Quarterly Reviews of Biophysics

www.cambridge.org/qrb

Single-molecule orientation-localization microscopy: Applications and approaches

Oumeng Zhang[1,2] and Matthew D. Lew[1]

[1]Preston M. Green Department of Electrical and Systems Engineering, Washington University in St. Louis, St. Louis, MO, USA and [2]Department of Electrical Engineering, California Institute of Technology, Pasadena, CA, USA

Review

Cite this article: Zhang O and Lew MD (2024). Single-molecule orientation-localization microscopy: Applications and approaches. *Quarterly Reviews of Biophysics*, **57**, e17, 1–30
https://doi.org/10.1017/S0033583524000167

Received: 02 August 2024
Revised: 03 November 2024
Accepted: 04 November 2024

Keywords:
fluorescence; biophysical chemistry and spectroscopy; physical chemistry; single-molecule dichroism; single-molecule fluorescence anisotropy

Corresponding authors:
Oumeng Zhang and Matthew D. Lew;
Emails: ozhang@caltech.edu; mdlew@wustl.edu

Abstract

Single-molecule orientation-localization microscopy (SMOLM) builds upon super-resolved localization microscopy by imaging orientations and rotational dynamics of individual molecules in addition to their positions. This added dimensionality provides unparalleled insights into nanoscale biophysical and biochemical processes, including the organization of actin networks, movement of molecular motors, conformations of DNA strands, growth and remodeling of amyloid aggregates, and composition changes within lipid membranes. In this review, we discuss recent innovations in SMOLM and cover three key aspects: (1) biophysical insights enabled by labeling strategies that endow fluorescent probes to bind to targets with orientation specificity; (2) advanced imaging techniques that leverage the physics of light-matter interactions and estimation theory to encode orientation information with high fidelity into microscope images; and (3) computational methods that ensure accurate and precise data analysis and interpretation, even in the presence of severe shot noise. Additionally, we compare labeling approaches, imaging hardware, and publicly available analysis software to aid the community in choosing the best SMOLM implementation for their specific biophysical application. Finally, we highlight future directions for SMOLM, such as the development of probes with improved photostability and specificity, the design of "smart" adaptive hardware, and the use of advanced computational approaches to handle large, complex datasets. This review underscores the significant current and potential impact of SMOLM in deepening our understanding of molecular dynamics, paving the way for future breakthroughs in the fields of biophysics, biochemistry, and materials science.

Table of contents

Introduction

Single molecules (SMs) have emerged as powerful, noninvasive probes for studies spanning biology, biochemistry, biophysics, and material science (Metskas and Rhoades, 2020; Möckl and Moerner, 2020; Lelek et al., 2021; Bustamante et al., 2021) since they were first observed using optical methods over three decades ago (Moerner and Kador, 1989; Betzig and Chichester, 1993; Xie, 1996). Their capability to discern and quantify intricate nanoscale processes at the molecular level continues to drive innovation in the field of microscopy. Over the last few decades, single-

molecule localization microscopy (SMLM) (Betzig et al., 2006; Hess et al., 2006; Rust et al., 2006; Sharonov and Hochstrasser, 2006) has revolutionized our ability to visualize cellular structures with unprecedented resolution surpassing the Abbé diffraction limit of ~250 nm. These techniques leverage the active control of fluorescence "on–off" states to reduce the concentration of emitting molecules, precisely localize the SMs, and reconstruct an image of the underlying structure with a typical resolution on the order of 10 nanometers (Moerner, 2015). During the past two decades, the field continues to innovate with sequential (Reinhardt et al., 2023), energy-transfer (Ghosh et al., 2019; Hauke et al., 2023; Chen et al., 2024a), interferometric (Shtengel et al., 2009; Aquino et al., 2011; Huang et al., 2016), and adaptive (Balzarotti et al., 2017; Cnossen et al., 2020; Gwosch et al., 2020; Weber et al., 2023; Sahl et al., 2024) imaging techniques, pushing practical localization precision to the molecular scale (<1 nm).

In the decade since the Nobel Prize in Chemistry 2014, developments have shifted toward *functional imaging*, i.e., sophisticated methods capable of imaging physicochemical properties beyond where molecules are located (Steves et al., 2024). Examples include measuring the emission spectrum (Zhang et al., 2015; Bongiovanni et al., 2016; Brenner et al., 2023), fluorescence lifetime (Thiele et al., 2020; Oleksiievets et al., 2022), and orientation and rotational diffusion, i.e., "wobble," (Backlund et al., 2014; Valades Cruz et al., 2016; Shaban et al., 2017) of individual molecules. Methods that simultaneously image molecular positions and orientations, termed single-molecule orientation-localization microscopy (SMOLM), have been shown to improve localization accuracy in SMLM since changes in orientation can be mistakenly perceived as changes in molecular position (Engelhardt et al., 2011; Backlund et al., 2012, 2014; Lew and Moerner, 2014; Backlund et al., 2016). Moreover, SMOLM offers profound insights into molecular structures and dynamics at the nanoscale that cannot be resolved in SMLM, such as the organization of amyloid aggregates (Shaban et al., 2017; Ding et al., 2020; Ding and Lew, 2021; Zhou et al., 2024a; Sun et al., 2024), conformations of DNA strands (Ha et al., 1996, 1998; Backer et al., 2016, 2019; Mazidi et al., 2019; Hulleman et al., 2021), structure of actin networks (Valades Cruz et al., 2016; Curcio et al., 2020; Rimoli et al., 2022), and the dynamic movements of molecular motors (Sosa et al., 2001; Peterman et al., 2001; Forkey et al., 2003; Beausang et al., 2013; Lippert et al., 2017).

In a typical SMOLM experiment, the target is labeled with fluorescent probes whose orientations convey useful information. Importantly, the fluorescent probe and labeling method must be chosen carefully. For example, a rigid bifunctional attachment strategy useful for probing the rotational motions of molecular motors is unlikely to be adaptable for characterizing the conformations of disordered proteins. In addition, fluorogenic "turn-on" probes, in contrast to conventional fluorophores, offer a degree of environmental sensitivity that can synergistically complement the orientational data measured by SMOLM.

The emitted fluorescence is then collected and modulated by an imaging system, and images are captured using photon-counting cameras. Since a standard fluorescence microscope has poor sensitivity for measuring molecular orientation, it must be modified to measure fluorescence emission under varying pumping polarization, manipulate the polarization and/or phase of the fluorescence emission, or both. These advancements, combined with algorithms capable of detecting dim fluorescent emitters and robustly estimating 2D/3D position and 2D/3D orientation simultaneously, are essential to quantify the rotational dynamics of SMs precisely and accurately.

In this review, we discuss new developments in these aspects of SMOLM and organize our coverage as follows. (Techniques that used polarized light to measure micro- and mesoscale biological structures are covered excellently elsewhere (Alonso, 2023; Brasselet and Alonso, 2023).) In the first section, we introduce various biophysical applications of SMOLM and labeling strategies that enable fluorophore orientations to sensitively probe the target of interest. We then discuss how light interacts with fluorescent molecules and vice versa, which establishes how microscope images can be used to sensitively measure molecular orientation. We next describe various methods for measuring SM orientations, followed by coverage of image analysis methods, including iterative methods for solving inverse problems and deep learning-based algorithms. The review concludes with an outlook suggesting future directions for SMOLM.

Sensing biomolecular architectures at the nanoscale: labeling strategies and applications

SMOLM can be applied to study a wide variety of targets, e.g., protein assemblies, nucleic acids, and lipids, and a broad variety of labeling and photochemistry have been harnessed to enable fluorophore orientations to faithfully probe the organization of biomolecules within the sample. We summarize recently reported labeling strategies in SMOLM in Figure 1 and their applications in Figures 2–4 and Table 1.

Covalent labeling of target structures

Many SMLM techniques, e.g., stochastic optical reconstruction microscopy (STORM) (Rust et al., 2006) and (fluorescence) photoactivation localization microscopy [(f)PALM] (Betzig et al., 2006; Hess et al., 2006) achieve SM blinking via specific photochemical conditions, e.g., by using specific illumination intensities and/or chemical imaging buffers. The target is labeled by covalently attaching an organic fluorophore or via fusing it to a fluorescent protein (Li and Vaughan, 2018). Due to the high rotational mobility of many chemical linkers (Sahoo et al., 2007; Doose et al., 2007; Sindbert et al., 2011; Chen et al., 2013; Beane et al., 2014; Gräwe and Stein, 2021), fluorescent probes usually rotate independently of the target molecule. Therefore, the probe and its attachment to the target must be carefully designed for SMOLM measurements. Here, we introduce labeling strategies that constrain the orientation of the fluorophores in a controlled relationship to the target structure.

Organization of actin filaments via covalent conjugation to phalloidin

The structural organization of actin filaments is crucial for various cellular processes, including motility, division, and force generation, all of which are fundamental to understanding cell mechanics. Accurately interpreting the orientational dynamics of fluorescent probes when studying actin filaments depends significantly on the rigidity of the linker connecting the fluorophore to the target molecule. Importantly, the orientational dynamics of fluorescent probes are influenced by both environmental forces (e.g., solvent collisions) and forces induced by the target of interest. It has been shown that even though phalloidin binds sufficiently rigidly to actin filaments, different linkers between the fluorophore and phalloidin exhibit different rigidities (Figure 1a).

https://doi.org/10.1017/S0033583524000167 Published online by Cambridge University Press

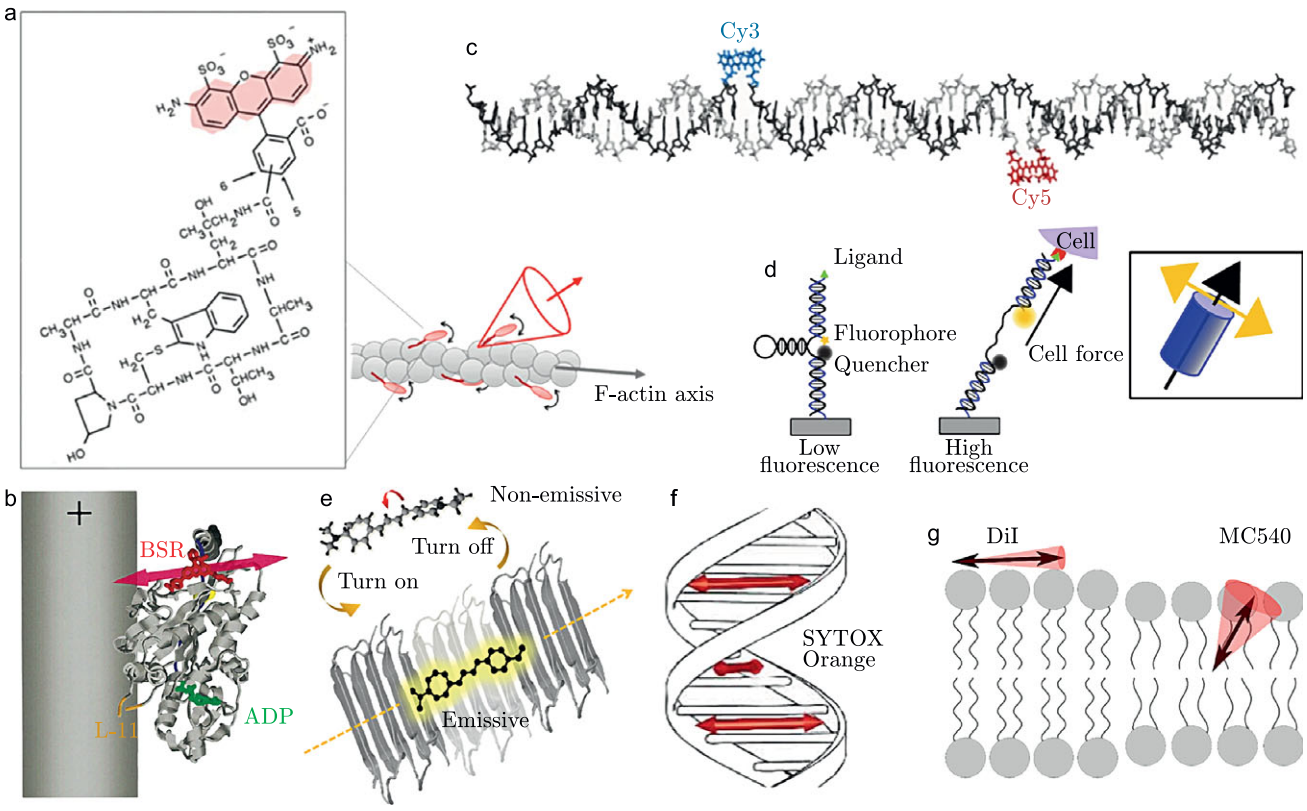

Figure 1. Representative labeling techniques in SMOLM. (a) Alexa Fluor 488-phalloidin conjugate labeling an actin filament (F-actin) (adapted from Rimoli et al., 2022). (b) Position and orientation of bis-((N-iodoacetyl)piperazinyl) sulfonerhodamine (BSR) on the kinesin protein structure (adapted from Sosa et al., 2001). (c) B-form double-stranded DNA internally labeled with covalently attached Cy3 and Cy5 dyes (adapted from Mortensen et al., 2015). (d) Concept of molecular tension DNA probes (adapted from Brockman et al., 2018). (e) Molecular rotors transiently bind to amyloid fibrils (adapted from Sarkar et al., 2023). (f) SYTOX orange dye intercalating within λ-DNA (adapted from Backer et al., 2016). (g) 1,1′-Dioctadecyl-3,3,3′,3′-Tetramethylindocarbocyanine Perchlorate (DiI) and merocyanine 540 (MC540) bound to gel- and fluid-like supported lipid bilayers, respectively (adapted from Lu et al., 2020).

Measuring the orientations of phalloidin-conjugated fluorescent molecules under identical labeling conditions, Valades Cruz et al. show that Atto 633-phalloidin exhibits a perpendicular orientation to actin stress fibers with a small wobble angle, whereas Alexa 488-phalloidin exhibits parallel orientations to actin stress fibers with slightly greater wobble angle (Figure 2a) (Valades Cruz et al., 2016). Alexa 647-phalloidin freely rotates due to its larger structure, which makes it inappropriate for studying actin fiber architectures using SMOLM. Comparing the wobbling behavior of differently charged dye molecules, including negatively charged Alexa 488, positively charged Atto 633, and neutral Atto 565, the authors surmise that the differences in wobbling of phalloidin conjugates are mostly attributed to the linker length; the linker length of Atto 565 is similar to that of Alexa 488, and they exhibit similar wobbling behavior. Similar relative degrees of rotational flexibility were also observed by (Figure 2b) Bruggeman et al. (2024).

Using the phalloidin-conjugated fluorophores, Rimoli et al. recently showed that SMOLM can resolve different nanoscale organizations of actin filament-based structures in mammalian cells (Figure 2c) (Rimoli et al., 2022); thin ventral and transverse arc stress fibers consist of highly aligned actin filaments, whereas thick peripheral and off-plane oriented dorsal stress fibers and focal adhesions consist of filaments with mixed orientations. The observations, especially within the dense assemblies, are uniquely enabled by orientation measurements using SMOLM.

Motor protein dynamics via bifunctional conjugation

Understanding the motions of motor proteins is crucial for understanding their mechanical and functional roles in cellular processes. One effective labeling strategy to study these dynamics is to attach fluorophores using more than one chemical linker to the target molecule, e.g., a bifunctional fluorophore that attaches to two separate residues of the target protein. In this way, the fluorophore's orientation is rigidly tied to the orientation of the target. For example, bifunctional rhodamine (Corrie et al., 1998) bound to two cysteines has been used to resolve the tilt, twist, and movement of myosin motors (Corrie et al., 1999; Forkey et al., 2003; Yildiz et al., 2003).

Beausang et al. show the stepping events of myosin V at sub-millisecond temporal resolution by labeling calmodulins along the lever arm with rhodamine (Beausang et al., 2013). They observed short-lived substeps (~10 to 15 ms), marked by highly disordered lever-arm orientations, which were interpreted as random fluctuations occurring when the detached head searched for the next binding site. The increased wobble during every other step aligns with the hand-over-hand mechanism and thermal search. These findings extend our understanding of the mechanical and thermal dynamics involved in the biophysical function of myosin V.

Another fluorophore, bis-((N-iodoacetyl)piperazinyl) sulfonerhodamine (BSR) has been used to track the translation and rotation of kinesin along microtubules (Figure 1b) (Peterman et al., 2001; Sosa et al., 2001; Asenjo et al., 2003). Attaching BSR to specific

https://doi.org/10.1017/S0033583524000167 Published online by Cambridge University Press

Table 1. Labeling strategies for SMOLM and their applications

Labeling strategy	Fluorophores	Typical exposure time and average signal	Applications
Covalent conjugation to phalloidin	Alexa Fluor 488, Atto 633, Alexa Fluor 647	100 ms, ~500 photons (Mehta et al., 2016) 100 ms, ~1700 photons (Rimoli et al., 2022)	Nanoscale organization of actin filaments and focal adhesions (Mehta et al., 2016; Rimoli et al., 2022; Valades Cruz et al., 2016)
Covalent bifunctional conjugation to cysteines	Bis-((*N*-iodo-acetyl)piperazinyl) sulfonerhodamine (BSR), bis-iodoacetamidorhodamine	100 ms, 1000 photon threshold (Sosa et al., 2001) 20 ms, ~500 photons (Forkey et al., 2003)	Motor protein dynamics, e.g., tilt, twist, and movement of myosin motors (Corrie et al., 1999; Forkey et al., 2003), and translation and rotation of kinesin along microtubules (Asenjo et al., 2003; Peterman et al., 2001; Sosa et al., 2001)
Covalent attachment to DNA (single linkage)	Cy3, Cy3B, Cy5	100 ms, 200 photons (Iqbal et al., 2008)	DNA hairpin-based tension probes (Blanchard et al., 2021; Brockman et al., 2018; Iqbal et al., 2008)
Covalent attachment to DNA (double linkage)	Cy3, Cy5	500 ms, ~1000–20,000 photons (Mortensen et al., 2015, 2016) 300 ms (Cervantes-Salguero et al., 2022) 100 ms (Cervantes-Salguero et al., 2024)	Structure and dynamics of biomolecules using engineered DNA structures (Cervantes-Salguero et al., 2022, 2024; Mortensen et al., 2015, 2016)
Intercalation within double-stranded DNA	YOYO–1, SYTOX orange, silicon-rhodamine-Hoechst 33342 conjugate	40 ms (a single frame, needs 3 frames for one measurement), ~1600 photons for SYTOX orange and ~8400 photons for silicon-rhodamine-Hoechst, (Backer et al., 2016) 100 ms (Mazidi et al., 2019) 100 ms, 4600 photons (Hulleman et al., 2021)	Measuring tangling, bending, supercoiling, and inclined base pairs within DNA (Valades Cruz et al., 2016; Backer et al., 2016; Mazidi et al., 2019; Hulleman et al., 2021; Backer et al., 2019)
Transient binding of lipophilic dyes (PAINT)	Nile red and derivatives (e.g., NR4A), Nile blue, merocyanine 540	30–100 ms, ~1300–5000 photons for Nile red, ~1700–4000 photons for Nile blue, ~1300–4300 photons for merocyanine 540 (Lu et al., 2020) 50 ms, ~1600 photons (Ding and Lew, 2021) 100 ms, ~3000–9000 photons (Zhang et al., 2022) 100 ms, ~5000 photons (Zhang et al., 2023)	Chemical composition and fluidity within nanodomains of cell membranes (Ding and Lew, 2021; Lu et al., 2020; Zhang et al., 2022, 2023)
Transient binding to protein oligomers and fibrils rich in β sheets	Thioflavin T and derivatives (ThT, ThX, etc.), Nile red, Nile blue, SYPRO orange, and LDS722	13–17 ms, ~500 photons per burst (Ding et al., 2020) 20 ms, ~580 photons (Ding and Lew, 2021) 30 ms (Sarkar et al., 2023) 20 ms, ~1600–3200 photons (Sun et al., 2024) 20 ms, ~750 photons (Zhou et al., 2024a)	Growth, decay, remodeling, and structural heterogeneities of amyloid fibrils and other β-sheet peptide self-assemblies (Ding et al., 2020; Ding and Lew, 2021; Krebs et al., 2005; Needham et al., 2020; Sarkar et al., 2023; Sun et al., 2024; Zhou et al., 2024a)
Doping within or direct conjugation to polymer films	Perylene-diimide (PDI), perylene-dicarboximide, perylene-monoimide (PMI), terylene-diimide (TDI), Alexa Fluor 532, Atto 647N, rhodamine B spiroamide	300 ms (Dedecker et al., 2009) 500 ms, ~250–1000 photons (Krause et al., 2016) 50 ms, ~1000–3800 photons (Zhang et al., 2018) 41,000 photons (Wang et al., 2019)	Characterizing architecture of and detecting mechanical fractures within bulk materials (Dedecker et al., 2009; Ham et al., 2014; Krause et al., 2016; Melnikov et al., 2007; Paeng and Kaufman, 2016; Wang et al., 2019; Zhang et al., 2018; Zheng et al., 2010)

Emitters other than single molecules, with various labeling strategies and applications: Fluorescence from quantum rods (Lippert et al., 2017; Ohmachi et al., 2012), scattered light from gold nanorods (Beckwith and Yang, 2021), and optically detected magnetic resonance imaging using nitrogen-vacancy centers in diamond (Backlund et al., 2017).

cysteine residues on kinesin enables precise monitoring of its orientation relative to the microtubule. SMOLM measurements revealed that, in the presence of AMP-PNP (a nonhydrolyzable analog of ATP), the kinesin motor domain maintains a rigid orientation with respect to the microtubule. Interestingly, in the presence of ADP, the motor domain transitions to a highly mobile state, which may be crucial for the 8-nm stepping motion of kinesin during processive movement (Sosa et al., 2001). A later study showed that these measured orientations align well with a hand-over-hand movement mechanism (Asenjo et al., 2003).

Other multifunctional linkers, e.g., fluorescein arsenical hairpin (FlAsH) (Griffin et al., 1998) and ReAsH (Adams et al., 2002), its resorufin-based cousin, that bind to four cysteines of a target protein, may also be used in SMOLM. Both FlAsH and ReAsH only become fluorescent upon proper binding and orientation of the tetracysteine motif (Walker et al., 2016). The drawback of these multifunctional strategies is that the labeling yield is generally low, and improperly labeled species, e.g., with only a single functional attachment, must be carefully removed to avoid artifacts (Peterman et al., 2001).

DNA structure, dynamics, and tension sensing via covalent conjugation

Recent advancements have also showcased SMOLM's utility for elucidating the structure and dynamics of engineered DNA structures (Cho et al., 2023; Zhan et al., 2023). A study using short double-stranded DNA molecules internally labeled with two distinct fluorophores (Cy3 and Cy5, Figure 1c) by Mortensen et al.

https://doi.org/10.1017/S0033583524000167 Published online by Cambridge University Press

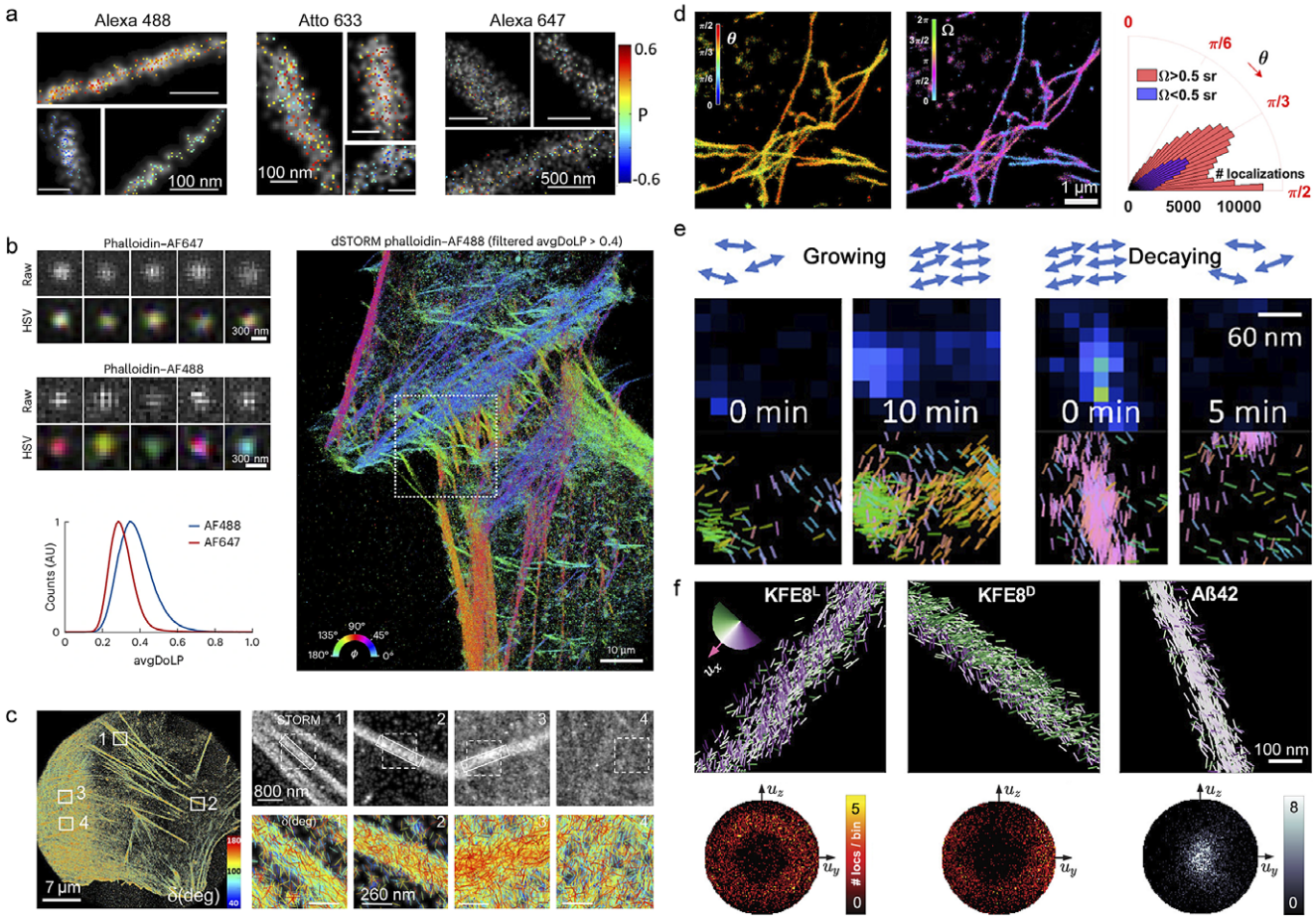

Figure 2. Imaging protein assemblies using SMOLM. (a) Polar-dSTORM imaging of actin stress fibers labeled with Alexa Fluor 488, Atto 633, and Alexa Fluor 647. Colors indicate the polarization factor *P*, equivalent here to linear dichroism *LD*, superimposed on grayscale dSTORM images (adapted from Valades Cruz et al., 2016). (b) Representative raw and hue-saturation-value (HSV) images of phalloidin-AF488 and phalloidin-AF647 bound to actin in fixed HeLa cells and distributions of the average degree of linear polarization (DoLP) for both fluorophores. Hue: angle of linear polarization (AoLP); saturation: DoLP; value: brightness (adapted from Bruggeman et al., 2024). (c) 4polar-STORM imaging of actin filament organization in fixed U2OS cells with color-coded wobbling angles δ (Alexa Fluor 488-phalloidin-labeled F-actin; adapted from Rimoli et al., 2022). The zoomed-in regions (1–4) show the (top) STORM and (bottom) 4polar-STORM images; lines indicate orientation, and colors represent wobble angles. (d) TAB SMOLM images of amyloid fibrils transiently labeled with LDS722, color-coded by (left) polar angle θ (rad) and (middle) wobble angle Ω (sr). The polar angle histogram reveals two distinct binding modes (adapted from Sarkar et al., 2023). (e) Visualization of growing and decaying amyloid-beta fibrils using (top) SMLM and (bottom) SMOLM with lines color-coded according to Nile blue orientation (adapted from Sun et al., 2024). (f) SMOLM images and orientation distributions for representative KFE8^{L}, KFE8^{D}, and Aβ42 fibrils (adapted from Zhou et al., 2024a). In each figure, Nile red orientations are plotted and color-coded relative to the long axis (u_x) of each fiber.

demonstrated the ability to resolve fluorophore separations as small as 10 base pairs, while accurately determining the 3D orientation of DNA molecules. Their findings establish the use of short, double-labeled DNA molecules as probes for mapping the 3D orientation of any structure to which they can be firmly attached (Mortensen et al., 2015, 2016).

Similarly, Hübner et al. utilized 2D rectangular DNA origami to study the binding orientations of ATTO 647N, ATTO 643, and Cy5 in different nanoenvironments (Figure 3a) (Hübner et al., 2021). They found that the nanoenvironment is crucial in determining the orientation of fluorophores. For instance, creating additional space by omitting nucleotides adjacent to a double-stranded region leads to stronger binding and a narrower, more defined distribution of dye orientations. Additionally, the dynamics of dye molecules around a DNA helix is affected by electrostatic and hydrophobic interactions, which complicates the accurate prediction of their final orientation within a DNA origami structure.

Cervantes-Salguero et al. explored the use of DNA origami to manipulate directly the orientations of cyanine dyes (Cervantes-Salguero et al., 2022) and to control the interduplex angles of dye-labeled Holliday Junction complexes (Figure 3b) (Cervantes-Salguero et al., 2024). They discovered that sequence-dependent partial intercalation of the dye could control its polar angle throughout a full revolution of a DNA double helix with a dispersion as small as ±4.5° within a 1.7 nm range. Additionally, they characterized experimentally the orientational constraints that Holliday Junctions impose on dye orientations; tuning the template conformation enabled the dye-template heterogeneity to be minimized.

In related work, Adamczyk et al. have demonstrated direct DNA engineering to control Cy5 and Cy3 orientations by doubly linking them to hybridized strands while leaving unpaired bases in the origami scaffold (Figure 3c) (Adamczyk et al., 2022). By varying the number of unpaired bases (from 0 to 8), the orientations of Cy5 and Cy3 were adjusted from perpendicular to parallel relative to the DNA double helix. With no unpaired bases, the dyes remained constrained and aligned perpendicularly. As the number of unpaired bases increased to 2, 4, or 6, the increased flexibility of

https://doi.org/10.1017/S0033583524000167 Published online by Cambridge University Press

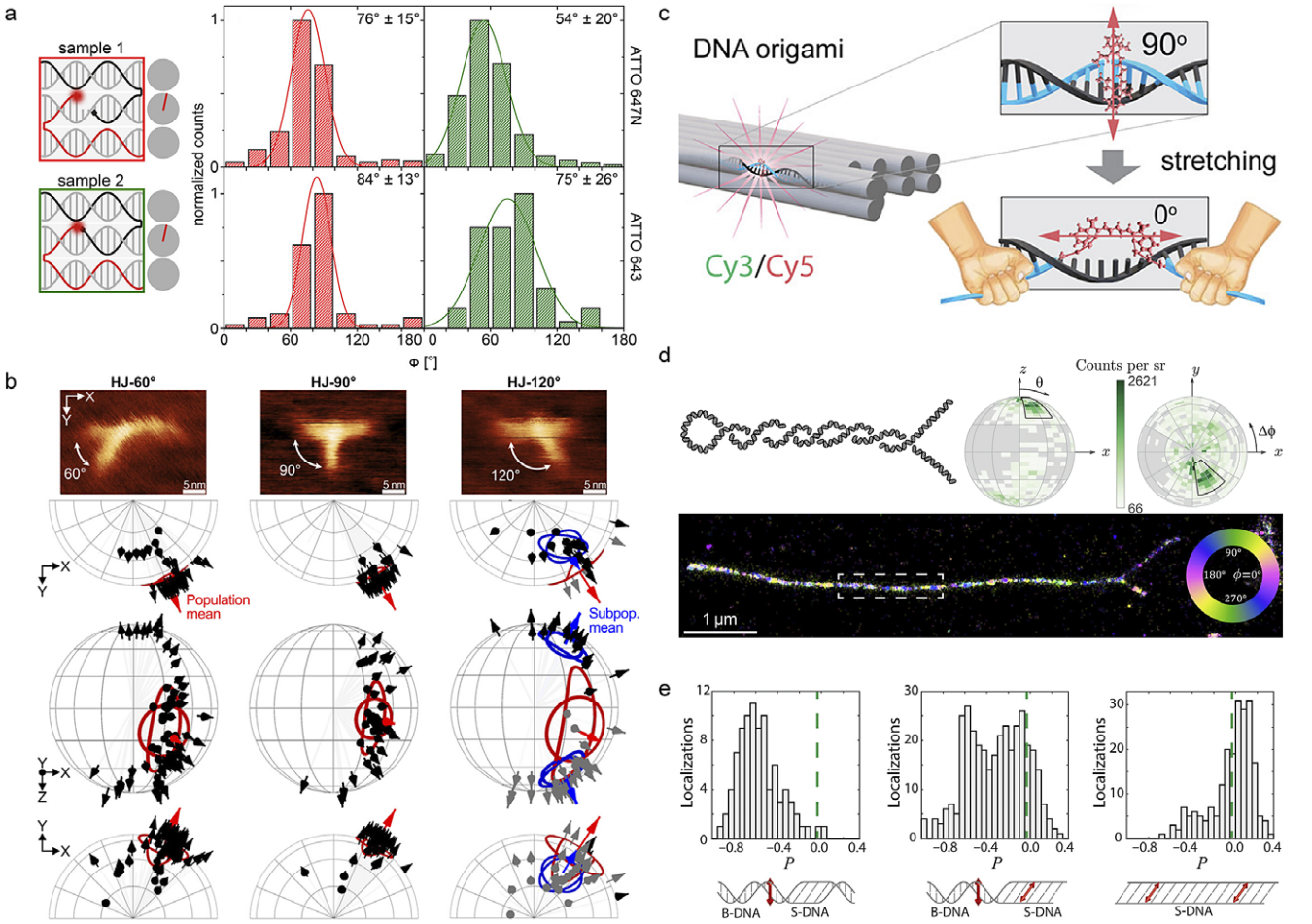

Figure 3. Imaging nucleic-acid structures and flexibility using SMOLM. (a) DNA helical winding of a scaffold strand (gray) and ssDNA staple (red line) labeled with a fluorophore (red dot), and orientation distributions of ATTO 647N and ATTO 643 within DNA origami structures 1 and 2 (adapted from Hübner et al., 2021). (b) (top) AFM and (bottom) three SMOLM views of Cy5 orientations within 4-arm Holliday Junction complexes (HJs) with interduplex angles of 60°, 90°, and 120° (adapted from Cervantes-Salguero et al., 2024). Mean orientations of populations and subpopulations are denoted by red and blue arrows, respectively. (c) Controlled orientations of doubly linked Cy3 and Cy5 molecules within DNA origami structures featuring different numbers of missing base pairs (adapted from Adamczyk et al., 2022). (d) (top left) Diagram and (bottom) SMOLM image of a plectoneme formed by a single supercoiled DNA molecule and distribution of SYTOX orange orientations along a typical individual strand aligned along the *x*-axis (adapted from Hulleman et al., 2021). Colors represent azimuthal orientations (top right) Typical orientation distribution of a supercoiled strand before it twists around itself. (e) Histograms of fluorescence polarization of DNA intercalators under stretching forces of 3, 7, and 35 pN (left to right) above the onset of the overstretching transition, along with illustrations of tilted intercalators (adapted from Backer et al., 2019).

the linker and additional spatial accommodation allowed the dyes greater rotational mobility when interacting with the DNA. At eight unpaired bases, the linkers fully extended, causing the fluorophores to align parallel to the DNA and become rotationally constrained.

Another promising application of SMOLM uses labeled DNA nanostructures to sense mechanical forces. Studies have shown that when Cy3B is covalently attached to the terminus of a DNA duplex, it aligns perpendicularly to the duplex's long axis (Iqbal et al., 2008). Consequently, when attached to DNA hairpin-based tension probes, the 3D orientation of piconewton cellular receptor forces can be determined using ensemble fluorescence polarization (Figure 1d) (Brockman et al., 2018; Blanchard et al., 2021). SMOLM has the potential to improve the sensitivity of these sensors to the single-molecule level.

Transient labeling of target structures

Binding-activated fluorescence is another mechanism to achieve SM blinking. In point accumulation for imaging in nanoscale topography (PAINT) (Sharonov and Hochstrasser, 2006; Kuo and Hochstrasser, 2011; Tholen et al., 2023), the fluorescence quantum yield of Nile red (NR), merocyanine 540, and other lipophilic probes increases within a non-polar chemical environment, e.g., when bound to a lipid bilayer. Since this initial demonstration, many variants of binding-activated SM blinking have been developed, including amyloid binding using amyloidophilic dyes (TAB, Spehar et al., 2018), DNA labeling using intercalating dyes (binding-activated localization microscopy, BALM (Schoen et al., 2011), and labeling a variety of biomolecules using dye-labeled oligonucleotides (DNA-PAINT, Jungmann et al., 2010, 2014; Steen et al., 2024). Unlike STORM and (f)PALM, which are limited by photobleaching of the fluorescent probes, the PAINT family of methods can collect an infinite number of localizations, due to the nearly limitless supply of fresh labels, in principle. The precise nature of dye-target interaction determines how the orientation of a fluorophore is related to the dynamics or organization of the target sample. Here, we discuss some PAINT-based methods that have been used in SMOLM.

https://doi.org/10.1017/S0033583524000167 Published online by Cambridge University Press

Amyloid aggregate structure and dynamics via transient binding of amyloidophilic dyes

A fundamental question in the study of amyloid-related neurodegenerative diseases, such as Alzheimer's, is how the structural organization of amyloid aggregates influences their pathological behavior. SMOLM is a powerful tool to reveal these nanoscale structural characteristics, providing insights that go beyond conventional methods like atomic force microscopy (AFM) and cryo-electron microscopy (cryo-EM). For example, the amyloidophilic dyes thioflavin T (ThT) (Spehar et al., 2018) and thioflavin X (ThX) (Needham et al., 2020), in addition to the lipophilic dyes Nile red (Ding et al., 2020) and Nile blue (Sun et al., 2024), have been used to transiently label amyloid aggregates for SMLM and SMOLM. These dyes only emit fluorescence when they are in the vicinity of the hydrophobic fibril surface; otherwise, their fluorescence quantum yield is low. SMOLM has shown that these dyes bind in a preferential direction to the grooves formed by cross-β sheets within fibrils, i.e., parallel to the fibril backbone (Krebs et al., 2005; Ding et al., 2020). Moreover, TAB dyes appear to exhibit a variety of orientations when bound to smaller oligomers (Ding et al., 2020; Ding and Lew, 2021), suggesting that these dyes may be useful for quantifying the organization of amyloid aggregates and studying how they disrupt cell membranes (Danzer et al., 2007; Outeiro et al., 2008). One significant development in TAB imaging is the use of dyes with improved signal-to-background ratios (SBR); Ding et al. reported that the background when using NR is reduced by 10-fold compared to ThT (Ding et al., 2020; Ding and Lew, 2021). Further, ThX exhibits a 5-fold improvement in brightness and a 7-fold increase in binding affinity compared to ThT (Needham et al., 2020) with the potential to produce dramatically more detailed SMOLM measurements.

Amyloid fibrils, such as those formed by amyloid-beta and alpha-synuclein, and other β-sheet peptide self-assemblies have since emerged as exciting applications for SMOLM studies using these dyes. For instance, Sarkar et al. discovered that SYPRO orange and LDS722, two molecular rotor dyes, exhibit distinct orientation characteristics when bound to amyloid fibrils compared to NR (Figures 1e and 2d) (Sarkar et al., 2023). Besides a population oriented parallel to the fibril, they observed an additional population with an inclined orientation, indicating diverse binding modes at different sites such as the fibril core, interfibril grooves, surface edges, ditches, and confined spaces in the fibril network. This structural diversity is crucial for understanding the biophysical properties of these environments, such as variations in local polarity, viscosity, and specific interactions like hydrogen bonding or π–π stacking.

Another critical biophysical question is understanding how the underlying molecular organization influences the growth and decay of fibrillar structures. Sun et al. used Nile blue to investigate the architecture and dynamics of Aβ42 fibrils (Figure 2e) (Sun et al., 2024). SMOLM revealed that assemblies with ordered and uniformly oriented structures are indicative of stable Aβ42 fibrils. Further, fibrils that show increasing uniformity are typically in a state of growth, whereas those that become more disordered correspond to decaying structures. SMOLM also revealed that locally disordered regions can facilitate large-scale fibrillar remodeling.

In another study, Zhou et al. used NR to reveal the helical (bilayer) ribbon architecture of fibrils of the engineered peptide KFE8 and recombinant Aβ42. Precise SMOLM measurements quantified the tilt of both the inner and outer layers of the fibrils relative to the long axis (Figure 2f) (Zhou et al., 2024a). Moreover, SM orientations revealed that the architectures of both KFE8 and Aβ42 are consistent with a helical bilayer ribbon, rather than a helical monolayer. However, KFE8 exhibits larger tilt angles, resulting in a higher diameter-to-pitch ratio, which indicates a more pronounced helicity; Aβ42 resembles an approximately straight line with only a modest backbone tilt. Without orientation data, these differences are difficult to discern in SMLM. SMOLM further enabled the differentiation of polymorphic branched and curved morphologies in KFE8, revealing significantly greater backbone heterogeneity compared to the more uniform straight Aβ42 fibrils.

DNA structure and dynamics via transient binding of DNA intercalators

The fluorescence of many DNA intercalating dyes (Flors et al., 2009) is enhanced upon binding to double-stranded DNA; imaging these dyes at the SM level enables binding-activated localization microscopy (BALM) (Schoen et al., 2011). It has been shown that SYTOX orange binds perpendicularly to the axis of λ-DNA (Figure 1f) (Backer et al., 2016), and YOYO-1 dyes exhibit a primary binding mode perpendicular to the DNA axis and a secondary binding mode parallel to the DNA axis (Larsson et al., 1994; Valades Cruz et al., 2016; Mazidi et al., 2019). Therefore, they have been used to resolve tangling, bending, and supercoiling of DNA (Figure 3d) (Hulleman et al., 2021). In contrast to SYTOX orange and YOYO-1, SiR-Hoechst exhibits nonspecific binding orientations due to its flexible four-carbon linker even though Hoechst is directly attached to the DNA strand. Therefore, it is not suitable for SMOLM (Backer et al., 2016).

Studies have shown that the orientation of intercalators can reveal structural differences between B-DNA and mechanically extended S-DNA. Backer et al. demonstrated that when DNA is stretched beyond the overstretching transition, intercalators like YOYO-1 exhibit a significant tilt, with an angle of approximately 54° relative to the S-DNA axis, in contrast to their typical perpendicular orientation (~90°) in B-DNA (Figure 3e) (Backer et al., 2019). This tilting provides the first experimental evidence of inclined base pairs in mechanically stretched DNA, offering a clearer understanding of the S-DNA conformation. However, the authors caution that the precise inclination of S-DNA base pairs might be perturbed by the presence of intercalators.

Lipid membrane structure and composition via transient binding of lipophilic dyes

The manner by which lipophilic probes transiently bind to model and cellular membranes is governed by the chemical environment and the molecular interactions within these complex assemblies. For example, the transition dipole moment of DiI (1,1′-Dioctadecyl-3,3,3′,3′-tetramethylindocarbocyanine perchlorate, $DiIC_{18}(3)$) bound to DPPC (1,2-Dipalmitoyl-sn-glycero-3-phosphocholine) supported lipid bilayers (SLBs) is oriented parallel to the membrane, as its hydrocarbon chains are incorporated in the nonpolar core while the chromophore headgroup resides in the polar region of the lipid bilayer. In contrast, the orientations of merocyanine 540 (MC540) are mostly perpendicular to a more fluid membrane composed of DOPC (1,2-Dioleoyl-sn-glycero-3-phosphocholine); MC540 also exhibits larger wobble angles in these membranes (Figure 1g) (Lu et al., 2020). Thus, the orientations of transiently bound probes measured via SMOLM reveal the chemical composition and fluidity of nanodomains within both model and cellular membranes.

The orientation spectra of NR molecules are extremely sensitive to the cholesterol concentration within the SLBs; they are confined and perpendicular to the membrane at high cholesterol concentrations and are relatively free to wobble at low cholesterol

https://doi.org/10.1017/S0033583524000167 Published online by Cambridge University Press

concentrations along the polar direction (parallel to the lipid acyl chains) (Figure 4a) (Ding and Lew, 2021). This behavior aligns with the "umbrella model" of lipid bilayers, where cholesterol condenses the lipid environment and creates ordered domains that restrict molecular movement. NR-membrane interactions have also facilitated the use of spherical supported lipid bilayers as 3D calibration targets for SMOLM (Wu et al., 2022a; Zhang et al., 2023; Bruggeman et al., 2024). However, its structural analog Nile blue is insensitive to cholesterol concentration within the membrane, emphasizing the importance of properly choosing probes for sensing specific membrane characteristics.

SMOLM has been used to study enzyme-induced reorganization of lipid domains. For instance, Lu et al. visualized the restructuring of lipid domains by sphingomyelinase (SMase), an enzyme that catalyzes the hydrolysis of sphingomyelin into ceramide by measuring the orientation spectra of NR and MC540 (Figure 4b) (Lu et al., 2020). Upon the addition of SMase, membrane composition shifted as ceramide formed and reorganized the structure. A dose-dependent disappearance of cholesterol-rich liquid-ordered domains was observed, and these regions were replaced by ceramide-rich domains.

Zhang et al. recently reported simultaneous ordering and damage of a lipid bilayer caused by cholesterol-loaded methyl-β-cyclodextrin via tracking the orientations and positions of single NR molecules transiently bound to DPPC SLBs (Figure 4c) (Zhang et al., 2022). The study revealed that while cholesterol deposition reduces NR's rotational diffusion, MβCD-chol somewhat counterintuitively increases translational motions within the membrane as it nonuniformly dissolves the SLB. Therefore, SMOLM's ability to measure rotations and positions simultaneously yields insights into complex changes in membrane structure that cannot be quantified via traditional single-particle tracking or polarization anisotropy alone.

SMOLM with NR has also been applied to study complex membrane-amyloid interactions with single-molecule sensitivity. Zhang et al. demonstrated that when amyloid aggregates infiltrate lipid membranes, they significantly change the rotational dynamics of NR molecules. Specifically, NR exhibited increased wobble angles in regions infiltrated by amyloid aggregates compared to those in pure DPPC SLBs. Further, the study found that Aβ42 aggregates interacting with lipid membranes tend to form smaller assemblies, such as oligomers and protofibrils, rather than fully developed fibrils (Figure 4d).

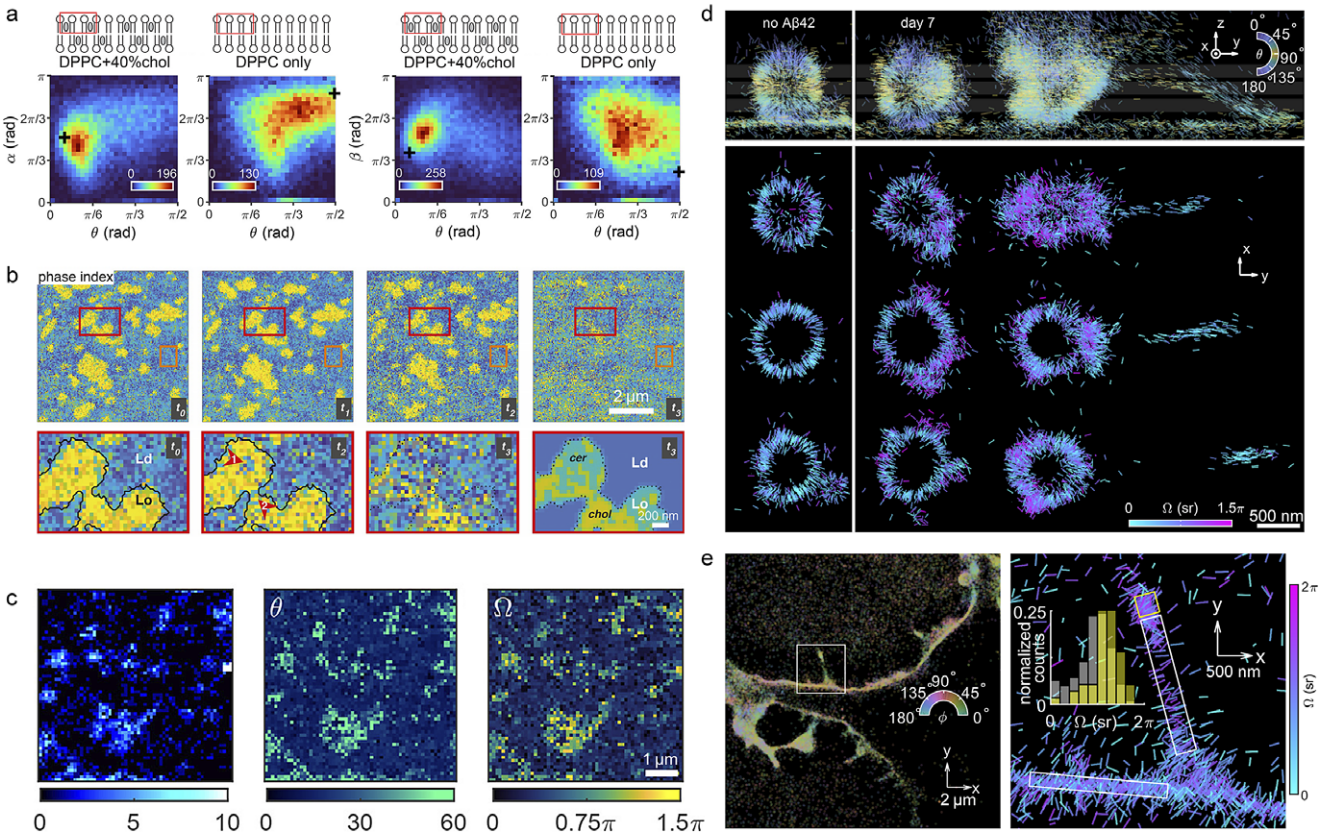

Figure 4. Imaging lipid membranes using SMOLM. (a) Distribution of polar angle (θ) and wobble angles (α along the polar direction and β perpendicular to the polar direction) of Nile red (NR) within DPPC bilayers with and without cholesterol (adapted from Ding and Lew, 2021). (b) SMOLM images of NR before and after successive sphingomyelinase (SMase) treatments reveal compositional changes within the liquid-ordered (Lo) domain and minor changes in domain size and shape during the treatment (adapted from Lu et al., 2020). (c) Nanodomains within SLBs sensed by transiently binding NR molecules using the raPol microscope (adapted from Zhang et al., 2022). (Left) localization density per 100 × 100 nm^2 in the azimuthally polarized channel; (middle) polar angle θ (deg); (right) wobble angle Ω (sr). (d) Orientations of Nile red (NR) transiently bound to spherical supported lipid bilayers (SLBs) after a 7-day incubation (left) without and (right) with Aβ42 monomers (adapted from Zhang et al., 2023). Localizations are color-coded by (top) polar angle θ (deg) and (bottom) wobble angle Ω (sr). All images are lateral (*xy*) views unless otherwise marked. (e) SMOLM images of an HEK-293T cell. Localizations are (left) color-coded by and (right) oriented along azimuthal angle ϕ (deg). (Right) Zoomed image of the boxed region at left, color-coded by wobble angle Ω (sr). The inset histogram shows the distribution of the measured wobble angle within the regions marked by yellow and white boxes (adapted from Zhang et al., 2023).

https://doi.org/10.1017/S0033583524000167 Published online by Cambridge University Press

Such dye-membrane interactions are not limited to model systems. For example, SMOLM has revealed diverse binding modes of MC540 on cell membranes, influenced by several factors including membrane tension, fluidity, and potential (Zhang et al., 2023). Imaging the wobble angle of MC540 reveals that the rigidity of the coverslip reduces membrane fluidity near the cell-coverslip interface, while lipids at the tip of a membrane protrusion are more fluid than those in surrounding regions (Figure 4e).

Other labeling strategies and applications

SMs embedded within polymer films can also be used to detect architectural changes and mechanical fractures since rotational motions are sometimes more sensitive to these changes compared to translational motions. Early SM orientation measurements used defocused imaging to map the orientations of dye molecules at various positions within dendrimers and below and above the glass transition temperature of the host material (Melnikov et al., 2007; Dedecker et al., 2009; Zheng et al., 2010; Ham et al., 2014; Paeng and Kaufman, 2016). More recently, researchers have used SMOLM to detect the nanoscale softening (Zhang et al., 2018) and deformation (Krause et al., 2016; Wang et al., 2019) of polymer matrices as fluorophore orientations change.

Besides SMs, the orientations of luminescent and scattering nanoparticles can also be resolved by imaging systems. For example, quantum nanorods are much brighter probes compared to typical fluorescent molecules and have been used for studying the force-generating mechanism of dynein molecules (Lippert et al., 2017). Tracking the orientation and position of gold nanorods using scattering light has been shown to achieve sub-millisecond temporal resolution (Beckwith and Yang, 2021) as the number of signal photons is no longer limited by photobleaching. However, since the size of typical quantum rods is 10 or 100 times compared to that of organic fluorophores, SMOLM is generally a less perturbative choice for studying biochemical processes. A similar concept to SMOLM has also been implemented in optically detected magnetic resonance imaging using nitrogen-vacancy centers in diamonds (Backlund et al., 2017).

Choosing the appropriate labeling strategy for SMOLM

The advantages and limitations of various labeling strategies, along with their applications, are summarized in Table 1. It is important to note that any exogenous probe can introduce perturbations to the biophysical structure or process under study. For instance, SYTOX orange DNA intercalators (Figure 1f), which increase quantum yield upon binding to DNA, may trap non-canonical conformations such as unstacked flanking bases upon interacting with the biomolecular surface (Biebricher et al., 2015; Kolbeck et al., 2024). Such alterations in local DNA structure can affect the conformational dynamics of the system and potentially influence the orientation data obtained through SMOLM. These perturbative effects, which may also occur with other intercalating dyes, must be carefully considered when interpreting results. Similarly, internal labeling strategies using Cy3 and Cy5 dyes (Figure 1c) can disturb local DNA conformation by replacing nucleotides within the backbone, leading to structural disorder and rapid orientational dynamics of the probe. A recent study using polarization-sensitive fluorescence microscopy has shown that Cy3 labeled single-stranded-double-stranded DNA junctions undergo significant conformational changes depending on the position and temperature (Heussman et al., 2022), and Maurer et al. further demonstrated that DNA "breathing" at these junctions can shift between multiple conformational macrostates (Maurer et al., 2023). Fluorescent dyes can also perturb peptide aggregates; Sun et al. used the photo-oxidation of thioflavin T, a common amyloidophilic dye, to induce growth, depolymerization, and remodeling within Aβ42 fibrils (Figure 2e) (Sun et al., 2024). Therefore, control experiments are essential to quantify the extent of dye-induced perturbations and to ensure reliable interpretation of SMOLM data.

When selecting probe-labeling strategies for SMOLM, it is important to balance the need for site-specific information with the risk of structural disruption. Covalent labeling offers precise control over fluorophore orientation relative to the attachment site (Budiarta et al., 2024) and can provide valuable insights into the conformational dynamics of protein domains. However, rigidly attaching a fluorophore to a target protein domain with a high yield may interfere with function or may not be feasible, depending on the domain's inherent flexibility. On the other hand, transient binding approaches mitigate these issues by avoiding high concentrations of covalently bound fluorophores; this method allows for temporary, low-concentration interactions of the dye with the target system, thereby reducing the number of labeled molecules compared to conventional labeling strategies. However, precise targeting of transiently binding probes to specific protein domains remains a challenge (Steen et al., 2024). As is the case with SMLM, proper choice of the labeling strategy is essential for ensuring useful and robust orientation measurements with minimal perturbation in SMOLM.

Interaction between light and fluorescent molecules

In this section, we introduce how light interacts with fluorescent molecules (Valeur, 2002; Novotny and Hecht, 2012). A photon from an optical field may be absorbed by a molecule, resulting in an electronic state transition from the singlet ground state S_0, i.e., the highest occupied molecular orbital, to various vibrational levels of the singlet excited state S_1, i.e., the lowest unoccupied molecular orbital. After a fast vibrational relaxation (typically on the order of a few picoseconds), the molecule decays to the lowest energy level of S_1. After a few nanoseconds, i.e., the *fluorescence* or *excited-state lifetime*, the molecule returns to a vibrationally excited state of S_0 by emitting a red-shifted fluorescence photon with lower energy. The molecule may also lose its energy via nonradiative relaxation such as vibration and collision and return to the ground state, which reduces the number of photons emitted. Therefore, the quality of a molecule as a fluorophore is measured by its quantum yield (Valeur, 2002)

$$\eta_{\mathrm{q}} = \frac{\gamma_{\mathrm{r}}}{\gamma_{\mathrm{r}} + \gamma_{\mathrm{nr}}}, \tag{1}$$

where γ_{r} is the fluorescence rate and γ_{nr} is the nonradiative relaxation rate; molecules with a quantum yield above 10% are usually considered quite fluorescent. Some widely-used fluorophores in single-molecule imaging, e.g., NR (Kucherak et al., 2010) and Rhodamine 6G (Fischer and Georges, 1996), may exhibit a quantum yield of >90% depending on the local environment (Li and Vaughan, 2018; Jradi and Lavis, 2019).

When a molecule is in the excited state S_1, it may also undergo intersystem crossing due to spin-orbital coupling and enter a long-lived (microseconds to seconds) and reactive triplet state T_1. Upon entering this state, the molecule cannot undergo repeated absorption and emission cycles; it appears to go dark. From the triplet state

https://doi.org/10.1017/S0033583524000167 Published online by Cambridge University Press

T_1, the molecule may return to S_0 via phosphorescence or non-radiative relaxation. It may also undergo chemical reactions with singlet oxygen and other reactive oxygen species and permanently lose its ability to fluoresce. This process is termed *photobleaching*, which fundamentally limits the number of photons emitted by a fluorescent molecule and is determined by the intrinsic photophysics and photochemistry of the fluorophore (Cordes et al., 2011; Ha and Tinnefeld, 2012; Gust et al., 2014). The total number of photons emitted by an SM may be increased by decreasing the photobleaching rate via quenching the triplet state, e.g., using photostabilizers, reducing or oxidizing agents, and oxygen-scavenging systems (Rasnik et al., 2006; Aitken et al., 2008; Vogelsang et al., 2008; Dave et al., 2009; Hoffman et al., 2011; Lee et al., 2013; Nahidiazar et al., 2016; Glembockyte et al., 2016; Sauer and Heilemann, 2017), or enhancing the emission rate using plasmonic nanoantennas (Kinkhabwala et al., 2009; Wientjes et al., 2016; Kaminska et al., 2018; Grabenhorst et al., 2020). However, one must note that these methods could potentially perturb the imaging targets themselves (Tosheva et al., 2020). In addition, nearby plasmonic nanoparticles will also distort the image of each fluorophore (Lim et al., 2016; Raab et al., 2017; Goldwyn et al., 2018; Zuo et al., 2019; Bloksma and Zijlstra 2021; Zuo et al., 2021; Moon et al., 2023; Huijben et al., 2024), compared to typical dipolar emission.

The orientation of fluorescent molecules relative to the applied optical field affects how they interact. Briefly, we may describe the interaction between a charge-neutral nanoparticle with an optical field by writing the multipolar interaction Hamiltonian (Novotny and Hecht, 2012)

$$H = \boldsymbol{p}_e \cdot \boldsymbol{E} - \boldsymbol{p}_m \cdot \boldsymbol{B} - [\boldsymbol{Q}\nabla] \cdot \boldsymbol{E} - \ldots, \tag{2}$$

where vectors $\boldsymbol{p}_e$ and $\boldsymbol{p}_m$ represent the total electric and magnetic dipole moments, respectively, the matrix $\boldsymbol{Q}$ represents the electric quadrupole moment, $\boldsymbol{E}$ and $\boldsymbol{B}$ represent the electric and magnetic fields, respectively, and $\boldsymbol{p}_e \cdot \boldsymbol{E} = \boldsymbol{p}_e^{\top} \boldsymbol{E}$ represents the dot or inner product between vectors $\boldsymbol{p}_e$ and $\boldsymbol{E}$. For typical SM imaging experiments where both illumination and emission are manipulated in the far-field, the magnetic dipole and electric quadrupole interactions are orders of magnitude weaker compared to the electric dipole interaction. Therefore, we describe the photon absorption and emission processes using only the electric dipole moments.

The transition dipole moment is the electric dipole moment associated with the transition between two quantum states. The absorption dipole moment describes the transition between initial state S_0 and final state S_1; the emission dipole moment describes the transition between initial state S_1 and final state S_0. Here, we omit the amplitude and only describe the orientation of a transition dipole using a unit vector (Figure 5a)

$$\boldsymbol{\mu} = \begin{bmatrix} \mu_x & \mu_y & \mu_z \end{bmatrix}^{\top} = \begin{bmatrix} \sin\theta\cos\phi & \sin\theta\sin\phi & \cos\theta \end{bmatrix}^{\top}, \tag{3}$$

where z represents the direction of the optical axis. Note that due to the two-fold degeneracy of a dipole moment, this unit vector is defined over a unit hemisphere. We only consider linear dipoles here; chirality may be modeled as a coherent superposition of multiple linear dipoles with spatial phase differences (Cyphersmith et al., 2011). Fundamentally, the orientation of the transition dipole moment $\boldsymbol{\mu}$ determines how the molecule interacts with the polarization of the optical field.

Absorption dipole moments

We now briefly introduce a model for light absorption by an SM. The transition dipole moment can be described as a quantum mechanical state transition, given by

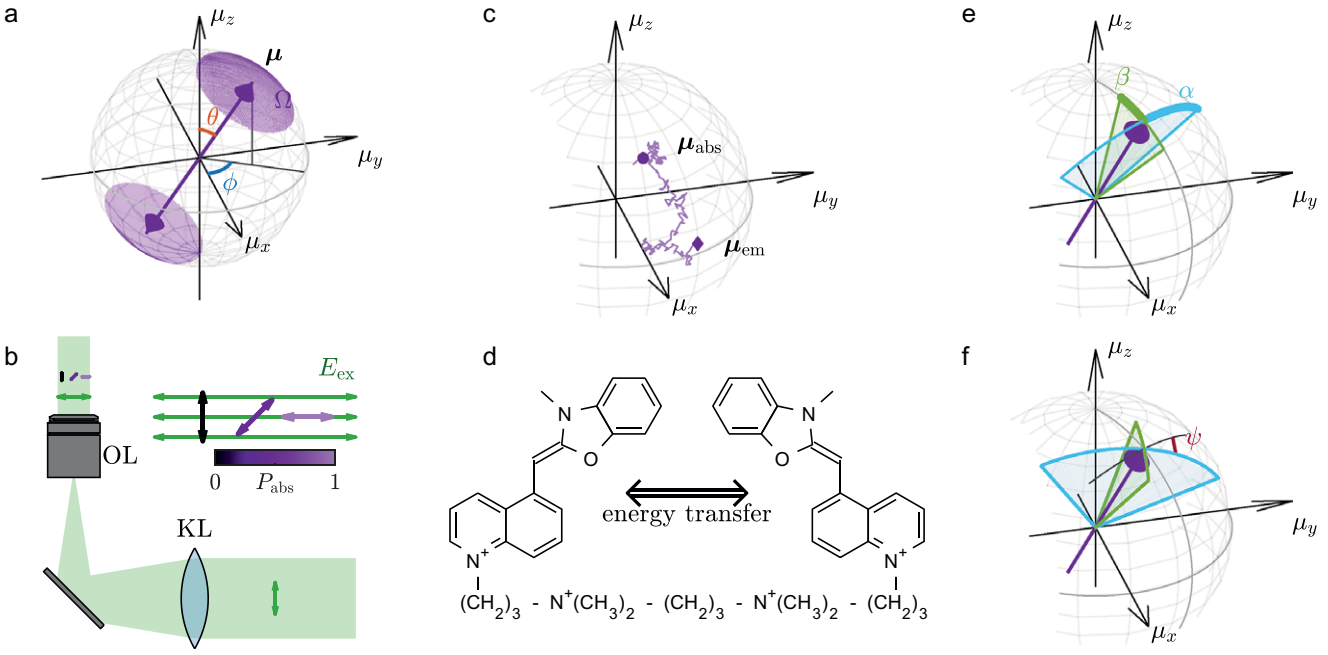

Figure 5. (a) Molecular orientation represented by a unit vector $\boldsymbol{\mu} = \left[\mu_x, \mu_y, \mu_z\right]^{\top} = \left[\sin\theta\cos\phi, \sin\theta\sin\phi, \cos\theta\right]^{\top}$. The wobble is modeled as a hard-edged cone with cone solid angle Ω (b) Excitation light in typical SMOLM. A Kohler lens (KL) is used to produce a collimated illumination beam above the objective lens (OL). The absorption probability is a function of the angle between the absorption dipole moment $\boldsymbol{\mu}_{abs}$ and the excitation optical field $\boldsymbol{E}_{ex}$ (green arrows). The absorption probability is maximized if $\boldsymbol{\mu}_{abs}$ is parallel to $\boldsymbol{E}_{ex}$. Colorbar: normalized absorption probability. (c) Depolarization, i.e., a non-zero angle between $\boldsymbol{\mu}_{abs}$ and $\boldsymbol{\mu}_{em}$ caused by rotation during the fluorescence lifetime between the absorption and emission events. (d) Depolarization caused by energy transfer between chromophores of a YOYO-1. (e,f) Anisotropic rotational diffusion models for SMs. (e) Cone half angles α and β represent the area within which the molecule can wobble, and (f) ψ describes the preferred direction of the wobble.

https://doi.org/10.1017/S0033583524000167 Published online by Cambridge University Press

$$\boldsymbol{\mu}_{\text{abs}} = \langle \psi_1 | q\boldsymbol{r} | \psi_0 \rangle = q \iiint \psi_1(\boldsymbol{r})^* \boldsymbol{r} \psi_0(\boldsymbol{r}) d^3\boldsymbol{r}, \tag{4}$$

where q represents the charge and $\boldsymbol{r}$ represents its position. Kets $|\psi_0\rangle$ and $|\psi_1\rangle$ represent the states associated with ground state S_0 and excited state S_1, respectively. According to Fermi's golden rule (Shankar, 2012), the SM's rate of transition from S_0 to S_1 in the presence of excitation field $\boldsymbol{E}_{\text{ex}} = [E_x, E_y, E_z]^\top$ is given by (Figure 5b)

$$P_{\text{abs}} \propto |\langle \psi_1 | \boldsymbol{E}_{\text{ex}} \cdot \boldsymbol{r} | \psi_0 \rangle|^2 \propto |\boldsymbol{E}_{\text{ex}} \cdot \boldsymbol{\mu}_{\text{abs}}|^2. \tag{5}$$

A molecule at its ground state S_0 is more likely to absorb an incident photon if the polarization of the photon is parallel to the absorption dipole moment $\boldsymbol{\mu}_{\text{abs}}$. In contrast, the absorption probability is zero if the absorption dipole moment is perpendicular to the polarization of the local electric field $\boldsymbol{E}_{\text{ex}}$.

Emission dipole moments

Suppose a molecule with an emission dipole moment of $\boldsymbol{\mu}_{\text{em}}$ located at $\boldsymbol{r} = [0,0,0]^\top$ relaxes from excited state S_1 to ground state S_0 and emits a photon. The classical far-field emission at position $\boldsymbol{r}_{\text{ff}}$ can be found by solving the electromagnetic wave equation for an oscillating dipole source (Novotny and Hecht, 2012), yielding (Figure 6a)

$$\boldsymbol{E}_{\text{ff}} = c_{\text{ff}} \hat{\boldsymbol{r}}_{\text{ff}} \times (\boldsymbol{\mu}_{\text{em}} \times \hat{\boldsymbol{r}}_{\text{ff}}) = c_{\text{ff}} \left(\mathbb{I} - \hat{\boldsymbol{r}}_{\text{ff}} \hat{\boldsymbol{r}}_{\text{ff}}^\top\right) \boldsymbol{\mu}_{\text{em}}, \tag{6}$$

where the unit vector

$$\hat{\boldsymbol{r}}_{\text{ff}} = \frac{\boldsymbol{r}_{\text{ff}}}{|\boldsymbol{r}_{\text{ff}}|} = [\sin\theta_{\text{ff}} \cos\phi_{\text{ff}} \quad \sin\theta_{\text{ff}} \sin\phi_{\text{ff}} \quad \cos\theta_{\text{ff}}]^\top \tag{7}$$

represents the viewing direction, c_{ff} is a normalization factor, $\mathbb{I}$ represents the identity matrix, and $\hat{\boldsymbol{r}}_{\text{ff}} \hat{\boldsymbol{r}}_{\text{ff}}^\top$ represents the outer product of $\hat{\boldsymbol{r}}_{\text{ff}}$ with itself. Therefore,

$$I_{\text{ff}} = |\boldsymbol{E}_{\text{ff}}|^2 \propto \left(\boldsymbol{\mu}_{\text{em}} - \hat{\boldsymbol{r}}_{\text{ff}} \hat{\boldsymbol{r}}_{\text{ff}}^\top \boldsymbol{\mu}_{\text{em}}\right) \cdot \left(\boldsymbol{\mu}_{\text{em}} - \hat{\boldsymbol{r}}_{\text{ff}} \hat{\boldsymbol{r}}_{\text{ff}}^\top \boldsymbol{\mu}_{\text{em}}\right) = 1 - (\hat{\boldsymbol{r}}_{\text{ff}} \cdot \boldsymbol{\mu}_{\text{em}})^2, \tag{8}$$

i.e., the fluorescence intensity has a sine-square dependence on the angle between the molecular orientation $\boldsymbol{\mu}_{\text{em}}$ and viewing direction $\hat{\boldsymbol{r}}_{\text{ff}}$. In addition, optical field is always perpendicular to the propagation direction, i.e.,

$$\hat{\boldsymbol{r}}_{\text{ff}} \cdot \boldsymbol{E}_{\text{ff}} \propto \hat{\boldsymbol{r}}_{\text{ff}} \cdot \boldsymbol{\mu}_{\text{em}} - \hat{\boldsymbol{r}}_{\text{ff}}^\top \hat{\boldsymbol{r}}_{\text{ff}} \hat{\boldsymbol{r}}_{\text{ff}}^\top \boldsymbol{\mu}_{\text{em}} = 0. \tag{9}$$

Note that even though both the absorption and emission dipole moments can be used for measuring the orientation of fluorescent molecules, they are not necessarily parallel to each other. Depolarization between the absorption and emission dipoles can be quantified by measuring fluorescence anisotropy (see next section for detailed discussion). The relationship between the fluorescence lifetime and rotational correlation time determines how far the molecule may rotate between an absorption and an emission event. A molecule's emission dipole moment $\boldsymbol{\mu}_{\text{em}}$ is decoupled from its absorption dipole moment $\boldsymbol{\mu}_{\text{abs}}$ when the molecule's rotation is much faster compared to its fluorescence lifetime (Lew et al., 2013; Backlund et al., 2014; Stallinga, 2015), which is typical for SMs in liquids. The correlation between $\boldsymbol{\mu}_{\text{em}}$ and $\boldsymbol{\mu}_{\text{abs}}$ becomes prominent when the rotational correlation time is comparable to the lifetime, e.g, when molecules are embedded within dense lipid membranes (Halder et al., 2018). Even for molecules that are immobilized within rigid substrates like polymer matrices, it is reported that these two vectors may exhibit an inclination angle of more than 20° from each other (Karedla et al., 2015) due to the interactions between molecular orbitals and the

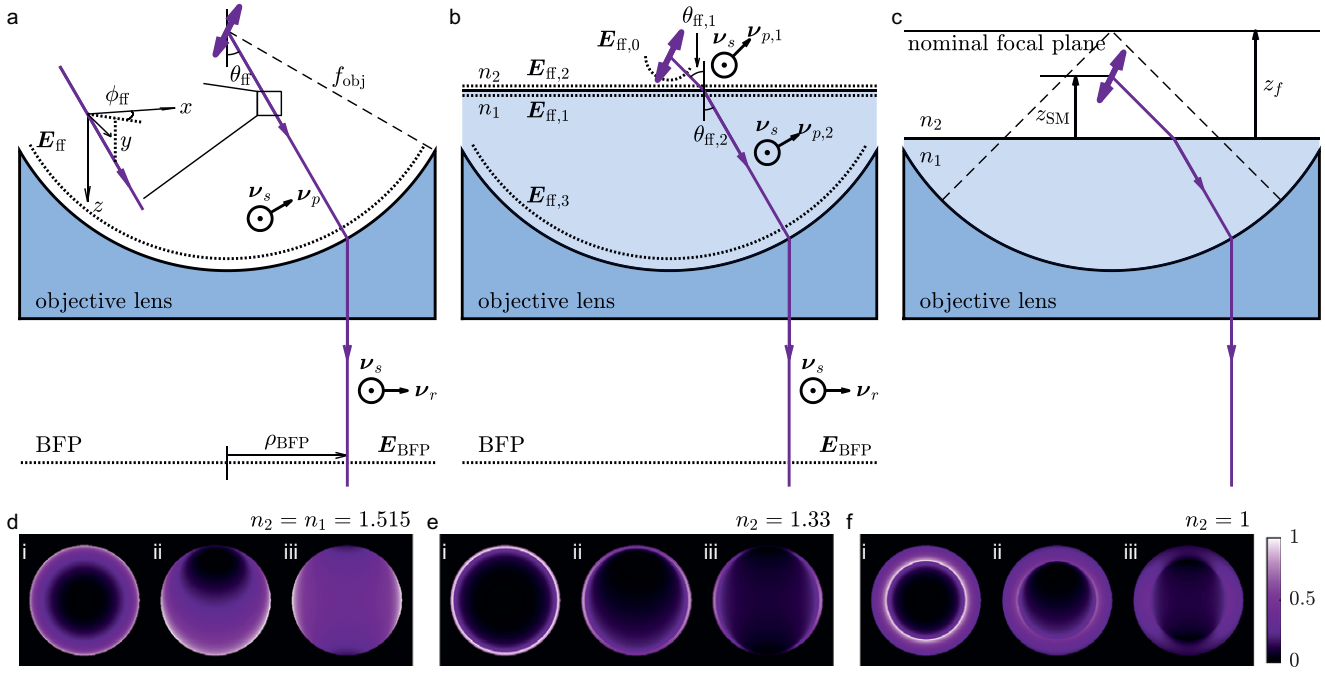

Figure 6. Schematic diagram of dipole emitters (a) within a medium of matched RI and (b) near the RI interface between the sample (n_2) and lens immersion medium (n_1). The objective lens captures a pseudo-spherical wave ($\boldsymbol{E}_{\text{ff}}$ and $\boldsymbol{E}_{\text{ff},3}$) and converts it to a pseudo-plane wave ($\boldsymbol{E}_{\text{BFP}}$). Useful unit vectors, angles, and lengths for the derivation in this section are labeled in the figure. (c) Positions of a dipole emitter relative to the RI interface (z_{SM}) and the nominal focal plane (z_f). (d-f) Representative intensity distributions at the BFP for SMs with orientations of (i) $\theta = 0°$, (ii) $[\theta, \phi] = [45°, 90°]$, and (iii) $[\theta, \phi] = [90°, 90°]$ when (d) the sample RI matches that of the lens immersion medium (1.515) and when the sample RI is (e) $n_2 = 1.33$ and (f) $n_2 = 1$. The numerical aperture is $\text{NA} = 1.4$. Colorbar: normalized intensity.

https://doi.org/10.1017/S0033583524000167 Published online by Cambridge University Press

chemical environment, and the possibility of relaxation into energy states other than S_0.

Methods for measuring the orientation of fluorescent molecules

Many methods have been developed to measure the orientation of fluorescent molecules (Rosenberg et al., 2005; Backlund et al., 2014). For example, one can simply add a polarizing beamsplitter (PBS) to a widefield microscope and measure linear dichroism (LD), given by

$$LD = \frac{\sum I_x - \sum I_y}{\sum I_x + \sum I_y}, \tag{10}$$

where $\sum I_x$ and $\sum I_y$ represent the total numbers of x- and y-polarized emission photons detected. The LD value is an implicit measure of emitter orientation. Further, it has been shown that the rotational mobility of an SM can be determined using the temporal autocorrelation of the LD value (fluorescence anisotropy correlation) (Zondervan et al., 2007). Testa et al. combined SMLM with polarization-sensitive fluorescence detection, showing that 2D histograms of x- and y-polarized fluorescence can reveal the rotational mobility of molecules, as demonstrated in living mammalian cells (Testa et al., 2008). However, despite its simplicity, LD suffers from orientational degeneracy, i.e., multiple molecular orientations produce the same LD value, e.g., zero in the cases of $\boldsymbol{\mu} = \left[\pm 1/\sqrt{2}, \pm 1/\sqrt{2}, 0\right]^\top$ and $\boldsymbol{\mu} = [0,0,1]^\top$. Increasing inclinations out of the xy-plane and increasing wobble also produce LD values closer to zero. To overcome these limitations, one can either manipulate the polarization and/or phase of the collected fluorescence photons (Fourkas, 2001; Rimoli et al., 2022) or measure the response of an emitter to various excitation polarizations over time (Forkey et al., 2003; Beausang et al., 2013; Backer et al., 2019), similar to measuring the polarization of scattered light under various illumination polarizations (Beckwith and Yang, 2021).

Another parameter associated with molecular orientation is fluorescence anisotropy, typically denoted by r (not to be confused with position $\boldsymbol{r}$) (Harms et al., 1999; Gradinaru et al., 2010). When a molecule is excited by linearly polarized light, fluorescence intensities collected along polarization directions parallel and orthogonal to the illumination are denoted $I_\parallel$ and $I_\perp$, respectively. The fluorescence anisotropy, given by $r = \left(I_\parallel - I_\perp\right)/\left(I_\parallel + 2I_\perp\right)$, quantifies the degree of rotation a molecule undergoes between absorption and emission. Although the orientation of a molecule cannot be directly measured, anisotropy is extremely sensitive to the rotation of the molecule. An anisotropy value of 0 indicates random emission polarization and free rotational motion, whereas an anisotropy value of 1 represents completely polarized emission from a rotationally fixed emitter. Gould et al. demonstrated (P)-FPALM, a method for simultaneously imaging the positions and anisotropies of single molecules under linearly polarized excitation light, enabling the study of molecular orientations within biological structures, such as mouse fibroblasts expressing Dendra2-actin or Dendra2-hemagglutinin (Gould et al., 2008).

A more sophisticated method for measuring molecular orientation involves measuring Stokes parameters (Alonso, 2023), e.g., by using a camera with an integrated polarizer above each pixel (Bruggeman et al., 2024) or by using a specific configuration of waveplates and polarizing beamsplitters (Mehta et al., 2016; Rimoli et al., 2022). Conventionally, the Stokes parameter s_0 characterizes light intensity, while s_1 through s_3 (s_8 for 3D Stokes parameters) describes light polarization. The degree of linear polarization (DoLP) and angle of linear polarization (AoLP) can be computed using (Bruggeman et al., 2024)

$$\mathrm{DoLP} = \sqrt{\frac{s_1^2 + s_2^2}{s_0^2}} \text{ and}$$

$$\mathrm{AoLP} = \frac{1}{2}\tan^{-1}\left(\frac{s_2}{s_1}\right), \tag{11}$$

where DoLP is determined by the polar angle θ, and AoLP is equal to the azimuthal angle ϕ. Further, there is an analogy between describing light polarization, which spans from linearly polarized to unpolarized, and the rotational dynamics of a molecule, which can be either fixed in a specific orientation or freely rotating. See "Modeling the rotational diffusion of fluorescent molecules" for more details.

In this section, we introduce two major categories of orientation-measurement methods: modulating the polarization of excitation light and detecting the polarization of the emitted fluorescence to measure the absorption dipole moment and modulating fluorescence emission to measure the emission dipole moment. As noted previously, although we classify these methods into absorption and emission-based, these two dipole moments are often coupled in practical experiments. In particular, the alignment of polarized excitation light with the absorption dipole moments can introduce a selection bias, thereby altering the observed distribution of emission dipole moments (Zhang et al., 2022; Munger et al., 2023), especially for slowly rotating molecules.

Excitation polarization modulation and polarization-sensitive detection were combined

The principle of measuring the orientation of the absorption dipole moment $\boldsymbol{\mu}_{\mathrm{abs}}$ using excitation modulation is as described by Eq. (5); an x-oriented molecule is most likely to absorb an x-polarized photon, and it is impossible for it to absorb a y- or z-polarized photon. The analogous statements are true for other polarization-orientation combinations.

Here, we denote $\boldsymbol{\mu}_{\mathrm{abs}}$ by $\boldsymbol{\mu}$ for simplicity. An SM is excited sequentially using illumination light of N unique polarizations $\boldsymbol{E}_1, \ldots, \boldsymbol{E}_N$. The expected total number of photons I_i, with $i \in \{1,2,\ldots,N\}$, detected from an SM excited by electric field polarization $\boldsymbol{E}_i$ is given by

$$I_i \propto \left| \begin{bmatrix} E_{x,i} & E_{y,i} & E_{z,i} \end{bmatrix} \begin{bmatrix} \mu_x & \mu_y & \mu_z \end{bmatrix}^\top \right|^2$$

$$= \begin{bmatrix} |E_{x,i}|^2 & |E_{y,i}|^2 & |E_{z,i}|^2 & 2\mathrm{Re}\{E_{x,i}^* E_{y,i}\} & 2\mathrm{Re}\{E_{x,i}^* E_{z,i}\} & 2\mathrm{Re}\{E_{y,i}^* E_{z,i}\} \end{bmatrix} \begin{bmatrix} \mu_x^2 \\ \mu_y^2 \\ \mu_z^2 \\ \mu_x\mu_y \\ \mu_x\mu_z \\ \mu_y\mu_z \end{bmatrix}. \tag{12}$$

Since each absorption and emission event arises from a specific molecular orientation $\boldsymbol{\mu}$ at time t, any intensity measured using a photon-counting detector can be written as a temporal average over the acquisition interval T. Therefore, we define the second-order moments $\boldsymbol{m} = \left[m_{xx}, m_{yy}, m_{zz}, m_{xy}, m_{xz}, m_{yz}\right]^\top$ of the transition dipole as

https://doi.org/10.1017/S0033583524000167 Published online by Cambridge University Press

$$m_{ij} = \frac{1}{T}\int_0^T \mu_i \mu_j \mathrm{d}t, \quad i,j \in \{x,y,z\}. \tag{13}$$

Further, assuming ergodicity, m_{ij} can also represent a corresponding average in orientation space. The forward imaging model is, therefore, given by

$$\boldsymbol{I} = s\begin{bmatrix} I_1 \\ I_2 \\ \vdots \\ I_N \end{bmatrix} = s\begin{bmatrix} |E_{x,1}|^2 & |E_{y,1}|^2 & |E_{z,1}|^2 & 2\mathrm{Re}\{E_{x,1}^* E_{y,1}\} & 2\mathrm{Re}\{E_{x,1}^* E_{z,1}\} & 2\mathrm{Re}\{E_{y,1}^* E_{z,1}\} \\ |E_{x,2}|^2 & |E_{y,2}|^2 & |E_{z,2}|^2 & 2\mathrm{Re}\{E_{x,2}^* E_{y,2}\} & 2\mathrm{Re}\{E_{x,2}^* E_{z,2}\} & 2\mathrm{Re}\{E_{y,3}^* E_{z,3}\} \\ \vdots & \vdots & \vdots & \vdots & \vdots & \vdots \\ |E_{x,N}|^2 & |E_{y,N}|^2 & |E_{z,N}|^2 & 2\mathrm{Re}\{E_{x,N}^* E_{y,N}\} & 2\mathrm{Re}\{E_{x,N}^* E_{z,N}\} & 2\mathrm{Re}\{E_{y,N}^* E_{z,N}\} \end{bmatrix} \begin{bmatrix} m_{xx} \\ m_{yy} \\ m_{zz} \\ m_{xy} \\ m_{xz} \\ m_{yz} \end{bmatrix}, \tag{14}$$

where s is the brightness scaling factor.

In the special case where the SMs are only excited by collimated epifluorescence illumination along the z direction (optical axis) (Backer et al., 2016), the z-polarized component $E_{z,i} = 0, \forall i$. This excitation method is only sensitive to the normalized projection of the orientational second moments into the xy plane, as given by

$$\zeta_{ij} = \frac{1}{T}\int_0^T \zeta_i \zeta_j dt \; i,j \in \{x,y\}, \tag{15}$$

where

$$\zeta_i = \frac{\mu_i}{\sqrt{\mu_x^2 + \mu_y^2}} \; i \in \{x,y\}. \tag{16}$$

The forward imaging model is simplified as

$$I = s\begin{bmatrix} |E_{x,1}|^2 & |E_{y,1}|^2 & 2\mathrm{Re}\{E_{x,1}^* E_{y,1}\} \\ |E_{x,2}|^2 & |E_{y,2}|^2 & 2\mathrm{Re}\{E_{x,2}^* E_{y,2}\} \\ \vdots & \vdots & \vdots \\ |E_{x,N}|^2 & |E_{y,N}|^2 & 2\mathrm{Re}\{E_{x,N}^* E_{y,N}\} \end{bmatrix} \begin{bmatrix} \zeta_{xx} \\ \zeta_{yy} \\ \zeta_{xy} \end{bmatrix}. \tag{17}$$

Using a series of fluorescence images obtained from varying angles of in-plane polarized excitation, achieved by continuously rotating a half-wave plate, Zhanghao et al. demonstrated super-resolution dipole orientation mapping in both fixed and live cells (Zhanghao et al., 2016). With three in-plane excitation polarizations that are 60° apart, Backer et al. achieved precisions of 2.5° for the azimuthal angle ϕ and 22 nm for lateral localization with 8424 signal photons and 158 background photons detected per pixel (Backer et al., 2016).

Note that even though solving the inverse problem associated with Eqs. (14) and (17) is computationally cheap, the main challenge using excitation modulation is that each SM needs to remain in the emissive state with a stable orientation for at least N sequential frames. One must also ensure that $\boldsymbol{E}_i$ is well known via careful calibration to obtain accurate measurements (Thorsen et al., 2022).

Another challenge of measuring the 3D orientation without measurement degeneracy using the method in Eq. (14) is the complex optical setup required for 3D polarization modulation (Thorsen et al., 2022). One method to overcome this challenge is to combine in-plane excitation polarization modulation [Eq. (17)] with polarized detection. Compared to only using LD [Eq. (10)], the addition of using x- and y-polarized excitation eliminates some measurement degeneracies. For example, the LD values for a rotationally fixed molecule with an orientation of $\boldsymbol{\mu} = \left[1/\sqrt{2}, 1/\sqrt{2}, 0\right]^\mathrm{T}$ and a freely wobbling molecule are both zero for unpolarized/circularly polarized excitation. In contrast, the LD value for an isotropic emitter is positive under x-polarized excitation and negative under y-polarized excitation, while the LD values are both zero for the fixed molecule under x- and y-polarized excitation. This method was recently used for measuring the structure of S-DNA (Backer et al., 2019). One can further increase the number of excitation and/or detection polarizations used to eliminate all orientation degeneracies. For example, 8 excitation polarizations and 2 detection polarizations were used to image the walking mechanics of Myosin V (Beausang et al., 2013). Note that since the detected intensities using this method are functions of both the absorption and emission dipole moments, any depolarization, e.g., intramolecular or intermolecular energy transfer (Figure 5c) (Carlsson et al., 1994), bending of the fluorescent molecule's backbone due to environmental interactions (Karedla et al., 2015), or rotation during the fluorescence lifetime (Figure 5d), may affect or bias the orientation and wobble measurements (Backer et al., 2019).

Another advantage of excitation polarization modulation is its compatibility with imaging modalities beyond SMOLM. A recently introduced approach known as MINFLUX-L (minimal photon fluxes – line-shaped dark spots) integrates excitation polarization modulation with MINFLUX (Zhan et al., 2022). This method uses linearly polarized line-shaped dark spots to probe molecules, thereby estimating 2D positions ($\sigma_{xy} = 12.3$ nm) and azimuthal angles ($\sigma_\phi = 26.6°$) using only 15 detected photons. Excitation modulation is also compatible with super-resolution techniques that image multiple fluorophores at once. For example, in optical lock-in detection super-resolution dipole orientation mapping (OLID-SDOM) (Guan et al., 2022), a continuously rotating excitation polarization is used to achieve background suppression and enable orientation measurements.

An attempt to achieve super-resolution using polarized excitation was proposed by Hafi et al. (2014). This method leverages the different responses of dipole emitters to varying excitation polarizations to distinguish between closely positioned molecules with different orientations and thereby improve resolution beyond the diffraction limit. However, its feasibility was questioned, especially when the orientation of emitters within a diffraction-limited area is homogeneous (Frahm and Keller, 2016). In response to these concerns, Hafi et al. acknowledged that the conditions necessary for resolution improvement via excitation polarization modulation require further investigation (Hafi et al., 2016).

Back focal plane imaging

To measure the emission dipole moment of fluorescent molecules, a forward imaging model that maps $\boldsymbol{\mu}_\mathrm{em}$ to the measurement space is required. The theory of image formation of dipole emitters has been discussed in many works (Böhmer and Enderlein, 2003; Lieb et al., 2004; Axelrod, 2012; Novotny and Hecht, 2012; Backer and Moerner, 2014, 2015; Chandler et al., 2019a). Here, we briefly derive the forward imaging model for two important cases that arise from Eq. (6): a matched case, where the SM is embedded within a homogeneous environment whose refractive index (RI) matches that of the objective lens immersion medium (Figure 6a), and a

https://doi.org/10.1017/S0033583524000167 Published online by Cambridge University Press

mismatched case, where the SM is embedded in a sample environment with an RI (n_2) different from that of the immersion medium (n_1, Figure 6b). For simplicity, we denote $\boldsymbol{\mu}_{\text{em}}$ by $\boldsymbol{\mu}$ in this section.

We first evaluate the case where the sample RI (n_1) matches that of the immersion medium (n_2). We denote the direction of the *s*- and *p*-polarized light using unit vectors (Figure 6a)

$$\boldsymbol{v}_s = [-\sin\phi_{\text{ff}} \quad \cos\phi_{\text{ff}} \quad 0]^\top \tag{18a}$$

$$\boldsymbol{v}_p = [\cos\theta_{\text{ff}}\cos\phi_{\text{ff}} \quad \cos\theta_{\text{ff}}\sin\phi_{\text{ff}} \quad -\sin\theta_{\text{ff}}]^\top, \tag{18b}$$

where θ_{ff} and ϕ_{ff} are the polar and azimuthal angles associated with the propagation direction $\hat{\boldsymbol{r}}_{\text{ff}}$ [Eq. (7)]. The far-field emission can be written as

$$\boldsymbol{E}_{\text{ff}} = A_s\boldsymbol{v}_s + A_p\boldsymbol{v}_p, \tag{19}$$

where scalars

$$A_s = \boldsymbol{v}_s \cdot \boldsymbol{E}_{\text{ff}} \text{ and} \tag{20a}$$

$$A_p = \boldsymbol{v}_p \cdot \boldsymbol{E}_{\text{ff}} \tag{20b}$$

represent the amplitudes of the *s*- and *p*-polarized light observed from direction $\hat{\boldsymbol{r}}_{\text{ff}}$, respectively. The objective lens collects this fluorescence and collimates it such that it propagates parallel to the optical axis. That is, *p*-polarized light within the sample is rotated to a polarization along the direction

$$\boldsymbol{v}_r = [\cos\phi_{\text{ff}},\ \sin\phi_{\text{ff}},\ 0]^\top \tag{21}$$

with polar coordinates within the back focal plane (BFP) expressed as $\rho_{\text{BFP}} = f_{\text{OL}}\sin\theta_{\text{ff}}$ and $\phi_{\text{BFP}} = \phi_{\text{ff}}$ and f_{OL} denoting the focal length of the objective lens. Therefore, the optical field at the BFP is given by

$$\begin{aligned}\boldsymbol{E}_{\text{BFP}}(\rho_{\text{BFP}},\phi_{\text{BFP}}) &= A_s\boldsymbol{v}_s + A_p\boldsymbol{v}_r \\ &= c_{\text{BFP}}\text{Circ}\left(\frac{\rho_{\text{BFP}}n_1}{f_{\text{OL}}\text{NA}}\right)(\cos\theta_{\text{ff}})^{-1/2}\left(\boldsymbol{v}_s\boldsymbol{v}_s^\top + \boldsymbol{v}_r\boldsymbol{v}_p^\top\right)(\mathbb{I} - \hat{\boldsymbol{r}}_{\text{ff}}\hat{\boldsymbol{r}}_{\text{ff}}^\top)\boldsymbol{\mu} \\ &= \boldsymbol{G}_{BFP}\boldsymbol{\mu},\end{aligned} \tag{22}$$

where the scalar c_{BFP} is a normalization factor (set to 1 here—the field may be normalized further) and NA is the numerical aperture of the objective. The circular indicator function $\text{Circ}(\rho)$ represents a finite aperture and is equal to 1 for $\rho < 1$ and 0 otherwise. The apodization factor $(\cos\theta_{\text{ff}})^{-1/2}$ maps the equal-angular distribution of energy in object space to a planar projection on the BFP while guaranteeing that the total energy entering the objective lens is identical to that within the BFP. That is,

$$\begin{aligned}&\int_{\phi_{\text{ff}}=0}^{2\pi}\int_{\theta_{\text{ff}}=0}^{\theta_0}|\boldsymbol{E}_{\text{ff}}|^2\sin\theta_{\text{ff}}\,\mathrm{d}\theta_{\text{ff}}\,\mathrm{d}\phi_{\text{ff}} \\ &= \int_{\phi_{\text{BFP}}=0}^{2\pi}\int_{\rho_{\text{BFP}}=0}^{f_{\text{OL}}\theta_0}|\boldsymbol{E}_{\text{BFP}}|^2\rho_{\text{BFP}}\,\mathrm{d}\rho_{\text{BFP}}\,\mathrm{d}\phi_{\text{BFP}},\end{aligned} \tag{23}$$

where

$$c_{\text{ff}}\sin\theta_{\text{ff}}\,\mathrm{d}\theta_{\text{ff}} = \left|(\cos\theta_{\text{ff}})^{-\frac{1}{2}}\right|^2 c_{\text{BFP}}\rho_{\text{BFP}}\,\mathrm{d}\rho_{\text{BFP}}. \tag{24}$$

Representative images of the intensity distribution given by Eq. (22) at the BFP for several molecular orientations are shown in Figure 6d.

Next, we evaluate the case when the sample RI differs from that of the immersion medium, which usually happens during typical biological imaging; the sample's RI is often close to that of water ($n_2 = 1.33$), whereas the immersion medium often has a larger RI (e.g., $n_1 = 1.515$) in order to achieve a higher collection NA. We define the following unit vectors (Figure 6b)

$$\boldsymbol{v}_{p,1} = [\cos\theta_{\text{ff},1}\cos\phi_{\text{ff}} \quad \cos\theta_{\text{ff},1}\sin\phi_{\text{ff}} \quad -\sin\theta_{\text{ff},1}]^\top \text{ and} \tag{25a}$$

$$\boldsymbol{v}_{p,2} = [\cos\theta_{\text{ff},2}\cos\phi_{\text{ff}} \quad \cos\theta_{\text{ff},2}\sin\phi_{\text{ff}} \quad -\sin\theta_{\text{ff},2}]^\top \tag{25b}$$

to represent the directions of *p*-polarized light within the lens immersion medium (n_1) and sample (n_2). Propagation directions $\theta_{\text{ff},1}$ and $\theta_{\text{ff},2}$ are related by

$$n_1\sin\theta_{\text{ff},1} = n_2\sin\theta_{\text{ff},2} \tag{26}$$

according to Snell's law. The polarization direction of the *s*-polarized light remains unchanged. The fields immediately before ($\boldsymbol{E}_{\text{ff},2}$) and after ($\boldsymbol{E}_{\text{ff},1}$) propagating through the RI interface are written as (Figure 6b)

$$\boldsymbol{E}_{\text{ff},2} = \frac{c_{\text{ff},2}}{\cos\theta_{\text{ff},2}}\left(\boldsymbol{v}_s^\top\boldsymbol{E}_{\text{ff},0}\boldsymbol{v}_s + \boldsymbol{v}_{p,2}^\top\boldsymbol{E}_{\text{ff},0}\boldsymbol{v}_{p,2}\right) \text{ and} \tag{27a}$$

$$\boldsymbol{E}_{\text{ff},1} = \frac{c_{\text{ff},2}}{\cos\theta_{\text{ff},2}}\left(t_s\boldsymbol{v}_s^\top\boldsymbol{E}_{\text{ff},0}\boldsymbol{v}_s + t_p\boldsymbol{v}_{p,2}^\top\boldsymbol{E}_{\text{ff},0}\boldsymbol{v}_{p,1}\right), \tag{27b}$$

where from Eq. (6), we have

$$\boldsymbol{E}_{\text{ff},0} = c_{\text{ff}}\left(\mathbb{I} - \hat{\boldsymbol{r}}_{\text{ff},2}\hat{\boldsymbol{r}}_{\text{ff},2}^\top\right)\boldsymbol{\mu}, \tag{28a}$$

$$\hat{\boldsymbol{r}}_{\text{ff},2} = [\sin\theta_{\text{ff},2}\cos\phi_{\text{ff}},\ \sin\theta_{\text{ff},2}\sin\phi_{\text{ff}},\ \cos\theta_{\text{ff},2}]^\top, \tag{28b}$$

$c_{\text{ff},2}$ is a normalization factor, and

$$t_s = \frac{2n_2\cos\theta_{\text{ff},2}}{n_1\cos\theta_{\text{ff},1} + n_2\cos\theta_{\text{ff},2}} \text{ and} \tag{29a}$$

$$t_p = \frac{2n_2\cos\theta_{\text{ff},2}}{n_1\cos\theta_{\text{ff},2} + n_2\cos\theta_{\text{ff},1}} \tag{29b}$$

are the Fresnel transmission coefficients for *s*- and *p*-polarized light. The field right before entering the objective lens is, therefore, given by

$$\boldsymbol{E}_{\text{ff},3} = \frac{c_{\text{ff},1}\cos\theta_{\text{ff},1}}{\cos\theta_{\text{ff},2}}\left(t_s\boldsymbol{v}_s^\top\boldsymbol{E}_{\text{ff},0}\boldsymbol{v}_s + t_p\boldsymbol{v}_{p,2}^\top\boldsymbol{E}_{\text{ff},0}\boldsymbol{v}_{p,1}\right), \tag{30}$$

where $\cos\theta_{\text{ff},1}$ and $\cos\theta_{\text{ff},2}$ represent the amplitude normalization factors corresponding to the spherical waves and $c_{\text{ff},1}$ (assumed to be 1 here) is a normalization factor. Similar to Eq. (22), accounting for the apodization factor, the optical field observed at the BFP is given by

$$\begin{aligned}&\boldsymbol{E}_{\text{BFP}}(u,v) \\ &= c_{\text{BFP}}\text{Circ}\left(\frac{\rho_{\text{BFP}}n_1}{f_{\text{OL}}\text{NA}}\right)\frac{(\cos\theta_{\text{ff},1})^{\frac{1}{2}}}{\cos\theta_{\text{ff},2}}\left(t_s\boldsymbol{v}_s\boldsymbol{v}_s^\top + t_p\boldsymbol{v}_r\boldsymbol{v}_{p,2}^\top\right)\left(\mathbb{I} - \hat{\boldsymbol{r}}_{\text{ff},2}\hat{\boldsymbol{r}}_{\text{ff},2}^\top\right) \\ &\boldsymbol{\mu} = \boldsymbol{G}_{\text{BFP}}\boldsymbol{\mu} \\ &= \begin{bmatrix} g_x^{(x)}(u,v) & g_y^{(x)}(u,v) & g_z^{(x)}(u,v) \\ g_x^{(y)}(u,v) & g_y^{(y)}(u,v) & g_z^{(y)}(u,v) \\ 0 & 0 & 0 \end{bmatrix}\boldsymbol{\mu},\end{aligned} \tag{31}$$

where

$$\rho_{\text{BFP}} = f_{\text{OL}}\sin\theta_{\text{ff},1}, \tag{32a}$$

$$u = \sin\theta_{\text{ff},1}\cos\phi_{\text{ff}}, \text{ and} \tag{32b}$$

https://doi.org/10.1017/S0033583524000167 Published online by Cambridge University Press

$$v = \sin\theta_{\mathrm{ff},1}\sin\phi_{\mathrm{ff}}. \tag{32c}$$

Entries $g_i^{(j)}$, with $i,j \in \{x,y,z\}$, are termed the (j-polarized) basis fields at the BFP. They represent the fields produced by x-, y-, and z-oriented dipoles, and any intermediate orientation $\boldsymbol{\mu}$ produces a linear combination of these basis fields g_i.

Finally, for a molecule located at $\boldsymbol{r} = [x,y,z_{\mathrm{SM}}]^{\top}$, where z_{SM} (Figure 6c) is the distance of the SM to the RI interface from above, the electric field at the BFP is given by

$$\begin{aligned}\boldsymbol{E}_{\mathrm{BFP}}(u,v;\boldsymbol{r},\boldsymbol{\mu}) &= \\ \exp\left[\frac{j2\pi}{\lambda}\left(n_1 xu + n_1 yv - n_1 z_f\cos\theta_{ff,1} + n_2 z_{\mathrm{SM}}\cos\theta_{ff,2}\right)\right]&\boldsymbol{G}_{\mathrm{BFP}}\boldsymbol{\mu} \\ = \exp\left\{\frac{j2\pi n_1}{\lambda}\left[xu + yv - z_f\sqrt{1-u^2-v^2} + z_{\mathrm{SM}}\sqrt{\left(\frac{n_2}{n_1}\right)^2 - u^2 - v^2}\right]\right\}&\boldsymbol{G}_{\mathrm{BFP}}\boldsymbol{\mu},\end{aligned} \tag{33}$$

where z_f represents the position of the nominal focal plane above the RI interface. We note that Eq. (33) assumes an ideal objective lens, and any (possibly field-dependent) optical aberrations (Fu et al., 2023; Liu et al., 2024; Xiao et al., 2024; Xu et al., 2020) can change the amplitude or phase or both of $\boldsymbol{E}_{\mathrm{BFP}}(u,v;\boldsymbol{r},\boldsymbol{\mu})$.

The intensity of x- and y-polarized fluorescence at the BFP is given by

$$\begin{bmatrix} I_x \\ I_y \end{bmatrix} = s\begin{bmatrix} \left|g_x^{(x)}\right|^2 & \left|g_y^{(x)}\right|^2 & \left|g_z^{(x)}\right|^2 & 2\mathrm{Re}\left\{g_x^{(x)*}g_y^{(x)}\right\} & 2\mathrm{Re}\left\{g_x^{(x)*}g_z^{(x)}\right\} & 2\mathrm{Re}\left\{g_y^{(x)*}g_z^{(x)}\right\} \\ \left|g_x^{(y)}\right|^2 & \left|g_y^{(y)}\right|^2 & \left|g_z^{(y)}\right|^2 & 2\mathrm{Re}\left\{g_x^{(y)*}g_y^{(y)}\right\} & 2\mathrm{Re}\left\{g_x^{(y)*}g_z^{(y)}\right\} & 2\mathrm{Re}\left\{g_y^{(y)*}g_z^{(y)}\right\} \end{bmatrix}\begin{bmatrix} m_{xx} \\ m_{yy} \\ m_{zz} \\ m_{xy} \\ m_{xz} \\ m_{yz} \end{bmatrix}. \tag{34}$$

Representative images of the intensity distribution given by Eqs. (31) and (32) at the BFP are shown in Figure 6e,f. The molecule is located at $\boldsymbol{r} = [0,0,0]^{\top}$ and the nominal focal plane position $z_f = 0$. The bright ring in these images represents the *supercritical* light coming from the evanescent fields near the SM that are transformed into propagating waves in the immersion medium (Axelrod, 2012). These intensity patterns can directly be used to measure the orientation of fluorophores (Lieb et al., 2004).

Modeling the rotational diffusion of fluorescent molecules

According to Eqs. (14) and (34), optical imaging is sensitive to the second-order orientational moments $\boldsymbol{m}$ of SMs instead of their first-order transition dipole moments $\boldsymbol{\mu}$. To interpret these values of $\boldsymbol{m}$, several models have been proposed to describe dipole orientation and wobble. One approach is to first rearrange the second moments into a 3 × 3 positive semidefinite (Zhou et al., 2024b) Hermitian matrix $\boldsymbol{M}$, which can be decomposed as

$$\begin{aligned}\boldsymbol{M} &= \begin{bmatrix} m_{xx} & m_{xy} & m_{xz} \\ m_{xy} & m_{yy} & m_{yz} \\ m_{xz} & m_{yz} & m_{zz} \end{bmatrix} = \sum\nolimits_{i=1}^{3}\lambda_i\boldsymbol{v}_i\boldsymbol{v}_i^{\top} \\ &= \frac{3\lambda_1 - 1}{2}\boldsymbol{v}_1\boldsymbol{v}_1^{\top} + \frac{3-3\lambda_1}{2}\frac{\mathbb{I}}{3} + \frac{\lambda_2-\lambda_3}{2}\left(\boldsymbol{v}_2\boldsymbol{v}_2^{\top} - \boldsymbol{v}_3\boldsymbol{v}_3^{\top}\right),\end{aligned} \tag{35}$$

where $\mathbb{I}$ represents the identity matrix and the scalars λ_i and vectors $\boldsymbol{v}_i$ correspond to the ith eigenvalue and eigenvector of $\boldsymbol{M}$, in the order of descending λ_i. Therefore, the second moments $\boldsymbol{M}$ perceived by the imaging system may be interpreted as a weighted mixture of several components: a fixed dipole of orientation $\boldsymbol{\mu} = \boldsymbol{v}_1$, an isotropic emitter ($\mathbb{I}/3$), and an orthogonal nuisance term that arises from asymmetric rotation.

If the molecule diffuses in all directions equally (Zhang and Lew, 2019), thereby exhibiting *isotropic* rotational diffusion, then the smaller eigenvalues λ_2 and λ_3 are identical. We may define rotational constraint $\gamma = (3\lambda_1 - 1)/2$ such that

$$\boldsymbol{M} = \gamma\boldsymbol{v}_1\boldsymbol{v}_1^{\top} + \frac{1-\gamma}{3}\mathbb{I}, \tag{36}$$

where the individual second moments are given by

$$m_{ii} = \gamma\mu_i^2 + \frac{1-\gamma}{3} \text{ and}$$

$$m_{ij} = \gamma\mu_i\mu_j, \quad i,j \in \{x,y,z\}, i \neq j. \tag{37}$$

The rotational constraint $\gamma \in [0,1]$ represents the degree to which the molecule's emission is consistent with a fixed dipole (Backer and Moerner, 2014, 2015; Backer et al., 2016); $\gamma = 0$ represents an isotropic emitter. We may parameterize this isotropic rotational diffusion as uniform wobble within a hard-edged cone of half angle α_s, and thus, γ can be written as

$$\begin{aligned}\gamma &= 1 - 3m_{xx}|_{\mathbf{v}_1=[0,0,1]^{\top}} \\ &= 1 - \frac{3\int_0^{\alpha_s}\int_0^{2\pi}(\sin\theta'\cos\phi')^2\sin\theta'\,d\phi'\,d\theta'}{\int_0^{\alpha_s}\int_0^{2\pi}\sin\theta'\,d\phi'\,d\theta'} = \frac{\cos^2\alpha_s + \cos\alpha_s}{2}.\end{aligned} \tag{38}$$

Alternatively, Eq. (38) is equivalent to

$$\gamma = 1 - \frac{3\Omega}{4\pi} + \frac{\Omega^2}{8\pi^2}, \tag{39}$$

where $\Omega \in [0,2\pi]$ represents the solid angle subtended by the cone on the orientation hemisphere (Figure 5a). A rotationally fixed molecule has a cone solid angle of 0, while a freely rotating molecule has $\Omega = 2\pi$.

Ding et al. and Zhou et al. further investigated molecules exhibiting *anisotropic* wobble, specifically focusing on scenarios where the eigenvalues λ_2 and λ_3 are not identical (Ding and Lew, 2021; Zhou et al., 2024b). In these cases, one may consider a molecule wobbling uniformly within an elliptical cone of distinct angles of α and β along the long and short axes, respectively. The eigenvalues (Eq. (35)) can be expressed as

$$\lambda_1 = \frac{1}{3\Omega}\int_{\phi'=0}^{2\pi} 1 - t^3(\phi')\,d\phi',$$

$$\lambda_2 = \frac{1}{3\Omega}\int_{\phi'=0}^{2\pi}\left(t^3(\phi') - 3t(\phi') + 2\right)\sin^2(\phi')\,d\phi',$$

$$\lambda_3 = \frac{1}{3\Omega}\int_{\phi'=0}^{2\pi}\left(t^3(\phi') - 3t(\phi') + 2\right)\cos^2(\phi')\,d\phi',$$

https://doi.org/10.1017/S0033583524000167 Published online by Cambridge University Press

$$\Omega = 2\pi - \int_{\phi'=0}^{2\pi} t(\phi')\mathrm{d}\phi', \text{ and}$$

$$t(\phi') = \cos(\max\theta(\phi)) = \sqrt{1 - \frac{\sin^2(\alpha) + \sin^2(\beta)}{\sin^2(\beta)\cos^2(\phi) + \sin^2(\alpha)\sin^2(\phi)}}, \tag{40}$$

where $\max\theta(\phi)$ represents the boundary of the anisotropic wobble cone, rotated so that its center points along the μ_z axis, parameterized by the maximum value of θ as a function of ϕ. The corresponding eigenvectors are given by

$$\boldsymbol{v}_2 = \begin{bmatrix} -\cos\theta\cos\phi\sin\psi - \sin\phi\cos\psi \\ -\cos\theta\sin\phi\sin\psi + \cos\phi\cos\psi \\ \sin\theta\sin\psi \end{bmatrix} \text{ and}$$

$$\boldsymbol{v}_3 = \begin{bmatrix} \cos\theta\cos\phi\cos\psi - \sin\phi\sin\psi \\ \cos\theta\sin\phi\cos\psi - \cos\phi\sin\psi \\ -\sin\theta\cos\psi \end{bmatrix}. \tag{41}$$

One may model the anisotropy as having long and short axes oriented parallel and perpendicular to the optical axis (Figure 5e) or rotated by an arbitrary angle ψ (Figure 5f). Importantly, one may interpret the eigen decomposition of $\boldsymbol{M}$ as expressing $\boldsymbol{m}$ in a rotated coordinate system with μ_z' aligned with the dipole's mean orientation and an equivalent second moment vector $\boldsymbol{m}' = [\lambda_3,\lambda_2,\lambda_1,0,0,0]^\mathsf{T}$. Therefore, the eigenvalues are simply equal to the first three squared second moments, each of which must be non-negative (Zhou et al., 2024b).

Alternatively, rotational dynamics can be expressed using generalized 3D Stokes parameters s_i, analogous to those used in standard polarimetry (Curcio et al., 2020). The relationship between the second moments and the Stokes parameters is given by

$$s_1 = 2s_0\left(m_{xx} - m_{yy}\right),$$

$$\begin{bmatrix} s_2 & s_4 & s_6 \end{bmatrix} = 2s_0\begin{bmatrix} m_{xy} & m_{xz} & m_{yz} \end{bmatrix},$$

$$s_3 = s_5 = s_7 = 0,$$

$$s_8 = \sqrt{3}s_0\left(m_{xx} + m_{yy} - m_{zz}\right)/2. \tag{42}$$

Note that s_3, s_5, and s_7 are zero since we assume that the SMs have no chirality. We also note that spherical harmonics $Y_l^m(\theta,\phi)$ may also be used as a basis to describe molecular rotational dynamics (Chandler et al., 2019b). These harmonics are convenient as a complete orthogonal basis for functions on a sphere, and they form the foundation of a unified framework for analyzing the image formation of individual dipoles and ensembles thereof (Chandler et al., 2019a, 2019b, 2020). Compared to fluorescence anisotropy, which projects orientation space into a single parameter, each of the aforementioned models provides a more detailed, high-dimensional description of SM rotational motions, and we recommend their use whenever possible.

This analysis has key implications for the temporal resolution of SMOLM techniques. Since any fluorescence measurement involves collecting some number of photons over time, SMOLM wobble measurements, quantified via rotational constraint γ or angles α_s, α, and β, therefore represent the degree of rotational diffusion that a molecule exhibits during the integration time. The choice of integration time typically balances several factors, including the duration of each fluorescence burst or fluorophore binding event, hardware limitations of the detector, and the desired angular precision of the measurement. Typical exposure times are 10 to 100 milliseconds for widefield imaging cameras (Table 1), which are useful for probing binding, phase separation, and aggregation dynamics (Nettels et al., 2024). Newly developed arrays of avalanche diodes have <200 ps precision (Bucci et al., 2024; Radmacher et al., 2024) for timing photon arrivals and can be adapted for SMOLM. Further, one may use SMOLM to track a molecule's mean orientation $\boldsymbol{\mu}$ and wobble γ, as well as its translational movements, over time, thereby enabling high-dimensional tracking of biomolecular dynamics.

Dipole-spread function engineering via modulating phase and polarization

The optical field at the image plane can be found by calculating the Fourier transform of the (modulated) field at the BFP (Figure 6d–f). Here, we denote any possible linear operation on the field at the BFP using a spatially varying Jones matrix

$$\boldsymbol{J}(u,v) = \begin{bmatrix} J_{11}(u,v) & J_{12}(u,v) \\ J_{21}(u,v) & J_{22}(u,v) \end{bmatrix}. \tag{43}$$

The image plane electric field for an in-focus emitter located at the origin ($x = y = z_{\mathrm{SM}} = z_f = 0$) is therefore given by

$$\begin{aligned} \boldsymbol{E}_{\mathrm{img}}(\xi,\eta) &= \mathcal{F}\{\boldsymbol{J}\boldsymbol{G}_{\mathrm{BFP}}\boldsymbol{\mu}\} = \mathcal{F}\{\boldsymbol{J}\boldsymbol{G}_{\mathrm{BFP}}\}\boldsymbol{\mu} = \boldsymbol{G}_{\mathrm{img}}\boldsymbol{\mu} \\ &= \begin{bmatrix} G_x^{(x)}(\xi,\eta) & G_y^{(x)}(\xi,\eta) & G_z^{(x)}(\xi,\eta) \\ G_x^{(y)}(\xi,\eta) & G_y^{(y)}(\xi,\eta) & G_z^{(y)}(\xi,\eta) \\ 0 & 0 & 0 \end{bmatrix}\boldsymbol{\mu}, \end{aligned} \tag{44}$$

where (ξ,η) represents coordinates within the image plane and $\mathcal{F}\{\cdot\}$ represents a 2D Fourier transform performed by the tube lens [TL1 and TL2, Figure 7a]. Entries $G_i^{(j)}$, with $i,j \in \{x,y,z\}$, are termed the basis fields at the image plane. Note that due to the Fourier transform, $\boldsymbol{E}_{\mathrm{img}}$ is shift-invariant with respect to the lateral position (x,y) of the molecule. However, the basis fields exhibit changes in their shapes when the molecule is defocused.

Similar to Eqs. (14) and (34), the forward imaging model using emission modulation can be written as

$$\begin{aligned} \boldsymbol{I} &= \begin{bmatrix} I^{(x)} \\ I^{(y)} \end{bmatrix} = s\begin{bmatrix} B_{xx}^{(x)} & B_{yy}^{(x)} & B_{zz}^{(x)} & B_{xy}^{(x)} & B_{xz}^{(x)} & B_{yz}^{(x)} \\ B_{xx}^{(y)} & B_{yy}^{(y)} & B_{zz}^{(y)} & B_{xy}^{(y)} & B_{xz}^{(y)} & B_{yz}^{(y)} \end{bmatrix}\boldsymbol{m} = s\boldsymbol{B}\boldsymbol{m} \\ &= s\begin{bmatrix} \left|G_x^{(x)}\right|^2 & \left|G_y^{(x)}\right|^2 & \left|G_z^{(x)}\right|^2 & 2\mathrm{Re}\left\{G_x^{(x)*}G_y^{(x)}\right\} & 2\mathrm{Re}\left\{G_x^{(x)*}G_z^{(x)}\right\} & 2\mathrm{Re}\left\{G_y^{(x)*}G_z^{(x)}\right\} \\ \left|G_x^{(y)}\right|^2 & \left|G_y^{(y)}\right|^2 & \left|G_z^{(y)}\right|^2 & 2\mathrm{Re}\left\{G_x^{(y)*}G_y^{(y)}\right\} & 2\mathrm{Re}\left\{G_x^{(y)*}G_z^{(y)}\right\} & 2\mathrm{Re}\left\{G_y^{(y)*}G_z^{(y)}\right\} \end{bmatrix}\begin{bmatrix} m_{xx} \\ m_{yy} \\ m_{zz} \\ m_{xy} \\ m_{xz} \\ m_{yz} \end{bmatrix}, \end{aligned} \tag{45}$$

where $B_{ij}^{(k)}$, with $i,j \in \{x,y,z\}$ and $k \in \{x,y\}$, are termed the k-polarized basis images describing the response (dipole spread function, DSF) of the imaging system to a dipole emitter. For unpolarized detection, the detected image is given by $I^{(x)} + I^{(y)}$, a mixture of both polarized images. We can also resolve $I^{(x)}$ and $I^{(y)}$ separately by placing a PBS in the emission path (Figure 7a).

For an unpolarized conventional microscope without additional modulation at the BFP, i.e., $J_{11}(u,v) = J_{22}(u,v) = 1$ and $J_{12}(u,v) = J_{21}(u,v) = 0$, SM orientation can be measured by fitting the shape of the measured images to the theoretical model [Figure 7b (i)] (Mortensen et al., 2010); the image corresponding to an in-(xy)

https://doi.org/10.1017/S0033583524000167 Published online by Cambridge University Press

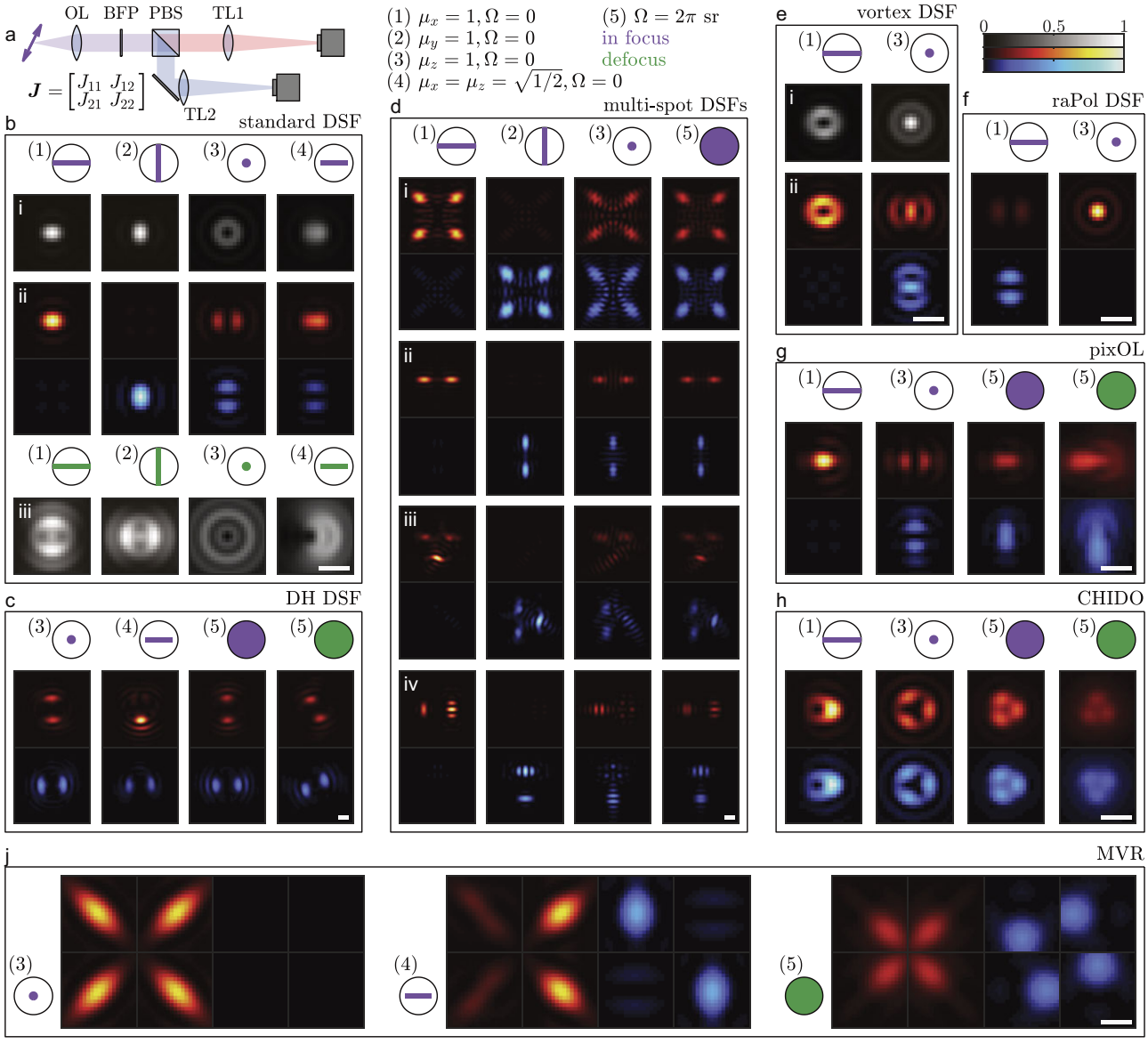

Figure 7. Representative images of recently developed and widely used dipole spread functions (DSFs). (a) Principle of a fluorescence microscope with polarized detection using a polarizing beamsplitter (PBS). An objective lens (OL) is placed at one focal length away from the dipole emitter. The tube lenses (TL1, TL2) perform optical Fourier transforms on the field at the back focal plane (BFP) modulated by an optical component represented by a 2×2 complex tensor $\boldsymbol{J}(u,v)$ and create the DSF at the detector plane. Images for molecules with various orientations and wobble using the (b) standard DSF (i) unpolarized and focused (Mortensen et al., 2010), (ii) polarized and focused (Ding et al., 2020), (iii) unpolarized and defocused (Böhmer and Enderlein, 2003), (c) double-helix DSF, (d) multi-spot DSFs (i–iv) quadrated (Backer et al., 2013), bisected (Backer et al., 2014), tri-spot (Zhang et al., 2018), duo-spot (Lu et al., 2020 DSFs), (e) vortex DSF (Ding and Lew, 2021; Hulleman et al., 2021), (f) radially and azimuthally polarized (raPol) standard DSF (Zhang et al., 2022), (g) pixOL (Wu et al., 2022a), and (h) CHIDO (Curcio et al., 2020). (j) Images from eight channels of the multi-view-reflector (MVR) microscope (Zhang et al., 2023). Molecule with (1) $[\theta,\phi] = [90°, 0°]$, (2) $[\theta,\phi] = [90°, 90°]$, (3) $\theta = 0°$, and (4) $[\theta,\phi] = [45°, 0°]$. (5) Isotropic emitter. Purple: in-focus molecules; green: molecules defocused by (b) 500 nm and (c–h) 200 nm. Color bar: normalized intensity; scale bar: 500 nm.

plane molecule exhibits an elliptical shape with an elongation direction parallel to the molecular orientation [Figure 7b(i)(1,2)] while the image corresponding to a z-oriented molecule exhibits a donut shape [Figure 7b(i)(3)]. One can also separate the x- and y-polarized emission light to obtain more distinct basis images for x- and y-oriented molecules [Figure 7b(ii)(1,2)]. This polarization-resolved DSF was used to resolve the structural heterogeneity within amyloid aggregates (Ding et al., 2020). Both the unpolarized and polarized standard DSFs are typically implemented to image molecules located close to the air-glass or water–glass interface because the additional phase caused by refractive index mismatch further improves orientational sensitivity by breaking the symmetry in the basis fields (Ding et al., 2020; Zhang and Lew, 2021b). The standard DSF can also be implemented with a defocus of ~500 nm to 1 μm (Böhmer and Enderlein, 2003). While localization precision is reduced as the photons are spread across a larger area, the more distinct images [Figure 7b(iii)] significantly improve orientational sensitivity. Defocused imaging has been used for imaging rotations of SMs embedded within polymers (Dickson et al., 1998; Patra et al., 2004; Uji-i et al., 2006) and resolving the stepping of Myosin V motors (Toprak et al., 2006).

https://doi.org/10.1017/S0033583524000167 Published online by Cambridge University Press

Engineering phase masks

Since the early 1980s (Cathey et al., 1984; Dowski and Cathey, 1995; Ojeda-Castañeda et al., 1986), point-spread function (PSF) engineering has been explored to extend the capabilities of conventional microscopes. In the case of SMOLM, by manipulating the optical field at the BFP using a spatially varying Jones matrix $\boldsymbol{J}(u,v)$, one can improve the orientational sensitivity of the microscope and make more accurate and precise measurements. Experimentally, engineered DSFs are often implemented by adding a 4f system to the detection path of a fluorescence microscope that facilitates easy access to the BFP. Many DSFs, e.g., the double-helix (DH) DSF (Pavani and Piestun, 2008; Pavani et al., 2009; Backlund et al., 2012), multi-spot DSFs (Backer et al., 2013, 2014; Zhang et al., 2018; Lu et al., 2020), vortex DSFs (Ding and Lew, 2021; Hulleman et al., 2021), and pixel-wise optimized DSF (Wu et al., 2022a) engineered for measuring 3D orientation and localization (pixOL), are designed using phase-only modulation, i.e.,

$$J_{11}(u,v) = \exp[jk\psi_x(u,v)],$$

$$J_{22}(u,v) = \exp\left[jk\psi_y(u,v)\right], \text{ and}$$

$$J_{12}(u,v) = J_{21}(u,v) = 0, \tag{46}$$

where $\psi_x(u,v)$ and $\psi_y(u,v)$ are the additional phase masks added to the x and y-polarized BFP, respectively. These DSFs can be implemented using a single spatial light modulator in a 4f system (Figure 8a,b), as shown in (Backlund et al., 2012; Backer et al., 2014; Zhang et al., 2018). In this configuration, the phase masks $\psi_x(u,v)$ and $\psi_y(u,v)$ may simply be rotated versions of each other.

The double-helix (DH) DSF was originally designed for measuring the axial position z_{SM} of SMs (Pavani and Piestun, 2008; Pavani et al., 2009); the image of a single emitter exhibits two lobes revolving around each other as a function of z_{SM}. It may be implemented using an SLM or by placing a commercially available transmissive phase plate (Gahlmann et al., 2013) in the BFP of an imaging system. The orientation information is encoded in the relative brightness of the lobes (Backlund et al., 2012). For example, in the x-polarized imaging channel, one lobe is significantly brighter compared to the other if the molecule is tilted within the xz-plane by ~ 45° [Figure 7c(4)]. In their work, the authors note that by simultaneously estimating the position and orientation of SMs using the DH DSF, orientation-induced systematic localization errors (Engelhardt et al., 2011) may be greatly improved; the experimental standard deviation averaged over a 2 μm depth range is reduced from 116 nm to 34 nm with 5925 signal photons and 9 background photons per pixel detected. One limitation of the DH DSF is that the image of z-oriented molecules is difficult to distinguish from those of isotropic emitters [Figure 7c(3,5)]. Consequently, the authors note that their localization correction works best for intermediately inclined molecules, i.e., $\theta \in [35°, 75°]$.

The design of another family of DSFs, the multi-spot DSFs, leverages the fact that the intensity distribution at the BFP changes as a function of molecular orientation (Figure 7d). These techniques segment the BFP into multiple sections, and various linear phase ramps are placed in these sections. Since the Fourier transform of a linear phase gradient is a lateral shift of the kernel, the additional phase creates a multi-spot DSF at the image plane, where each spot exhibits a lateral shift depending on the phase ramp in the corresponding area at the BFP. Intuitively, orientation information is encoded in the relative brightness between the spots, similar to the DH DSF.

Two early methods, the quadrated [Figure 7d(i)] (Backer et al., 2013) and bisected [Figure 7d(ii)] (Backer et al., 2014) DSFs, both use a symmetric partitioning strategy. The quadrated DSF imaged dicyanomethylenedihydrofuran-N-6 (DCDHF-N-6) molecules embedded within polymethyl methacrylate (PMMA) with orientation precisions of $\sigma_\theta = 1.8°$ and $\sigma_\phi = 1.7°$ and 2370 photons detected. The bisected DSF is resolved by the 3D position and orientation of SMs attached to microtubules in a BSC-1 cell within an axial range of 500 nm. Similar to the DH DSF, the bisected DSF can also remove orientation-induced localization errors and resolve the axial position z of an SM using the relative positions of its spots. However, both the quadrated and bisected DSFs exhibit an orientational degeneracy when distinguishing between z-oriented molecules versus isotropic emitters. The tri-spot DSF [Figure 7d(iii)] (Zhang et al., 2018) was later developed to eliminate the degeneracy by creating six linearly independent basis images; i.e., six spots within the image plane are used to estimate all six second-order orientational moments $\boldsymbol{m}$. Therefore, it can measure not only the orientation but also the rotational "wobble" of a molecule within a cone of solid angle Ω during a camera frame (see Modeling the rotational diffusion of fluorescent molecules for details). It was used to resolve anisotropic emission from fluorescent beads and SMs embedded within polymers, as well as SM orientation and wobble dynamics within supported lipid membranes (Lu et al., 2020). Precisions of $\sigma_\theta = 6.0°$ and $\sigma_\phi = 10.6°$ for measuring orientation and $\sigma_\Omega = 0.11\pi$ sr for measuring the wobble cone angle were reported for 1300 signal photons and 5 background photons per pixel detected. The duo-spot DSF [Figure 7d(iv)] (Lu et al., 2020) was also designed based on the intensity distribution at the BFP specifically for distinguishing in-plane molecules from z-oriented molecules. For in-plane molecules, two spots with similar brightness were observed in each polarization channel [Figure 7d(iv)

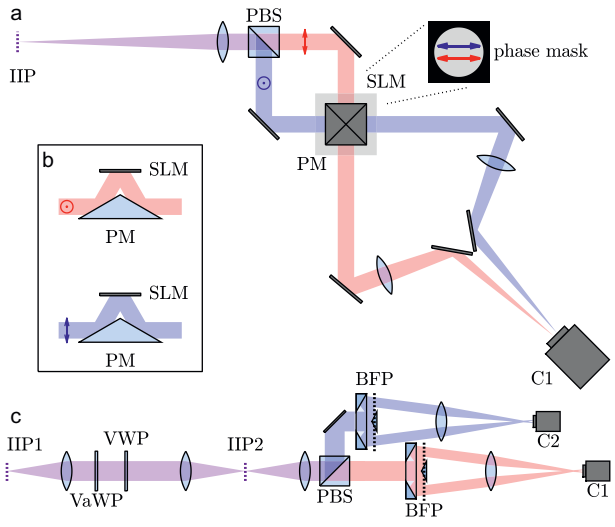

Figure 8. (a, b) Schematic of a polarization-sensitive 4f imaging system appended to the detection path of a fluorescence microscope for modulating the phase at the back focal plane (BFP) using a spatial light modulator (SLM). (a) After separating the x (red) and y (blue) polarized fluorescence using a polarizing beamsplitter (PBS), light is guided towards a pyramid mirror and (b) reflected upwards towards the SLM. Both x and y-polarized BFP are positioned at the same area on the SLM. Arrows on the phase mask represent the light polarization on the SLM. Both imaging channels are collected using camera C1. (c) Schematic of the raMVR microscope. After turning radially and azimuthally polarized fluorescence to x- and y-polarized light using a variable wave plate (VaWP) and a vortex wave plate (VWP), a PBS and two sets of pyramid mirrors separate lights into eight detection channels, captured by cameras C1 and C2.

https://doi.org/10.1017/S0033583524000167 Published online by Cambridge University Press

(1,2)]; for z-oriented molecules, only one spot in each channel will be detected [Figure 7d(iv)(3)]. It was also used in lipid membrane imaging, yielding precisions of $\sigma_\theta = 8.4^\circ$, $\sigma_\phi = 21.8^\circ$, and $\sigma_\Omega = 0.16\pi$ sr with 950 signal photons and 5 background photons per pixel detected.

The vortex DSF is implemented by adding a vortex phase plate, which is usually used in STED microscopy to create a donut-shaped depletion laser pattern, to the emission path. The features of this DSF are opposite of those of the standard DSF (Figure 7b); images corresponding to in-plane molecules exhibit a donut shape [Figure 7e(1)], whereas images corresponding to z-oriented molecules are single-focused spots [Figure 7e(3)]. The orientational measurement precisions of both the unpolarized [Figure 7e(i)] (Hulleman et al., 2021) and (x and y) polarized [Figure 7e(ii)] (Ding and Lew 2021) vortex DSFs are superior to those of the analogous standard DSFs. The unpolarized vortex DSF was used to resolve different periodicities of plectoneme structures where two helices intertwine with each other within supercoiled DNA. Imaging λ-DNA on a tilted coverslip, it achieved an orientation precision of $\sigma_\theta = 3.1^\circ$, $\sigma_\phi = 5.5^\circ$, and a wobble precision of $\sigma_\Omega = 0.37$ sr (converted from the published measurements), as well as localization precisions of $\sigma_{xy} = 5.6$ nm along the lateral direction and $\sigma_z = 27$ nm along the axial direction with 4000 signal photons and 10 background photons/pixel detected (Hulleman et al., 2021). The polarized vortex DSF achieves orientation precisions of $\sigma_\theta = 4.5^\circ$ and $\sigma_\phi = 7.7^\circ$ and a lateral localization precision of $\sigma_{xy} = 12.5$ nm with 510 signal photons and 2.3 background photons/pixel detected. Further, the authors show that this DSF is capable of resolving *anisotropic* wobbling, i.e., a molecule that diffuses rotationally within an *elliptical* cone (Zhou et al., 2024b), within a single camera frame (see Modeling the rotational diffusion of fluorescent molecules for details). They find that NR molecules bound within DPPC SLBs tend to wobble along the direction parallel to acyl chains; whereas those bound to Aβ42 oligomers exhibit a wide distribution for wobble anisotropy.

Another phase mask was designed by numerical optimization, i.e., maximizing the Fisher information (Moon and Stirling, 2000) of measuring the orientational second moments, similar to that used to create the tetrapod DSF (Shechtman et al., 2015) for 3D SMLM. This method, termed pixel-wise DSF engineering for measuring the 3D orientation and localization (pixOL) (Wu et al., 2022a), produced a phase mask with a smaller phase gradient compared to other engineered phase masks. The basis images exhibit similar features to those of the x and y-polarized (xyPol) standard DSF when in focus (Figure 7g, purple). However, it breaks the defocus symmetry of the standard DSF and is more suitable for 3D imaging (Figure 7g, green). Over a 700 nm depth range, the pixOL DSF achieves an orientation precision of $\sigma_{\boldsymbol{\mu}} = 4.1^\circ$ (an arc length on the orientation unit sphere, i.e., a geometric average between σ_θ and σ_ϕ that accounts for their correlation), a wobble precision of $\sigma_\Omega = 0.44$ sr, and localization precisions of $\sigma_{xy} = 23.2$ nm along the lateral direction and $\sigma_z = 19.5$ nm with 2500 signal photons and 3 background photons/pixel detected. As a proof of principle, the authors demonstrate this DSF by imaging NR molecules bound within a spherical SLB consisting of DPPC and 40% cholesterol. The pixOL measurements showed that NR molecules are highly constrained to an orientation perpendicular to the membrane—an ideal calibration target for 3D SMOLM.

Beyond classical optimization, machine learning can also be used for phase mask design in a manner similar to technologies developed for 3D SMLM (Nehme et al., 2020). Here, the goal is to use deep learning to explore the high dimensional design space robustly and construct a phase mask that is optimal for a specific measurement task; i.e., the optimized design achieves a minimized error rate. Jointly minimizing the error of measuring 3D position and 3D orientation, Jouchet et al. used this technique to produce the Arrowhead phase mask (Jouchet et al., 2023). Imaging single DCDHF-N-6 molecules within PMMA, the arrowhead mask achieves experimental precisions of $\sigma_{\boldsymbol{\mu}} = 4.3^\circ$ for orientation, $\sigma_{xy} = 11$ nm for lateral position, and $\sigma_z = 33.6$ nm for axial position with a median of 3900 signal photons and 80 background photons/pixel detected (see Image analysis methods for details on Arrowhead DSF analysis and estimation).

Polarization modulation

Besides modulating the phase at the BFP, one can also manipulate fluorescence polarization, i.e., apply spatially varying polarization rotation in the BFP before polarization splitting, to measure SM orientation. In this case, the cross elements $J_{12}(u,v)$ and $J_{21}(u,v)$ are no longer zero. For polarization-only modulation, the optical component can be described by a spatially varying *real* tensor, e.g., separating the radially and azimuthally polarized fluorescence by placing a vortex (half) wave plate (Zhang et al., 2022), or equivalently, a y-phi mask (Backlund et al., 2016) or two SLMs (Hashimoto et al., 2015), at the BFP. The design rationale is based on the toroidal emission pattern of dipole emitters; a molecule oriented along the optical axis z emits radially polarized light. Separating the radially polarized light from the azimuthal polarization improves one's sensitivity to detect changes in polar angle; the relevant real tensor is given by

$$\boldsymbol{J} = \begin{bmatrix} \cos\phi_{\mathrm{ff}} & \sin\phi_{\mathrm{ff}} \\ -\sin\phi_{\mathrm{ff}} & \cos\phi_{\mathrm{ff}} \end{bmatrix}. \tag{47}$$

This method, termed the radially and azimuthally polarized (raPol) standard DSF (Zhang et al., 2022), exhibits excellent orientation measurement performance; with 5000 signal photons and 30 background photons/pixel detected, it achieves precisions of $\sigma_\theta = 1.7^\circ$, $\sigma_\phi = 1.4^\circ$, and $\sigma_\Omega = 0.16$ sr. Further, due to its more compact size compared to other engineered DSFs (Figure 7f), it exhibits a localization precision of $\sigma_{xy} = 2.2$ nm under the aforementioned SBR, comparable to that using the x and y polarized standard DSF. Its detectability under low SBR is also comparable to xyPol and is superior to those of other engineered DSFs. It has been shown that measuring molecule locations in the azimuthally polarized channel removes orientation-induced localization bias (Backlund et al., 2016). Given its superior sensitivity to detecting z-oriented molecules [Figure 7f(3)] and excellent localization and orientation precision (Zhang and Lew, 2021b), it was used to image NR molecules within planar SLBs and resolved coupling between absorption and emission dipole orientations. It also detected changes in translational and rotational diffusions of NR molecules induced by cholesterol (Zhang et al., 2022).

The recently introduced Multi-View Reflector (MVR) microscope (Figure 7j) further extends SMOLM's capabilities (Zhang et al., 2023). In addition to separating radially and azimuthally polarized fluorescence, it incorporates two sets of pyramid mirrors to split light at the BFP and creates eight detection channels. The system's DSF exhibits similar characteristics to multi-spot DSFs; the relative intensity and position of spots within each channel

https://doi.org/10.1017/S0033583524000167 Published online by Cambridge University Press

indicate the orientation and axial position of the emitter, respectively. Despite the complexity of this system (Figure 8c), it showcases remarkable robustness to background fluorescence; since background photons are spread across the eight detection channels along with the signal photons, its effective SBR is better than those of multi-spot DSFs. While imaging SLBs on silica spheres, the MVR microscope experimentally achieves an isotropic 3D localization precision of 10.9 nm and orientation precision of 2.0° across a 1.5-micron axial range. It also showed great robustness against aberrations induced by refractive-index mismatches and was used for studying Aβ42-membrane interactions and heterogeneities in fixed HEK-293T cell membranes.

Unlike phase-only and polarization-only modulations of the fluorescence at the BFP, Coordinate and Height super-resolution Imaging with Dithering and Orientation (CHIDO) (Ramkhalawon et al., 2013; Vella and Alonso, 2019; Curcio et al., 2020) uses a single stressed-engineered optic (SEO) to modulate both phase and polarization simultaneously. Its complex tensor is given by

$$\boldsymbol{J} = \cos\left(\frac{c_{\mathrm{st}}\rho_{\mathrm{BFP}}}{2}\right)\begin{bmatrix}1 & 0\\ 0 & 1\end{bmatrix} + j\sin\left(\frac{c_{\mathrm{st}}\rho_{\mathrm{BFP}}}{2}\right)\begin{bmatrix}\cos\phi_{\mathrm{ff}} & -\sin\phi_{\mathrm{ff}}\\ -\sin\phi_{\mathrm{ff}} & -\cos\phi_{\mathrm{ff}}\end{bmatrix}. \tag{48}$$

It creates a set of linearly independent basis images that rotate when a molecule is defocused (Figure 7h). The precise features and the performance of this DSF depend on the stress coefficient c_{st} (1.2π in Figure 7h). With 40,000 signal photons detected, CHIDO experimentally achieves a lateral localization precision of $\sigma_{xy} = 13$ nm, an axial localization precision of $\sigma_z = 50$ nm, and a precision for measuring the wobble angle $\sigma_\Omega = 0.9$ for molecules attached to F-actin filaments whose tilt angles from the fiber are within 20°.

Choosing the appropriate technique for SMOLM

With a myriad of techniques developed in recent years, choosing an SMOLM design can be daunting. Recent studies adapt classical and quantum estimation theory to find optimal imaging systems for both SMLM (Tsang, 2015; Tsang et al., 2016; Lupo and Pirandola, 2016; Rehacek et al., 2017; Ang et al., 2017; Backlund et al., 2018; Tsang, 2019; Prasad and Yu, 2019) and SMOLM (Zhang and Lew, 2019, 2020, 2021a; Beckwith and Yang, 2021). For example, in the absence of background photons, one must minimize the phase variation in the detected optical field in order to measure the molecular orientation of rotationally fixed molecules as precisely as possible (Zhang and Lew, 2020). With these performance limits,

Table 2. Applications, benefits, and limitations of techniques for SMOLM

Target	Technique	Measurement application	Benefits	Limitations
Absorption dipole orientation	Excitation modulation (Backer et al., 2016; Thorsen et al., 2022)	2D or 3D orientation depending on the excitation strategy	Easier to design the excitation strategy to achieve excellent measurement performance	SM must be stable for multiple frames, needs precise control and calibration of excitation polarization especially in 3D
Mixture of absorption and emission dipole orientation	Polarized excitation and detection (Backer et al., 2019; Beausang et al., 2013)	2D position and 3D orientation	Computationally cheap, excellent measurement performance	SM must be stable for multiple frames, may exhibit bias if there exists depolarization
Emission dipole orientation	Fluorescence anisotropy and linear dichroism (Gradinaru et al., 2010; Harms et al., 1999; Zondervan et al., 2007)	Depolarization and rotational dynamics	Easy to implement	Measurement degeneracy, implicitly measures orientation
Emission dipole orientation	Polarization-sensing camera (Bruggeman et al., 2024)	2D position and 3D orientation	Easy to implement	Measurement degeneracy, lower SBR
Emission dipole orientation	Standard (defocused) (Böhmer and Enderlein, 2003; Mortensen et al., 2010), *x*- and *y*-polarized (Ding et al., 2020), 4polar(ized) (Mehta et al., 2016; Rimoli et al., 2022) DSFs	2D position and 3D orientation	Easy to implement, best detectability	Measurement degeneracy for some rotational dynamics
Emission dipole orientation	Double-helix (Backlund et al., 2012), bisected (Backer et al., 2014), quadrated (Backer et al., 2013), tri-spot (Zhang et al., 2018), duo-spot (Lu et al., 2020) DSFs	3D position and 3D orientation	Robust against aberration	Lower SBR, worse detectability and estimation performance
Emission dipole orientation	pixOL (Wu et al., 2022a), arrowhead (Jouchet et al., 2023), CHIDO (Curcio et al., 2020), vortex (Ding and Lew, 2021; Hulleman et al., 2021) DSFs	3D position and 3D orientation	Excellent detection and estimation performance	Not robust against aberrations
Emission dipole orientation	radially and azimuthally polarized DSF (Zhang et al., 2022)	2D position and 3D orientation	Excellent estimation performance, comparable detectability to the standard DSF	Not robust against aberrations
Emission dipole orientation	raMVR microscope (Zhang et al., 2023)	3D position and 3D orientation	Excellent estimation performance, robust against aberration	Complex to implement

https://doi.org/10.1017/S0033583524000167 Published online by Cambridge University Press

one can compare existing methods and evaluate how efficient a technique is at extracting maximum information from a fixed number of signal photons.

Here, we recommend choosing specific criteria based upon the target sample and measurement task. Various advantages and limitations of each approach are summarized in Table 2. In absorption-based techniques, the choice of excitation and detection strategies depends on the expected orientation and rotational dynamics of the target molecules. When most molecules align perpendicularly to the optical axis, using a standard epifluorescence excitation beam traveling along the optical axis of the objective lens with multiple in-plane polarizations is adequate for studying orientational characteristics; see, for example, (Backer et al., 2016). In contrast, when the molecular orientation exhibits a prominent axial component, it becomes necessary to either integrate emission polarization separation or implement 3D polarization modulation through tilted illumination (Thorsen et al., 2022).

For emission-based methods, we follow a recent work (Zhang and Lew, 2021b) to compare some of the aforementioned DSFs using Fisher information. From estimation theory, the best-possible standard deviation of any unbiased estimator is given by the square root of the Cramér-Rao lower bound (CRB), which is the inverse of the Fisher information matrix (Chao et al., 2016). Critically, DSFs whose spatial intensity distribution $\boldsymbol{I}$ changes more strongly with orientation exhibit superior sensitivity for measuring SM orientation. DSFs with more compact footprints, e.g., *xy*Pol, raPol, vortex DSFs, pixOL, and CHIDO, generally exhibit superior measurement precision compared to DSFs that are spread over a larger area, e.g., the DH DSF and multi-spot DSFs. Intuitively, they also are easier to detect above noise and therefore are more suitable in SM experiments whose photon budgets are limited. As shown in Figure 9a-d, raPol exhibits the highest overall position-orientation precision in thin samples for SMs at the coverslip-sample interface when the sample is defocused by approximately 200 nm. Other compact DSFs also perform well, similarly outperforming larger DSFs including the MVR microscope. However, a key disadvantage is that the subtle features of the DSFs must be measured with high sensitivity to obtain precise and accurate estimates of SM orientations and positions. Therefore, performance may degrade due to optical aberrations or miscalibration of the system. For example, CHIDO performs 5–6 times worse in experiments compared to the CRB (Curcio et al., 2020; Hulleman et al., 2021). Moreover, performance degradation may be worse when imaging deeply within biological tissues. In contrast, larger DSFs that encode SM orientations in the relative brightness of their spots and SM (axial) position in the positions of the spots are more robust to optical aberrations; precise shape-fitting is not as critical. For example, the MVR microscope exhibits both excellent measurement precision and robustness against aberrations. Further, it exhibits better precision compared to compact DSFs in thick samples over a depth range of 1.5 microns (Figure 9e–h). However, it requires careful alignment of a complex optical system.

Image analysis methods

Accurately and precisely estimating the position and orientation of molecules is crucial for SMOLM; a selection of publicly available software is summarized in Table 3. Many SMOLM algorithms separate the detection and estimation tasks; they first detect and localize SMs and then subsequently estimate their orientations (Figure 10a). For example, to detect smaller DSFs such as pixOL (Wu et al., 2022a), one might use the images of an in-focus emitter or Gaussian DSF for detection and localization. Orientation estimation and (3D) position refinement can be achieved using pattern matching (Patra et al., 2004; Aguet et al., 2009) or maximum likelihood estimation (MLE) (Hulleman et al., 2021). In contrast, 2D and/or 3D localization of the double-helix DSF and multi-spot DSFs involve localizing the spots, either by fitting Gaussian spots (Backlund et al., 2012; Backer et al., 2014) or employing other algorithms like ThunderSTORM (Ovesný et al., 2014; Zhang et al., 2018). The orientation can be calculated by using the spot brightness ratio or directly estimated using an MLE.

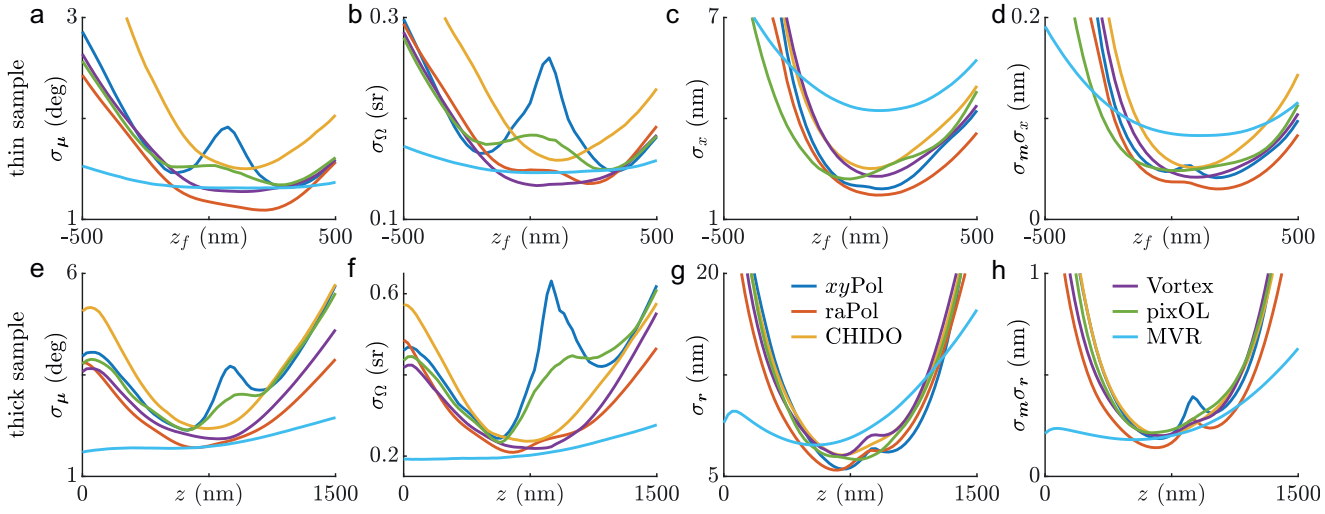

Figure 9. Best-possible precisions, given by the square root of the Cramér-Rao lower bound, of measuring SM position and orientation in (a–d) thin and (e–h) thick samples using various SMOLM techniques. For thin samples, we report precisions of (a) the average orientation $\boldsymbol{\mu}$, (b) wobble angle Ω, (c) 2D position x, and (d) combined precision for orientational second moments $\boldsymbol{m}$ and 2D position x as a function of nominal focal plane position z_f. All SMs are positioned at $z = 0$ nm (at the glass-media interface). For thick samples, we report precisions of (e) average orientation $\boldsymbol{\mu}$, (f) wobble angle Ω, (g) 3D position $\boldsymbol{r}$, and (h) combined precision for orientational second moments $\boldsymbol{m}$ and 3D position $\boldsymbol{r}$ as a function of molecular position z. The nominal focal plane is set at $z_f = 1200$ nm. For all simulations, we assume that the sample has a refractive index $n_2 = 1.33$ (equal to that of water) and that 5000 signal photons and 40 background photons per pixel total across all channels are collected. See (Zhang and Lew, 2021b) for details on how each quantity is defined and calculated.

https://doi.org/10.1017/S0033583524000167 Published online by Cambridge University Press

Table 3. Publicly available image analysis software for SMOLM

Name (reference)	Measurement application	Analysis method	Comments and repository link
RoSE-O (Mazidi et al., 2019)	2D position and 3D orientation	Sparsity-promoting regularized maximum likelihood detection and estimation	Able to perform full DSF fitting using user-supplied phase mask: https://github.com/Lew-Lab/RoSE-O. Polarization camera version also available: https://github.com/Lew-Lab/RoSE-O_POLCAM
Vecfitcpu_vortex (Hulleman et al., 2021)	3D position and 3D orientation	Maximum likelihood estimation	Software for vortex point spread function. https://github.com/imphys/vecfitcpu_vortex
4polarSTORM (Rimoli et al., 2022)	2D position and 3D orientation	Generalized likelihood ratio test (SM detection), maximum likelihood estimation	Software for 4polar-STORM. https://gitlab.fresnel.fr/mosaic/4polarSTORM
RoSEO3D (Wu et al., 2022a)	3D position and 3D orientation	Sparsity-promoting regularized maximum likelihood estimation	Able to perform full DSF fitting using user-supplied phase mask. https://github.com/Lew-Lab/RoSEO3D
Deep-SMOLM (Wu et al., 2022b)	2D position and 3D orientation	Convolutional neural network (CNN)	Initially demonstrated using the pixOL DSF. Example CNN and protocol and code for training CNN available. https://github.com/Lew-Lab/Deep-SMOLM
POLCAM (Bruggeman et al., 2024)	2D position and 3D orientation	Centroid localization, least-squares fitting	Much faster than full DSF fitting. Both SMOLM and diffraction-limited analysis functionalities are available. https://github.com/ezrabru/POLCAM-SR; https://github.com/ezrabru/POLCAM-Live; https://github.com/ezrabru/napari-polcam

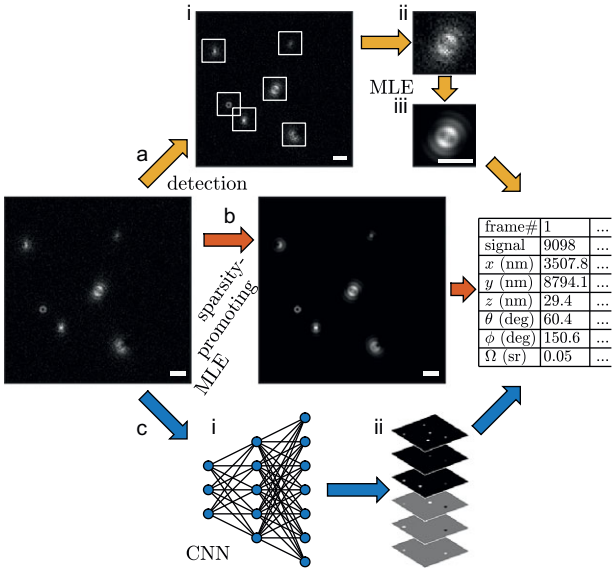

Figure 10. Workflow of detection and estimation algorithms in SMOLM. (a) A raw fluorescence image can be processed using (i) an SM detection algorithm. (ii) The detected SM images can be fitted to the forward imaging model using an MLE; a reconstruction of the raw image using the fit parameters is shown in (iii). (b) The image can also be fitted to the forward imaging model using a sparsity-promoting MLE (reconstruction shown in (b)), or (c) through a (i) convolutional neural network that generates an (ii) upsampled stack representing the position and orientation of SMs. The final output of these algorithms is a list of SM positions and orientations.

Here, we show MLE for estimating the second-order orientational moments $\boldsymbol{m}$. Other orientational parameters, such as the Stokes parameters, can be estimated similarly as long as a forward model is written that explicitly models both signal and noise within the detected images. We assume that the number of detected photons at pixel i follows a Poisson distribution, i.e., $\hat{I}_i \sim \text{Poisson}(I_i + b_i)$, where I_i is given by Eq. (45) and b_i represents the expected background. Therefore, the estimated brightness and the second-order moment vector are estimated by minimizing the Poisson negative log-likelihood (NLL), i.e.,

$$(\hat{s}, \hat{\boldsymbol{m}}) = \underset{s,\boldsymbol{m}}{\text{argmin}} \left[\sum_i \hat{I}_i \log \frac{I_i(s, \boldsymbol{B}, \boldsymbol{m}) + b_i}{b_i} - I_i \right]. \tag{49}$$

This equation can be further refined using a first-order approximation by including the gradient of $\boldsymbol{B}$ with respect to the molecule's 3D position for robust, computationally efficient subpixel-scale localization (Mazidi et al., 2019). The second moments $\hat{\boldsymbol{m}}$ can be mapped to the first-order transition dipole moments $\hat{\boldsymbol{\mu}}$ and wobble $\hat{\Omega}$ using a Fisher information (FI)-weighted, mean square-error cost function, i.e.,

$$(\hat{\boldsymbol{\mu}}, \hat{\Omega}) = \underset{\boldsymbol{\mu},\Omega}{\text{argmin}} \left\{ [\boldsymbol{m}'(\boldsymbol{\mu}, \Omega) - \hat{\boldsymbol{m}}]^{\top} \mathbf{FI} [\boldsymbol{m}'(\boldsymbol{\mu}, \Omega) - \hat{\boldsymbol{m}}] \right\}, \tag{50}$$

where $\boldsymbol{m}'$ is given by Eq. (37).

A significant drawback of separating the detection and estimation algorithms is the difficulty in handling high molecular density, thus restricting acquisition speed. An alternative strategy is to leverage the inherent sparsity of SM blinking in SMOLM experiments through a regularized MLE (Figure 10b) and solve the molecular detection and position and orientation estimation tasks simultaneously. Instead of minimizing the Poisson NLL, a sparsity-promoting regularizer, e.g., the $\ell 2$ norm of intensity-weighted second moments $\hat{\boldsymbol{m}}$ associated with each spatial grid point, is added to the cost function. Mazidi et al. demonstrated that such an algorithm performs closely to the theoretical bound given by the CRB even in highly overlapping areas (Mazidi et al., 2019). However, one limitation, especially for 3D SMOLM, is that iterative optimization algorithms tend to be computationally expensive and slow (Bruggeman et al., 2024).

Recently, deep learning, particularly convolutional neural networks (CNNs), has emerged as a powerful tool for SM image analysis due to its superior pattern recognition capabilities. Inspired by recent advancements in CNN-based 3D localization algorithms (Möckl et al., 2020; Nehme et al., 2020; Speiser et al., 2021), Wu et al.

https://doi.org/10.1017/S0033583524000167 Published online by Cambridge University Press

introduced an approach named Deep-SMOLM to detect SMs and simultaneously estimate their 2D positions and 3D orientations (Wu et al., 2022b) (Figure 10c). Two polarized images are input to the NN, and six upsampled images are produced, each representing the 2D spatial distribution of one of the six second-order orientational moments. A post-processing step converts these images into a list of 2D positions and 3D orientations. Using both simulated and experimentally acquired images with highly overlapping pixOL DSFs, the NN demonstrates measurement precision close to the theoretical limit (3.8° orientation, 0.32 sr wobble angle, and 8.5 nm lateral position using 1000 detected photons) and a tenfold improvement in speed over iterative approaches. The aforementioned Arrowhead DSF also makes use of an NN for position and orientation estimation (Jouchet et al., 2023). First, SMs within the field of view are coarsely located using the standard DSF (e.g., by turning off the SLM), and then centered and cropped ROIs containing the Arrowhead DSF are fed to the analysis NN to produce 3D position and 3D orientation estimates. The NN was able to analyze ~150,000 DSF images at a rate of 4 ms per molecule. Clearly, the use of NNs for SMOLM image analysis holds tremendous promise for accelerating precise 6D measurements of SMs.

Conclusion and outlook

In this review, we have explored the latest advancements in SMOLM, highlighting its expanding role across various research areas. Our discussion spans a range of innovative labeling techniques and advanced imaging methods that offer unparalleled insights into molecular orientations and dynamics. Recent work highlights the crucial roles of fluorescent probes for visualizing the complex organization and dynamics of actin filaments, DNA structures, amyloid aggregates, and cellular membranes, among others. Additionally, we have reviewed various imaging techniques that underscore both the potential and the challenges of SMOLM. These methods aim to optimize the measurement of molecular orientations from multiple perspectives, including the fundamental physics of light-matter interactions as well as principles of estimation theory. Further, the incorporation of advanced computational tools improves the accuracy and precision of these measurements. Overall, the insights presented in this review underscore how SMOLM advances our understanding of biological and biochemical processes at the nanoscale.

As we envision the future of SMOLM, several developments are key to further expanding its capabilities and adoption in biophysical studies. The development of new fluorescent probes is crucial for advancing SMOLM (Grimm et al., 2023). Future probes should aim for enhanced photostability, higher quantum yield, and improved binding specificity to target structures, while also minimizing perturbative effects. These improvements would significantly enhance the SBR in SMOLM measurements by boosting signal levels and reducing the off-structure background. Improved brightness (photons/s) is particularly critical when studying the orientational dynamics of SMs in the complex environments of biological systems. Engineering new probes that specifically bind to certain biomarkers or protein domains, react to cellular environmental changes, and change their optical properties in response to specific chemical interactions and environments will also be particularly beneficial (Kikuchi et al., 2023; Wu et al., 2023; Bhuskute et al., 2024; Erkamp et al., 2024; Zhu et al., 2024).

Continuous innovation in imaging systems is essential for overcoming the limitations of existing methods and achieving accurate, precise, and robust measurements. Measurement precision could be further enhanced by using adaptive hardware, where the imaging system is iteratively updated to progressively measure the orientation of a single molecule more precisely, as is done for molecular positions in MINFLUX (Balzarotti et al., 2017; Cnossen et al., 2020; Gwosch et al., 2020; Weber et al., 2023; Sahl et al., 2024). Recent developments in single-photon avalanche diode (SPAD) array detectors (Bucci et al., 2024) have the potential to provide precise photon arrival timing as well as location information for SMOLM, thereby enabling SMOLM to probe faster biochemical processes including protein folding and conformational dynamics. Existing emission-based methods (engineered DSFs) could be combined with selective illumination techniques like light-sheet illumination (Gustavsson et al., 2018; Nelson et al., 2024) to improve the SBR. Further, measuring higher-order orientational moments, i.e., measuring absorption and emission dipole moments simultaneously using both excitation and emission modulation, could enable more detailed studies of rotational dynamics with improved angular resolution (Chen et al., 2024b). In these ways, each precious fluorescence photon can be utilized more efficiently for higher precision measurements.

Advanced computational imaging techniques will also play a significant role in the future of SMOLM. The integration of modern computer vision methodologies, such as neural fields (Park et al., 2019; Mildenhall et al., 2022; Zhou et al., 2023; Zhang et al., 2024) or diffusion models (Waibel et al., 2023; Hui et al., 2024), could potentially improve estimation performance, allowing for the extraction of more detailed information from larger and more complex datasets. Especially when engineered DSFs and estimation algorithms are optimized jointly, these computational advances could potentially handle images with higher molecular density, thereby improving imaging speed and overall data throughput.

With numerous opportunities for technological innovation, we expect SMOLM to have significant contributions to elucidating the nanoscale organization and dynamics of biological and chemical systems in the near future. Higher precision measurements of both 3D position and 3D orientation have a unique power to reveal new insights, and we eagerly anticipate SMOLM to have far-ranging applications from understanding fundamental biological processes to developing new materials and nanotechnologies.

Acknowledgements. We thank Tianben Ding and Tingting Wu for helpful discussions when preparing this manuscript.

Financial support. Research reported in this publication was supported by the National Institute of General Medical Sciences of the National Institutes of Health under Award Number R35GM124858 to M.D.L.

Competing interest. The authors declare none.

References

Adamczyk AK, Huijben TAPM, Sison M, Di Luca A, Chiarelli G, Vanni S, Brasselet S, Mortensen KI, Stefani FD, Pilo-Pais M and Acuna GP (2022) DNA self-assembly of single molecules with deterministic position and orientation. *ACS Nano* **16** (10), 16924–16931. https://doi.org/10.1021/acsnano.2c06936

Adams C, Gross RE, Martin LA, Walkup BR, Yao GK, Llopis JY and Tsien RY (2002) New biarsenical ligands and Tetracysteine motifs for protein labeling in vitro and in vivo: Synthesis and biological applications. *Journal of the American Chemical Society* **124** (21), 6063–6076. https://doi.org/10.1021/ja017687n

Aguet F, Geissbühler S, Märki I, Lasser T and Unser M (2009) Super-resolution orientation estimation and localization of fluorescent dipoles

using 3-D steerable filters. *Optics Express* **17** (8), 6829. https://doi.org/10.1364/OE.17.006829

Aitken CE, Marshall RA and Puglisi JD (2008) An oxygen scavenging system for improvement of dye stability in single-molecule fluorescence experiments. *Biophysical Journal* **94** (5), 1826–1835. https://doi.org/10.1529/biophysj.107.117689

Alonso MA (2023) Geometric descriptions for the polarization of nonparaxial light: A tutorial. *Advances in Optics and Photonics* **15** (1), 176. https://doi.org/10.1364/AOP.475491

Ang SZ, Nair R and Tsang M (2017) Quantum limit for two-dimensional resolution of two incoherent optical point sources. *Physical Review A* **95** (6), 063847. https://doi.org/10.1103/PhysRevA.95.063847

Aquino D, Schönle A, Geisler C, Middendorff CV, Wurm CA, Okamura Y, Lang T, Hell SW and Egner A (2011) Two-color nanoscopy of three-dimensional volumes by 4Pi detection of stochastically switched fluorophores. *Nature Methods* **8** (4), 353–359. https://doi.org/10.1038/nmeth.1583

Asenjo AB, Krohn N and Sosa H (2003) Configuration of the two kinesin motor domains during ATP hydrolysis. *Nature Structural \& Molecular Biology* **10** (10), 836–842. https://doi.org/10.1038/nsb984

Axelrod D (2012) Fluorescence excitation and imaging of single molecules near dielectric-coated and bare surfaces: A theoretical study. *Journal of Microscopy* **247** (2), 147–160. https://doi.org/10.1111/j.1365-2818.2012.03625.x

Backer AS, Backlund MP, Lew MD and Moerner WE (2013) Single-molecule orientation measurements with a quadrated pupil. *Optics Letters* **38** (9), 1521. https://doi.org/10.1364/OL.38.001521

Backer AS, Backlund MP, von Diezmann AR, Sahl SJ and Moerner WE (2014) A bisected pupil for studying single-molecule orientational dynamics and its application to three-dimensional super-resolution microscopy. *Applied Physics Letters* **104** (19), 193701. https://doi.org/10.1063/1.4876440

Backer AS, Biebricher AS, King GA, Wuite GJL, Heller I and Peterman EJG (2019) Single-molecule polarization microscopy of DNA intercalators sheds light on the structure of S-DNA. *Science Advances* **5** (3), eaav1083. https://doi.org/10.1126/sciadv.aav1083

Backer AS, Lee MY and Moerner WE (2016) Enhanced DNA imaging using super-resolution microscopy and simultaneous single-molecule orientation measurements. *Optica* **3** (6), 659. https://doi.org/10.1364/OPTICA.3.000659

Backer AS and Moerner WE (2014) Extending single-molecule microscopy using optical Fourier processing. *The Journal of Physical Chemistry B* **118** (28), 8313–8329. https://doi.org/10.1021/jp501778z

Backer AS and Moerner WE (2015) Determining the rotational mobility of a single molecule from a single image: A numerical study. *Optics Express* **23** (4), 4255. https://doi.org/10.1364/OE.23.004255

Backlund MP, Arbabi A, Petrov PN, Arbabi E, Saurabh S, Faraon A and Moerner WE (2016) Removing orientation-induced localization biases in single-molecule microscopy using a broadband metasurface mask. *Nature Photonics* **10** (7), 459–462. https://doi.org/10.1038/nphoton.2016.93

Backlund MP, Kehayias P and Walsworth RL (2017) Diamond-based magnetic imaging with Fourier optical processing. *Physical Review Applied* **8** (5), 054003. https://doi.org/10.1103/PhysRevApplied.8.054003

Backlund MP, Lew MD, Backer AS, Sahl SJ, Grover G, Agrawal A, Piestun R and Moerner WE (2012) Simultaneous, accurate measurement of the 3D position and orientation of single molecules. *Proceedings of the National Academy of Sciences* **109** (47), 19087–19092. https://doi.org/10.1073/pnas.1216687109

Backlund MP, Lew MD, Backer AS, Sahl SJ and Moerner WE (2014) The role of molecular dipole orientation in single-molecule fluorescence microscopy and implications for super-resolution imaging. *ChemPhysChem* **15** (4), 587–599. https://doi.org/10.1002/cphc.201300880

Backlund MP, Shechtman Y and Walsworth RL (2018) Fundamental precision bounds for three-dimensional optical localization microscopy with Poisson statistics. *Physical Review Letters* **121** (2), 023904. https://doi.org/10.1103/PhysRevLett.121.023904

Balzarotti F, Eilers Y, Gwosch KC, Gynnå AH, Westphal V, Stefani FD, Elf J and Hell SW (2017) Nanometer resolution imaging and tracking of fluorescent molecules with minimal photon fluxes. *Science* **355** (6325), 606–612. https://doi.org/10.1126/science.aak9913

Beane G, Boldt K, Kirkwood N and Mulvaney P (2014) Energy transfer between quantum dots and conjugated dye molecules. *The Journal of Physical Chemistry C* **118** (31), 18079–18086. https://doi.org/10.1021/jp502033d

Beausang JF, Shroder DY, Nelson PC and Goldman YE (2013) Tilting and wobble of myosin V by high-speed single-molecule polarized fluorescence microscopy. *Biophysical Journal* **104** (6), 1263–1273. https://doi.org/10.1016/j.bpj.2013.01.057

Beckwith JS and Yang H (2021) Sub-millisecond translational and Orientational dynamics of a freely moving single Nanoprobe. *The Journal of Physical Chemistry B* **125** (49), 13436–13443. https://doi.org/10.1021/acs.jpcb.1c08917

Betzig E and Chichester RJ (1993) Single molecules observed by near-field scanning optical microscopy. *Science* **262** (5138), 1422–1425. https://doi.org/10.1126/science.262.5138.1422

Betzig E, Patterson GH, Sougrat R, Lindwasser OW, Olenych S, Bonifacino JS, Davidson MW, Lippincott-Schwartz J and Hess HF (2006) Imaging intracellular fluorescent proteins at nanometer resolution. *Science* **313** (5793), 1642–1645. https://doi.org/10.1126/science.1127344

Bhuskute KR, Kikuchi K, Luo Z and Kaur A (2024) Visualizing amyloid assembly at the Nanoscale: Insights from super-resolution imaging. *Analysis & Sensing* **4** (4), e202400001. https://doi.org/10.1002/anse.202400001

Biebricher AS, Heller I, Roijmans RFH, Hoekstra TP, Peterman EJG and Wuite GJL (2015) The impact of DNA intercalators on DNA and DNA-processing enzymes elucidated through force-dependent binding kinetics. *Nature Communications* **6** (1), 7304. https://doi.org/10.1038/ncomms8304

Blanchard A, Combs JD, Brockman JM, Kellner AV, Glazier R, Su H, Bender RL, Bazrafshan AS, Chen W, Quach ME, Li R, Mattheyses AL and Salaita K (2021) Turn-key mapping of cell receptor force orientation and magnitude using a commercial structured illumination microscope. *Nature Communications* **12** (1), 4693. https://doi.org/10.1038/s41467-021-24602-x

Bloksma F and Zijlstra P (2021) Imaging and localization of single emitters near Plasmonic particles of different size, shape, and material. *The Journal of Physical Chemistry C* **125** (40), 22084–22092. https://doi.org/10.1021/acs.jpcc.1c06665

Böhmer M and Enderlein J (2003) Orientation imaging of single molecules by wide-field epifluorescence microscopy. *Journal of the Optical Society of America B* **20** (3), 554. https://doi.org/10.1364/JOSAB.20.000554

Bongiovanni MN, Godet J, Horrocks MH, Tosatto L, Carr AR, Wirthensohn DC, Ranasinghe RT, Lee J-E, Ponjavic A, Fritz JV, Dobson CM, Klenerman D and Lee SF (2016) Multi-dimensional super-resolution imaging enables surface hydrophobicity mapping. *Nature Communications* **7** (1), 13544. https://doi.org/10.1038/ncomms13544

Brasselet S and Alonso MA (2023) Polarization microscopy: From ensemble structural imaging to single-molecule 3D orientation and localization microscopy. *Optica* **10** (11), 1486. https://doi.org/10.1364/OPTICA.502119

Brenner B, Sun C, Raymo FM and Zhang HF (2023) Spectroscopic single-molecule localization microscopy: Applications and prospective. *Nano Convergence* **10** (1), 14. https://doi.org/10.1186/s40580-023-00363-9

Brockman JM, Blanchard AT, Pui-Yan V, Derricotte WD, Zhang Y, Fay ME, Lam WA, Evangelista FA, Mattheyses AL and Salaita K (2018) Mapping the 3D orientation of piconewton integrin traction forces. *Nature Methods* **15**(2), 115–118. https://doi.org/10.1038/nmeth.4536.

Bruggeman E, Zhang O, Needham L-M, Körbel M, Daly S, Cheetham M, Peters R, Wu T, Klymchenko AS, Davis SJ, Paluch EK, Klenerman D, Lew MD, O'Holleran K and Lee SF (2024) POLCAM: Instant molecular orientation microscopy for the life sciences. *Nature Methods* **21** (10), 1873–1883. https://doi.org/10.1038/s41592-024-02382-8

Bucci A, Tortarolo G, Held MO, Bega L, Perego E, Castagnetti F, Bozzoni I, Slenders E and Vicidomini G (2024) 4D single-particle tracking with asynchronous read-out single-photon avalanche diode array detector. *Nature Communications* **15** (1), 6188. https://doi.org/10.1038/s41467-024-50512-9

Budiarta M, Streit M and Beliu G (2024) Site-specific protein labeling strategies for super-resolution microscopy. *Current Opinion in Chemical Biology* **80**, 102445. https://doi.org/10.1016/j.cbpa.2024.102445

Bustamante CJ, Chemla YR, Liu S and Wang MD (2021) Optical tweezers in single-molecule biophysics. *Nature Reviews Methods Primers* **1** (1), 25. https://doi.org/10.1038/s43586-021-00021-6

Carlsson C, Larsson A, Jonsson M, Albinsson B and Norden B (1994) Optical and photophysical properties of the oxazole yellow DNA probes YO and YOYO. *The Journal of Physical Chemistry* **98** (40), 10313–10321. https://doi.org/10.1021/j100091a055

https://doi.org/10.1017/S0033583524000167 Published online by Cambridge University Press

Cathey WT, **Frieden BR**, **Rhodes WT and Rushforth CK** (1984) Image gathering and processing for enhanced resolution. *Journal of the Optical Society of America A* **1** (3), 241. https://doi.org/10.1364/JOSAA.1.000241

Cervantes-Salguero K, **Biaggne A**, **Youngsman JM**, **Ward BM**, **Kim YC**, **Li L**, **Hall JA**, **Knowlton WB**, **Graugnard E and Kuang W** (2022) Strategies for controlling the spatial orientation of single molecules tethered on DNA origami templates physisorbed on glass substrates: Intercalation and stretching. *International Journal of Molecular Sciences* **23** (14), 7690. https://doi.org/10.3390/ijms23147690

Cervantes-Salguero K, **Kadrmas M**, **Ward BM**, **Lysne D**, **Wolf A**, **Piantanida L**, **Pascual G and Knowlton WB** (2024) Minimizing structural heterogeneity in DNA self-assembled dye Templating via DNA origami-tuned conformations. *Langmuir* **40** (19), 10195–10207. https://doi.org/10.1021/acs.langmuir.4c00470

Chandler T, **Shroff H**, **Oldenbourg R and La Rivière P** (2019a) Spatio-angular fluorescence microscopy I basic theory. *Journal of the Optical Society of America A* **36** (8), 1334. https://doi.org/10.1364/JOSAA.36.001334

Chandler T, **Shroff H**, **Oldenbourg R and La Rivière P** (2020) Spatio-angular fluorescence microscopy III constrained angular diffusion, polarized excitation, and high-NA imaging. *Journal of the Optical Society of America A* **37** (9), 1465. https://doi.org/10.1364/JOSAA.389217

Chandler T, **Shroff H**, **Oldenbourg R and Rivière PL** (2019b) Spatio-angular fluorescence microscopy II paraxial 4f imaging. *Journal of the Optical Society of America A* **36** (8), 1346. https://doi.org/10.1364/JOSAA.36.001346

Chao J, **Sally Ward E and Ober RJ** (2016) Fisher information theory for parameter estimation in single molecule microscopy: Tutorial. *Journal of the Optical Society of America A* **33** (7), B36. https://doi.org/10.1364/JOSAA.33.000B36

Chen T, **Karedla N and Enderlein J** (2024a) Measuring sub-nanometer undulations at microsecond temporal resolution with metal- and graphene-induced energy transfer spectroscopy. *Nature Communications* **15** (1), 1789. https://doi.org/10.1038/s41467-024-45822-x

Chen X, **Zaro JL and Shen W-C** (2013) Fusion protein linkers: Property, design and functionality. *Advanced Drug Delivery Reviews* **65** (10), 1357–1369. https://doi.org/10.1016/j.addr.2012.09.039

Chen Y, **Qiu Y and Lew MD** (2024b) Resolving the Orientations of and Separation between an Overlapping Pair of Dipole Emitters. (Version 1). arXiv. https://doi.org/10.48550/ARXIV.2406.04469.

Cho Y, **Park SH**, **Huh J-H**, **Gopinath A and Lee S** (2023) DNA as grabbers and steerers of quantum emitters. *Nano* **12** (3), 399–412. https://doi.org/10.1515/nanoph-2022-0602

Cnossen J, **Hinsdale T**, **Thorsen RØ**, **Siemons M**, **Schueder F**, **Jungmann R**, **Smith CS**, **Rieger B and Stallinga S** (2020) Localization microscopy at doubled precision with patterned illumination. *Nature Methods* **17** (1), 59–63. https://doi.org/10.1038/s41592-019-0657-7

Cordes T, **Maiser A**, **Steinhauer C**, **Schermelleh L and Tinnefeld P** (2011) Mechanisms and advancement of antifading agents for fluorescence microscopy and single-molecule spectroscopy. *Physical Chemistry Chemical Physics* **13** (14), 6699. https://doi.org/10.1039/c0cp01919d

Corrie JET, **Brandmeier BD**, **Ferguson RE**, **Trentham DR**, **Kendrick-Jones J**, **Hopkins SC**, **van der HUA**, **Goldman YE**, **Sabido-David C**, **Dale RE**, **Criddle S and Irving M** (1999) Dynamic measurement of myosin light-chain-domain tilt and twist in muscle contraction. *Nature* **400** (6743), 425–430. https://doi.org/10.1038/22704

Corrie JET, **Craik JS and Munasinghe VRN** (1998) A Homobifunctional Rhodamine for labeling proteins with defined orientations of a Fluorophore. *Bioconjugate Chemistry* **9** (2), 160–167. https://doi.org/10.1021/bc970174e

Curcio V, **Alemán-Castañeda LA**, **Brown TG**, **Brasselet S and Alonso MA** (2020) Birefringent Fourier filtering for single molecule coordinate and height super-resolution imaging with dithering and orientation. *Nature Communications* **11** (1), 5307. https://doi.org/10.1038/s41467-020-19064-6

Cyphersmith A, **Maksov A**, **Hassey-Paradise R**, **McCarthy KD and Barnes MD** (2011) Defocused emission patterns from chiral Fluorophores: Application to chiral Axis orientation determination. *The Journal of Physical Chemistry Letters* **2** (6), 661–665. https://doi.org/10.1021/jz2001024

Danzer KM, **Haasen D**, **Karow AR**, **Moussaud S**, **Habeck M**, **Giese A**, **Kretzschmar H**, **Hengerer B and Kostka M** (2007) Different species of -Synuclein oligomers induce calcium influx and seeding. *Journal of Neuroscience* **27** (34), 9220–9232. https://doi.org/10.1523/JNEUROSCI.2617-07.2007

Dave R, **Terry DS**, **Munro JB and Blanchard SC** (2009) Mitigating unwanted Photophysical processes for improved single-molecule fluorescence imaging. *Biophysical Journal* **96** (6), 2371–2381. https://doi.org/10.1016/j.bpj.2008.11.061

Dedecker P, **Muls B**, **Deres A**, **Uji-i H**, **Hotta J**, **Sliwa M**, **Soumillion J**, **Müllen K**, **Enderlein J and Hofkens J** (2009) Defocused wide-field imaging unravels structural and temporal heterogeneity in complex systems. *Advanced Materials* **21** (10–11), 1079–1090. https://doi.org/10.1002/adma.200801873

Dickson RM, **Norris DJ and Moerner WE** (1998) Simultaneous imaging of individual molecules aligned both parallel and perpendicular to the optic axis. *Physical Review Letters* **81** (24), 5322–5325. https://doi.org/10.1103/PhysRevLett.81.5322

Ding T and Lew MD (2021) Single-molecule localization microscopy of 3D orientation and anisotropic wobble using a polarized vortex point spread function. *The Journal of Physical Chemistry B* **125** (46), 12718–12729. https://doi.org/10.1021/acs.jpcb.1c08073

Ding T, **Wu T**, **Mazidi H**, **Zhang O and Lew MD** (2020) Single-molecule orientation localization microscopy for resolving structural heterogeneities between amyloid fibrils. *Optica* **7** (6), 602. https://doi.org/10.1364/OPTICA.388157

Doose S, **Neuweiler H**, **Barsch H and Sauer M** (2007) Probing polyproline structure and dynamics by photoinduced electron transfer provides evidence for deviations from a regular polyproline type II helix. *Proceedings of the National Academy of Sciences* **104** (44), 17400–17405. https://doi.org/10.1073/pnas.0705605104

Dowski ER and Cathey WT (1995) Extended depth of field through wavefront coding. *Applied Optics* **34** (11), 1859. https://doi.org/10.1364/AO.34.001859

Engelhardt J, **Keller J**, **Hoyer P**, **Reuss M**, **Staudt T and Hell SW** (2011) Molecular orientation affects localization accuracy in superresolution far-field fluorescence microscopy. *Nano Letters* **11** (1), 209–213. https://doi.org/10.1021/nl103472b

Erkamp NA, **Farag M**, **Qiu Y**, **Quan D**, **Sneideris T**, **Wu T**, **Welsh TJ**, **Ausserwöger H**, **Krug TJ**, **Weitz DA**, **Lew MD**, **Knowles TPJ and Pappu RV** (2024) Differential interactions determine anisotropies at interfaces of RNA-based biomolecular condensates *bioRxiv* 2024.08.19.608662. https://doi.org/10.1101/2024.08.19.608662

Fischer M and Georges J (1996) Fluorescence quantum yield of rhodamine 6G in ethanol as a function of concentration using thermal lens spectrometry. *Chemical Physics Letters* **260** (1–2), 115–118. https://doi.org/10.1016/0009-2614(96)00838-X

Flors C, **Ravarani CNJ and David TFD** (2009) Super-resolution imaging of DNA Labelled with intercalating dyes. *ChemPhysChem* **10** (13), 2201–2204. https://doi.org/10.1002/cphc.200900384

Forkey JN, **Quinlan ME**, **Alexander Shaw M**, **Corrie JET and Goldman YE** (2003) Three-dimensional structural dynamics of myosin V by single-molecule fluorescence polarization. *Nature* **422** (6930), 399–404. https://doi.org/10.1038/nature01529

Fourkas JT (2001) Rapid determination of the three-dimensional orientation of single molecules. *Optics Letters* **26** (4), 211. https://doi.org/10.1364/OL.26.000211

Frahm L and Keller J (2016) Polarization modulation adds little additional information to super-resolution fluorescence microscopy. *Nature Methods* **13** (1), 7–8. https://doi.org/10.1038/nmeth.3687

Fu S, **Shi W**, **Luo T**, **He Y**, **Zhou L**, **Yang J**, **Yang Z**, **Liu J**, **Liu X**, **Guo Z**, **Yang C**, **Liu C**, **Huang Z**, **Ries J**, **Zhang M**, **Xi P**, **Jin D and Li Y** (2023) Field-dependent deep learning enables high-throughput whole-cell 3D super-resolution imaging. *Nature Methods* **20** (3), 459–468. https://doi.org/10.1038/s41592-023-01775-5

Gahlmann A, **Ptacin JL**, **Grover G**, **Quirin S**, **von Diezmann L**, **Lee MK**, **Backlund MP**, **Shapiro L**, **Piestun R and Moerner WE** (2013) Quantitative multicolor subdiffraction imaging of bacterial protein Ultrastructures in three dimensions. *Nano Letters* **13** (3), 987–993. https://doi.org/10.1021/nl304071h

Ghosh A, **Sharma A**, **Chizhik AI**, **Isbaner S**, **Ruhlandt D**, **Tsukanov R**, **Gregor I**, **Karedla N and Enderlein J** (2019) Graphene-based metal-induced energy

https://doi.org/10.1017/S0033583524000167 Published online by Cambridge University Press

transfer for sub-nanometre optical localization. *Nature Photonics* **13** (12), 860–865. https://doi.org/10.1038/s41566-019-0510-7

Glembockyte V, Lin J and Cosa G (2016) Improving the photostability of red- and green-emissive single-molecule fluorophores via Ni^{2+} mediated excited triplet-state quenching. *The Journal of Physical Chemistry B* **120** (46), 11923–11929. https://doi.org/10.1021/acs.jpcb.6b10725

Goldwyn HJ, Smith KC, Busche JA and Masiello DJ (2018) Mislocalization in Plasmon-enhanced single-molecule fluorescence microscopy as a dynamical Young's interferometer. *ACS Photonics* **5** (8), 3141–3151. https://doi.org/10.1021/acsphotonics.8b00372

Gould TJ, Gunewardene MS, Gudheti MV, Verkhusha Y, S-R GJA and Hess ST (2008) Nanoscale imaging of molecular positions and anisotropies. *Nature Methods* **5** (12), 1027–1030. https://doi.org/10.1038/nmeth.1271

Grabenhorst L, Trofymchuk K, Steiner F, Glembockyte V and Tinnefeld P (2020) Fluorophore photostability and saturation in the hotspot of DNA origami nanoantennas. *Methods and Applications in Fluorescence* **8** (2), 024003. https://doi.org/10.1088/2050-6120/ab6ac8

Gradinaru CC, Marushchak DO, Samim M and Krull UJ (2010) Fluorescence anisotropy: From single molecules to live cells. *The Analyst* **135** (3), 452. https://doi.org/10.1039/b920242k

Gräwe A and Stein V (2021) Linker engineering in the context of synthetic protein switches and sensors. *Trends in Biotechnology* **39** (7), 731–744. https://doi.org/10.1016/j.tibtech.2020.11.007

Griffin BA, Adams SR and and Tsien RY (1998) Specific covalent labeling of recombinant protein molecules inside live cells. *Science* **281** (5374), 269–272. https://doi.org/10.1126/science.281.5374.269

Grimm JB, Tkachuk AN, Patel R, Hennigan ST, Gutu A, Dong P, Gandin V, Osowski AM, Holland KL, Liu ZJ, Brown TA and Lavis LD (2023) Optimized red-absorbing dyes for imaging and sensing. *Journal of the American Chemical Society* **145** (42), 23000–23013. https://doi.org/10.1021/jacs.3c05273

Guan M, Wang M, Zhanghao K, Zhang X, Li M, Liu W, Niu J, Yang X, Chen L, Jing Z, Zhang MQ, Jin D, Xi P and Gao J (2022) Polarization modulation with optical lock-in detection reveals universal fluorescence anisotropy of subcellular structures in live cells. *Light: Science & Applications* **11** (1), 4. https://doi.org/10.1038/s41377-021-00689-1

Gust A, Zander A, Gietl A, Holzmeister P, Schulz S, Lalkens B, Tinnefeld P and Grohmann D (2014) A starting point for fluorescence-based single-molecule measurements in biomolecular research. *Molecules* **19** (10), 15824–15865. https://doi.org/10.3390/molecules191015824

Gustavsson A-K, Petrov PN, Lee MY, Shechtman Y and Moerner WE (2018) 3D single-molecule super-resolution microscopy with a tilted light sheet. *Nature Communications* **9** (1), 123. https://doi.org/10.1038/s41467-017-02563-4

Gwosch KC, Pape JK, Balzarotti F, Hoess P, Ellenberg J, Ries J and Hell SW (2020) MINFLUX nanoscopy delivers 3D multicolor nanometer resolution in cells. *Nature Methods* **17** (2), 217–224. https://doi.org/10.1038/s41592-019-0688-0

Ha T, Enderle T, Chemla DS, Selvin PR and Weiss S (1996) Single molecule dynamics studied by polarization modulation. *Physical Review Letters* **77** (19), 3979–3982. https://doi.org/10.1103/PhysRevLett.77.3979

Ha T, Glass J, Th E, Chemla DS and Weiss S (1998) Hindered rotational diffusion and rotational jumps of single molecules. *Physical Review Letters* **80** (10), 2093–2096. https://doi.org/10.1103/PhysRevLett.80.2093

Ha T and Tinnefeld P (2012) Photophysics of fluorescent probes for single-molecule biophysics and super-resolution imaging. *Annual Review of Physical Chemistry* **63** (1), 595–617. https://doi.org/10.1146/annurev-physchem-032210-103340

Hafi N, Grunwald M, Van Den Heuvel LS, Aspelmeier T, Chen J-H, Zagrebelsky M, Schütte OM, Steinem C, Korte M, Munk A and Walla PJ (2014) Fluorescence nanoscopy by polarization modulation and polarization angle narrowing. *Nature Methods* **11** (5), 579–584. https://doi.org/10.1038/nmeth.2919

Hafi N, Grunwald M, Van Den Heuvel LS, Aspelmeier T, Steinem C, Korte M, Munk A and Walla PJ (2016) Reply to 'polarization modulation adds little additional information to super-resolution fluorescence microscopy'. *Nature Methods* **13** (1), 8–9. https://doi.org/10.1038/nmeth.3721

Halder A, Saha B, Maity P, Kumar GS, Sinha DK and Karmakar S (2018) Lipid chain saturation and the cholesterol in the phospholipid membrane affect the spectroscopic properties of lipophilic dye nile red. *Spectrochimica Acta Part A: Molecular and Biomolecular Spectroscopy* **191**, 104–110. https://doi.org/10.1016/j.saa.2017.10.002

Ham S, Yang J, Schlosser F, Würthner F and Kim D (2014) Reconstruction of the molecular structure of a Multichromophoric system using single-molecule defocused wide-field imaging. *The Journal of Physical Chemistry Letters* **5** (16), 2830–2835. https://doi.org/10.1021/jz501233d

Harms GS, Sonnleitner M, Schütz GJ, Gruber HJ and Schmidt T (1999) Single-molecule anisotropy imaging. *Biophysical Journal* **77** (5), 2864–2870. https://doi.org/10.1016/S0006-3495(99)77118-3

Hashimoto M, Yoshiki K, Kurihara M, Hashimoto N and Araki T (2015) Orientation detection of a single molecule using pupil filter with electrically controllable polarization pattern. *Optical Review* **22** (6), 875–881. https://doi.org/10.1007/s10043-015-0143-0

Hauke L, Isbaner S, Ghosh A, Guido I, Turco L, Chizhik AI, Gregor I, Karedla N, Rehfeldt F and Enderlein J (2023) Metal-induced energy transfer (MIET) for live-cell imaging with fluorescent proteins. *ACS Nano* **17** (9), 8242–8251. https://doi.org/10.1021/acsnano.2c12372

Hess ST, Girirajan TPK and Mason MD (2006) Ultra-high resolution imaging by fluorescence Photoactivation localization microscopy. *Biophysical Journal* **91** (11), 4258–4272. https://doi.org/10.1529/biophysj.106.091116

Heussman D, Kittell J, Von Hippel PH and Marcus AH (2022) Temperature-dependent local conformations and conformational distributions of cyanine dimer labeled single-stranded–double-stranded DNA junctions by 2D fluorescence spectroscopy. *The Journal of Chemical Physics* **156** (4), 045101. https://doi.org/10.1063/5.0076261

Huang F, Sirinakis G, Allgeyer ES, Schroeder LK, Duim WC, Kromann EB, Phan T, Rivera-Molina FE, Myers JR, Irnov I, Lessard M, Zhang Y, Handel MA, Jacobs-Wagner C, Lusk CP, Rothman JE, Toomre D, Booth MJ and Bewersdorf J (2016) Ultra-high resolution 3D imaging of whole cells. *Cell* **166** (4), 1028–1040. https://doi.org/10.1016/j.cell.2016.06.016

Hübner K, Joshi H, Aksimentiev A, Stefani FD, Tinnefeld P and Acuna GP (2021) Determining the in-plane orientation and binding mode of single fluorescent dyes in DNA origami structures. *ACS Nano* **15** (3), 5109–5117. https://doi.org/10.1021/acsnano.0c10259

Hui M, Wei Z, Zhu H, Xia F and Zhou Y (2024) Microdiffusion: Implicit representation-guided diffusion for 3D reconstruction from limited 2D microscopy projections. In *Proceedings of the IEEE/CVF Conference on Computer Vision and Pattern Recognition (CVPR)*, pp. 11460–11469.

Huijben TAPM, Mahajan S, Fahim M, Zijlstra P, Marie R and Mortensen KI (2024) Point-spread function deformations unlock 3D localization microscopy on spherical nanoparticles. *ACS Nano* **18** (43), 29832–29845. https://doi.org/10.1021/acsnano.4c09719

Hulleman CN, Thorsen RØ, Kim E, Dekker C, Stallinga S and Rieger B (2021) Simultaneous orientation and 3D localization microscopy with a vortex point spread function. *Nature Communications* **12** (1), 5934. https://doi.org/10.1038/s41467-021-26228-5

Iqbal A, Arslan S, Okumus B, Wilson TJ, Giraud G, Norman DG, Ha T and Lilley DMJ (2008) Orientation dependence in fluorescent energy transfer between Cy3 and Cy5 terminally attached to double-stranded nucleic acids. *Proceedings of the National Academy of Sciences* **105** (32), 11176–11181. https://doi.org/10.1073/pnas.0801707105

Jouchet P, Roy AR and Moerner WE (2023) Combining deep learning approaches and point spread function engineering for simultaneous 3D position and 3D orientation measurements of fluorescent single molecules. *Optics Communications* **542**, 129589. https://doi.org/10.1016/j.optcom.2023.129589

Jradi FM and Lavis LD (2019) Chemistry of photosensitive Fluorophores for single-molecule localization microscopy. *ACS Chemical Biology* **14** (6), 1077–1090. https://doi.org/10.1021/acschembio.9b00197

Jungmann R, Avendaño MS, Woehrstein JB, Dai M, Shih WM and Yin P (2014) Multiplexed 3D cellular super-resolution imaging with DNA-PAINT and exchange-PAINT. *Nature Methods* **11** (3), 313–318. https://doi.org/10.1038/nmeth.2835

Jungmann R, Steinhauer C, Scheible M, Kuzyk A, Tinnefeld P and Simmel FC (2010) Single-molecule kinetics and super-resolution microscopy by fluorescence imaging of transient binding on DNA origami. *Nano Letters* **10** (11), 4756–4761. https://doi.org/10.1021/nl103427w

https://doi.org/10.1017/S0033583524000167 Published online by Cambridge University Press

Kaminska I, **Vietz C**, **Cuartero-González Á**, **Tinnefeld P**, **Fernández-Domínguez AI and Acuna GP** (2018) Strong plasmonic enhancement of single molecule photostability in silver dimer optical antennas. *Nano* **7** (3), 643–649. https://doi.org/10.1515/nanoph-2017-0081

Karedla N, **Stein SC**, **Hähnel D**, **Gregor I**, **Chizhik A and Enderlein J** (2015) Simultaneous measurement of the three-dimensional orientation of excitation and emission dipoles. *Physical Review Letters* **115** (17), 173002. https://doi.org/10.1103/PhysRevLett.115.173002

Kikuchi K, **Adair LD**, **Lin J**, **New EJ and Kaur A** (2023) Photochemical mechanisms of Fluorophores employed in single-molecule localization microscopy. *Angewandte Chemie International Edition* **62** (1), e202204745. https://doi.org/10.1002/anie.202204745

Kinkhabwala A, **Yu Z**, **Fan S**, **Avlasevich Y**, **Müllen K and Moerner WE** (2009) Large single-molecule fluorescence enhancements produced by a bowtie nanoantenna. *Nature Photonics* **3** (11), 654–657. https://doi.org/10.1038/nphoton.2009.187

Kolbeck PJ, **Tišma M**, **Analikwu BT**, **Vanderlinden W**, **Dekker C and Lipfert J** (2024) Supercoiling-dependent DNA binding: Quantitative modeling and applications to bulk and single-molecule experiments. *Nucleic Acids Research* **52** (1), 59–72. https://doi.org/10.1093/nar/gkad1055

Krause S, **Neumann M**, **Fröbe M**, **Magerle R and Von Borczyskowski C** (2016) Monitoring Nanoscale deformations in a drawn polymer melt with single-molecule fluorescence polarization microscopy. *ACS Nano* **10** (2), 1908–1917. https://doi.org/10.1021/acsnano.5b05729

Krebs MRH, **Bromley EHC and Donald AM** (2005) The binding of thioflavin-T to amyloid fibrils: Localisation and implications. *Journal of Structural Biology* **149** (1), 30–37. https://doi.org/10.1016/j.jsb.2004.08.002

Kucherak OA, **Oncul S**, **Darwich Z**, **Yushchenko DA**, **Arntz Y**, **Didier P**, **Mély Y and Klymchenko AS** (2010) Switchable Nile red-based probe for cholesterol and lipid order at the outer leaflet of biomembranes. *Journal of the American Chemical Society* **132** (13), 4907–4916. https://doi.org/10.1021/ja100351w

Kuo C and Hochstrasser RM (2011) Super-resolution microscopy of lipid bilayer phases. *Journal of the American Chemical Society* **133** (13), 4664–4667. https://doi.org/10.1021/ja1099193

Larsson A, **Carlsson C**, **Jonsson M and Albinsson B** (1994) Characterization of the binding of the fluorescent dyes YO and YOYO to DNA by polarized light spectroscopy. *Journal of the American Chemical Society* **116** (19), 8459–8465. https://doi.org/10.1021/ja00098a004

Lee SF, **Vérolet Q and Fürstenberg A** (2013) Improved super-resolution microscopy with Oxazine Fluorophores in heavy water. *Angewandte Chemie International Edition* **52** (34), 8948–8951. https://doi.org/10.1002/anie.201302341

Lelek M, **Gyparaki MT**, **Beliu G**, **Schueder F**, **Griffié J**, **Manley S**, **Jungmann R**, **Sauer M**, **Lakadamyali M and Zimmer C** (2021) Single-molecule localization microscopy. *Nature Reviews Methods Primers* **1** (1), 39. https://doi.org/10.1038/s43586-021-00038-x

Lew MD, **Backlund MP and Moerner WE** (2013) Rotational mobility of single molecules affects localization accuracy in super-resolution fluorescence microscopy. *Nano Letters* **13** (9), 3967–3972. https://doi.org/10.1021/nl304359p

Lew MD and Moerner WE (2014) Azimuthal polarization filtering for accurate, precise, and robust single-molecule localization microscopy. *Nano Letters* **14** (11), 6407–6413. https://doi.org/10.1021/nl502914k

Li H and Vaughan JC (2018) Switchable Fluorophores for single-molecule localization microscopy. *Chemical Reviews* **118** (18), 9412–9454. https://doi.org/10.1021/acs.chemrev.7b00767

Lieb MA, **Zavislan JM and Novotny L** (2004) Single-molecule orientations determined by direct emission pattern imaging. *Journal of the Optical Society of America B* **21** (6), 1210. https://doi.org/10.1364/JOSAB.21.001210

Lim K, **Ropp C**, **Barik S**, **Fourkas J**, **Shapiro B and Waks E** (2016) Nanostructure-induced distortion in single-emitter microscopy. *Nano Letters* **16** (9), 5415–5419. https://doi.org/10.1021/acs.nanolett.6b01708

Lippert LG, **Dadosh T**, **Hadden JA**, **Karnawat V**, **Diroll BT**, **Murray CB**, **Holzbaur ELF**, **Schulten K**, **Reck-Peterson SL and Goldman YE** (2017) Angular measurements of the dynein ring reveal a stepping mechanism dependent on a flexible stalk. *Proceedings of the National Academy of Sciences* **114** (23), E4564–E4573. https://doi.org/10.1073/pnas.1620149114

Liu S, **Chen J**, **Hellgoth J**, **Müller L-R**, **Ferdman B**, **Karras C**, **Xiao D**, **Lidke KA**, **Heintzmann R**, **Shechtman Y**, **Li Y and Ries J** (2024) Universal inverse modeling of point spread functions for SMLM localization and microscope characterization. *Nature Methods* **21** (6), 1082–1093. https://doi.org/10.1038/s41592-024-02282-x

Lu J, **Mazidi H**, **Ding T**, **Zhang O and Lew MD** (2020) Single-molecule 3D orientation imaging reveals Nanoscale compositional heterogeneity in lipid membranes. *Angewandte Chemie International Edition* **59** (40), 17572–17579. https://doi.org/10.1002/anie.202006207

Lupo C and Pirandola S (2016) Ultimate precision bound of quantum and subwavelength imaging. *Physical Review Letters* **117** (19), 190802. https://doi.org/10.1103/PhysRevLett.117.190802

Maurer J, **Albrecht CS**, **Herbert P**, **Heussman D**, **Chang A**, **Von Hippel PH and Marcus AH** (2023) Studies of DNA 'breathing' by polarization-sweep single-molecule fluorescence microscopy of Exciton-coupled (iCy3) $_2$ dimer-labeled DNA fork constructs. *The Journal of Physical Chemistry B* **127** (50), 10730–10748. https://doi.org/10.1021/acs.jpcb.3c06463

Mazidi H, **King ES**, **Zhang O**, **Nehorai A and Lew MD** (2019) Dense super-resolution imaging of molecular orientation via joint sparse basis deconvolution and spatial pooling. In *2019 IEEE 16th International Symposium on Biomedical Imaging (ISBI 2019)*. IEEE, pp. 325–329. https://doi.org/10.1109/ISBI.2019.8759444.

Mehta SB, **McQuilken M**, **La Riviere PJ**, **Occhipinti P**, **Verma A**, **Oldenbourg R**, **Gladfelter AS and Tani T** (2016) Dissection of molecular assembly dynamics by tracking orientation and position of single molecules in live cells. *Proceedings of the National Academy of Sciences* **113** (42). https://doi.org/10.1073/pnas.1607674113

Melnikov SM, **Yeow EKL**, **Uji-i H**, **Cotlet M**, **Müllen K**, **De Schryver FC**, **Enderlein J and Hofkens J** (2007) Origin of simultaneous donor−acceptor emission in single molecules of Peryleneimide−Terrylenediimide labeled Polyphenylene Dendrimers. *The Journal of Physical Chemistry B* **111** (4), 708–719. https://doi.org/10.1021/jp0655625

Metskas LA and Rhoades E (2020) Single-molecule FRET of intrinsically disordered proteins. *Annual Review of Physical Chemistry* **71** (1), 391–414. https://doi.org/10.1146/annurev-physchem-012420-104917

Mildenhall B, **Srinivasan PP**, **Tancik M**, **Barron JT**, **Ramamoorthi R and Ng R** (2022) NeRF: Representing scenes as neural radiance fields for view synthesis. *Communications of the ACM* **65** (1), 99–106. https://doi.org/10.1145/3503250

Möckl L and Moerner WE (2020) Super-resolution microscopy with single molecules in biology and beyond–essentials, current trends, and future challenges. *Journal of the American Chemical Society* **142** (42), 17828–17844. https://doi.org/10.1021/jacs.0c08178

Möckl L, **Roy AR and Moerner WE** (2020) Deep learning in single-molecule microscopy: Fundamentals, caveats, and recent developments [invited]. *Biomedical Optics Express* **11** (3), 1633. https://doi.org/10.1364/BOE.386361

Moerner WE (2015) Single-molecule spectroscopy, imaging, and photocontrol: Foundations for super-resolution microscopy (nobel lecture). *Angewandte Chemie International Edition* **54** (28), 8067–8093. https://doi.org/10.1002/anie.201501949

Moerner WE and Kador L (1989) Optical detection and spectroscopy of single molecules in a solid. *Physical Review Letters* **62** (21), 2535–2538. https://doi.org/10.1103/PhysRevLett.62.2535

Moon G, **Son T**, **Yoo H**, **Lee C**, **Lee H**, **Im S and Kim D** (2023) Defocused imaging-based quantification of plasmon-induced distortion of single emitter emission. *Light: Science & Applications* **12** (1), 221. https://doi.org/10.1038/s41377-023-01237-9

Moon TK and Stirling WC (2000) *Mathematical Methods and Algorithms for Signal Processing*. New Jersey: Prentice Hall.

Mortensen KI, **Churchman LS**, **Spudich JA and Flyvbjerg H** (2010) Optimized localization analysis for single-molecule tracking and super-resolution microscopy. *Nature Methods* **7** (5), 377–381. https://doi.org/10.1038/nmeth.1447

Mortensen KI, **Sung J**, **Flyvbjerg H and Spudich JA** (2015) Optimized measurements of separations and angles between intra-molecular fluorescent markers. *Nature Communications* **6** (1), 8621. https://doi.org/10.1038/ncomms9621

Mortensen KI, **Sung J**, **Spudich JA and Flyvbjerg H** (2016) How to measure separations and angles between Intramolecular fluorescent markers. In *Methods in Enzymology*, Vol. **581**. Elsevier, pp. 147–185. https://doi.org/10.1016/bs.mie.2016.08.020.

https://doi.org/10.1017/S0033583524000167 Published online by Cambridge University Press

Munger E, Sison M and Brasselet S (2023) Influence of the excitation polarization on single molecule 3D orientation imaging. *Optics Communications* **541**, 129480. https://doi.org/10.1016/j.optcom.2023.129480

Nahidiazar L, Agronskaia AV, Broertjes J, van den Broek B and Jalink K (2016) Optimizing imaging conditions for demanding multi-color super resolution localization microscopy. *PLoS One* **11** (7), e0158884. https://doi.org/10.1371/journal.pone.0158884

Needham L-M, Weber J, Varela JA, Fyfe JWB, Do DT, Xu CK, Tutton L, Cliffe R, Keenlyside B, Klenerman D, Dobson CM, Hunter CA, Müller KH, O'Holleran K, Bohndiek SE, Snaddon TN and Lee SF (2020) ThX – A next-generation probe for the early detection of amyloid aggregates. *Chemical Science* **11** (18), 4578–4583. https://doi.org/10.1039/C9SC04730A

Nehme E, Freedman D, Gordon R, Ferdman B, Weiss LE, Alalouf O, Naor T, Orange R, Michaeli T and Shechtman Y (2020) DeepSTORM3D: Dense 3D localization microscopy and PSF design by deep learning. *Nature Methods* **17** (7), 734–740. https://doi.org/10.1038/s41592-020-0853-5

Nelson T, Vargas-Hernández S, Freire M, Cheng S and Gustavsson A-K (2024) Multimodal illumination platform for 3D single-molecule super-resolution imaging throughout mammalian cells. *Biomedical Optics Express* **15** (5), 3050. https://doi.org/10.1364/BOE.521362

Nettels D, Galvanetto N, Ivanović MT, Nüesch M, Yang T and Schuler B (2024) Single-molecule FRET for probing nanoscale biomolecular dynamics. *Nature Reviews Physics* **6** (10), 587–605. https://doi.org/10.1038/s42254-024-00748-7

Novotny L and Hecht B (2012) *Principles of Nano-Optics*. Cambridge, England: Cambridge University Press.

Ohmachi M, Komori Y, Iwane AH, Fujii F, Jin T and Yanagida T (2012) Fluorescence microscopy for simultaneous observation of 3D orientation and movement and its application to quantum rod-tagged myosin V. *Proceedings of the National Academy of Sciences* **109** (14), 5294–5298. https://doi.org/10.1073/pnas.1118472109

Ojeda-Castañeda J, Andrés P and Díaz A (1986) Annular apodizers for low sensitivity to defocus and to spherical aberration. *Optics Letters* **11** (8), 487. https://doi.org/10.1364/OL.11.000487

Oleksiievets N, Mathew C, Thiele JC, Gallea JI, Nevskyi O, Gregor I, Weber A, Tsukanov R and Enderlein J (2022) Single-molecule fluorescence lifetime imaging using wide-field and confocal-laser scanning microscopy: A comparative analysis. *Nano Letters* **22** (15), 6454–6461. https://doi.org/10.1021/acs.nanolett.2c01586

Outeiro TF, Putcha P, Tetzlaff JE, Spoelgen R, Koker M, Carvalho F, Hyman BT and McLean PJ (2008) Formation of toxic oligomeric α-synuclein species in living cells. *PLoS One* **3** (4), e1867. https://doi.org/10.1371/journal.pone.0001867

Ovesný M, Křížek P, Borkovec J, Švindrych Z and Hagen GM (2014) ThunderSTORM: A comprehensive ImageJ plug-in for PALM and STORM data analysis and super-resolution imaging. *Bioinformatics* **30** (16), 2389–2390. https://doi.org/10.1093/bioinformatics/btu202

Paeng K and Kaufman LJ (2016) Single molecule experiments reveal the dynamic heterogeneity and exchange time scales of polystyrene near the Glass transition. *Macromolecules* **49** (7), 2876–2885. https://doi.org/10.1021/acs.macromol.6b00097

Park JJ, Florence P, Straub J, Newcombe R and Lovegrove S (2019) DeepSDF: Learning continuous signed distance functions for shape representation. In *2019 IEEE/CVF Conference on Computer Vision and Pattern Recognition (CVPR)*. Long Beach, CA, USA: IEEE, pp. 165–174. https://doi.org/10.1109/CVPR.2019.00025.

Patra D, Gregor I and Enderlein J (2004) Image analysis of defocused single-molecule images for three-dimensional molecule orientation studies. *The Journal of Physical Chemistry A* **108** (33), 6836–6841. https://doi.org/10.1021/jp048188m

Pavani SRP and Piestun R (2008) High-efficiency rotating point spread functions. *Optics Express* **16** (5), 3484. https://doi.org/10.1364/OE.16.003484

Pavani SRP, Thompson MA, Biteen JS, SJ, Liu N, Twieg RJ, Piestun R and Moerner WE (2009) Three-dimensional, single-molecule fluorescence imaging beyond the diffraction limit by using a double-helix point spread function. *Proceedings of the National Academy of Sciences* **106** (9), 2995–2999. https://doi.org/10.1073/pnas.0900245106

Peterman EJG, Sosa H, Goldstein LSB and Moerner WE (2001) Polarized fluorescence microscopy of individual and many Kinesin motors bound to Axonemal microtubules. *Biophysical Journal* **81** (5), 2851–2863. https://doi.org/10.1016/S0006-3495(01)75926-7

Prasad S and Yu Z (2019) Quantum-limited superlocalization and superresolution of a source pair in three dimensions. *Physical Review A* **99** (2), 022116. https://doi.org/10.1103/PhysRevA.99.022116

Raab M, Vietz C, Stefani FD, Acuna GP and Tinnefeld P (2017) Shifting molecular localization by plasmonic coupling in a single-molecule mirage. *Nature Communications* **8** (1), 13966. https://doi.org/10.1038/ncomms13966

Radmacher N, Nevskyi O, Gallea JI, Thiele JC, Gregor I, Rizzoli SO and Enderlein J (2024) Doubling the resolution of fluorescence-lifetime single-molecule localization microscopy with image scanning microscopy. *Nature Photonics* **18** (10), 1059–1066. https://doi.org/10.1038/s41566-024-01481-4

Ramkhalawon RD, Brown TG and Alonso MA (2013) Imaging the polarization of a light field. *Optics Express* **21** (4), 4106. https://doi.org/10.1364/OE.21.004106

Rasnik I, McKinney SA and Ha T (2006) Nonblinking and long-lasting single-molecule fluorescence imaging. *Nature Methods* **3** (11), 891–893. https://doi.org/10.1038/nmeth934

Rehacek J, Paúr M, Stoklasa B, Hradil Z and Sánchez-Soto LL (2017) Optimal measurements for resolution beyond the Rayleigh limit. *Optics Letters* **42** (2), 231. https://doi.org/10.1364/OL.42.000231

Reinhardt SCM, Masullo LA, Baudrexel I, Steen PR, Kowalewski R, Eklund AS, Strauss S, Unterauer EM, Schlichthaerle T, Strauss MT, Klein C and Jungmann R (2023) Ångström-resolution fluorescence microscopy. *Nature* **617** (7962), 711–716. https://doi.org/10.1038/s41586-023-05925-9

Rimoli CV, Valades-Cruz CA, Curcio V, Mavrakis M and Brasselet S (2022) 4polar-STORM polarized super-resolution imaging of actin filament organization in cells. *Nature Communications* **13** (1), 301. https://doi.org/10.1038/s41467-022-27966-w

Rosenberg SA, Quinlan ME, Forkey JN and Goldman YE (2005) Rotational motions of macro- molecules by single-molecule fluorescence microscopy. *Accounts of Chemical Research* **38** (7), 583–593. https://doi.org/10.1021/ar040137k

Rust MJ, Bates M and Zhuang X (2006) Sub-diffraction-limit imaging by stochastic optical reconstruction microscopy (STORM). *Nature Methods* **3** (10), 793–796. https://doi.org/10.1038/nmeth929

Sahl SJ, Matthias J, Inamdar K, Weber M, Khan TA, Brüser C, Jakobs S, Becker S, Griesinger C, Broichhagen J and Hell SW (2024) Direct optical measurement of intramolecular distances with angstrom precision. *Science* **386** (6718), 180–187. https://doi.org/10.1126/science.adj7368

Sahoo H, Roccatano D, Hennig A and Nau WM (2007) A 10-Å spectroscopic ruler applied to short Polyprolines. *Journal of the American Chemical Society* **129** (31), 9762–9772. https://doi.org/10.1021/ja072178s

Sarkar A, Namboodiri V and Kumbhakar M (2023) Single-molecule orientation imaging reveals two distinct binding configurations on amyloid fibrils. *The Journal of Physical Chemistry Letters* **14** (21), 4990–4996. https://doi.org/10.1021/acs.jpclett.3c00823

Sauer M and Heilemann M (2017) Single-molecule localization microscopy in eukaryotes. *Chemical Reviews* **117** (11), 7478–7509. https://doi.org/10.1021/acs.chemrev.6b00667

Schoen I, Ries J, Klotzsch E, Ewers H and Vogel V (2011) Binding-activated localization microscopy of DNA structures. *Nano Letters* **11** (9), 4008–4011. https://doi.org/10.1021/nl2025954

Shaban HA, Valades-Cruz CA, Savatier J and Brasselet S (2017) Polarized super-resolution structural imaging inside amyloid fibrils using Thioflavine T. *Scientific Reports* **7** (1), 12482. https://doi.org/10.1038/s41598-017-12864-9

Shankar R (2012) *Principles of Quantum Mechanics*. Springer Science \& Business Media.

Sharonov A and Hochstrasser RM (2006) Wide-field subdiffraction imaging by accumulated binding of diffusing probes. *Proceedings of the National Academy of Sciences* **103** (50), 18911–18916. https://doi.org/10.1073/pnas.0609643104

Shechtman Y, Weiss LE, Backer AS, Sahl SJ and Moerner WE (2015) Precise three-dimensional scan-free multiple-particle tracking over large axial ranges with tetrapod point spread functions. *Nano Letters* **15** (6), 4194–4199. https://doi.org/10.1021/acs.nanolett.5b01396

Shtengel G, Galbraith JA, Galbraith CG, Lippincott-Schwartz J, Gillette JM, Manley S, Sougrat R, Waterman CM, Kanchanawong P, Davidson MW, Fetter RD and Hess HF (2009) Interferometric fluorescent super-resolution

https://doi.org/10.1017/S0033583524000167 Published online by Cambridge University Press

microscopy resolves 3D cellular ultrastructure. *Proceedings of the National Academy of Sciences* **106** (9), 3125–3130. https://doi.org/10.1073/pnas.0813131106

Sindbert S, Kalinin S, Nguyen H, Kienzler A, Clima L, Bannwarth W, Appel B, Müller S and Seidel CAM (2011) Accurate distance determination of nucleic acids via Förster resonance energy transfer: Implications of dye linker length and rigidity. *Journal of the American Chemical Society* **133** (8), 2463–2480. https://doi.org/10.1021/ja105725e

Sosa H, Peterman EJG, Moerner WE and Goldstein LSB (2001) ADP-induced rocking of the kinesin motor domain revealed by single-molecule fluorescence polarization microscopy. *Nature Structural Biology* **8** (6), 540–544. https://doi.org/10.1038/88611

Spehar K, Ding T, Sun Y, Kedia N, Lu J, Nahass GR, Lew MD and Bieschke J (2018) Super-resolution imaging of amyloid structures over extended times by using transient binding of single thioflavin T molecules. *Chembiochem* **19** (18), 1944–1948. https://doi.org/10.1002/cbic.201800352

Speiser A, Müller L-R, Hoess P, Matti U, Obara CJ, Legant WR, Kreshuk A, Macke JH, Ries J and Turaga SC (2021) Deep learning enables fast and dense single-molecule localization with high accuracy. *Nature Methods* **18** (9), 1082–1090. https://doi.org/10.1038/s41592-021-01236-x

Stallinga S (2015) Effect of rotational diffusion in an orientational potential well on the point spread function of electric dipole emitters. *Journal of the Optical Society of America A* **32** (2), 213. https://doi.org/10.1364/JOSAA.32.000213

Steen PR, Unterauer EM, Masullo LA, Kwon J, Perovic A, Jevdokimenko K, Opazo F, Fornasiero EF and Jungmann R (2024) The DNA-PAINT palette: A comprehensive performance analysis of fluorescent dyes. *Nature Methods* **21** (9), 1755–1762. https://doi.org/10.1038/s41592-024-02374-8

Steves MA, He C and Xu K (2024) Single-molecule spectroscopy and super-resolution mapping of physicochemical parameters in living cells. *Annual Review of Physical Chemistry* **75** (1), 163–183. https://doi.org/10.1146/annurev-physchem-070623-034225

Sun B, Ding T, Zhou W, Porter TS and Lew MD (2024) Single-molecule orientation imaging reveals the nano-architecture of amyloid fibrils undergoing growth and decay. *Nano Letters* **24** (24), 7276–7283. https://doi.org/10.1021/acs.nanolett.4c01263

Testa I, Schönle A, Middendorff V, Geisler C, Medda C, Wurm R, Stiel CA, Jakobs AC, Bossi S, Eggeling M, Hell SW C and Egner A (2008) Nanoscale separation of molecular species based on their rotational mobility. *Optics Express* **16** (25), 21093. https://doi.org/10.1364/OE.16.021093

Thiele JC, Helmerich DA, Oleksiievets N, Tsukanov R, Butkevich E, Sauer M, Nevskyi O and Enderlein J (2020) Confocal fluorescence-lifetime single-molecule localization microscopy. *ACS Nano* **14** (10), 14190–14200. https://doi.org/10.1021/acsnano.0c07322

Tholen MME, Tas RP, Wang Y and Albertazzi L (2023) Beyond DNA: New probes for PAINT super-resolution microscopy. *Chemical Communications* **59** (54), 8332–8342. https://doi.org/10.1039/D3CC00757J

Thorsen RØ, Hulleman CN, Rieger B and Stallinga S (2022) Photon efficient orientation estimation using polarization modulation in single-molecule localization microscopy. *Biomedical Optics Express* **13** (5), 2835. https://doi.org/10.1364/BOE.452159

Toprak E, Enderlein J, Syed S, McKinney SA, Petschek RG, Ha T, Goldman YE and Selvin PR (2006) Defocused orientation and position imaging (DOPI) of myosin V. *Proceedings of the National Academy of Sciences* **103** (17), 6495–6499. https://doi.org/10.1073/pnas.0507134103

Tosheva KL, Yuan Y, Matos Pereira P, Culley S and Henriques R (2020) Between life and death: Strategies to reduce phototoxicity in super-resolution microscopy. *Journal of Physics D: Applied Physics* **53** (16), 163001. https://doi.org/10.1088/1361-6463/ab6b95

Tsang M (2015) Quantum limits to optical point-source localization. *Optica* **2** (7), 646. https://doi.org/10.1364/OPTICA.2.000646

Tsang M (2019) Quantum limit to subdiffraction incoherent optical imaging. *Physical Review A* **99** (1), 012305. https://doi.org/10.1103/PhysRevA.99.012305

Tsang M, Nair R and Lu X-M (2016) Quantum theory of superresolution for two incoherent optical point sources. *Physical Review X* **6** (3), 031033. https://doi.org/10.1103/PhysRevX.6.031033

Uji-i H, Melnikov SM, Deres A, Bergamini G, De Schryver F, Herrmann A, Müllen K, Enderlein J and Hofkens J (2006) Visualizing spatial and temporal heterogeneity of single molecule rotational diffusion in a glassy polymer by defocused wide-field imaging. *Polymer* **47** (7), 2511–2518. https://doi.org/10.1016/j.polymer.2005.11.094

Valades Cruz CA, Shaban HA, Kress A, Bertaux N, Monneret S, Mavrakis M, Savatier J and Brasselet S (2016) Quantitative nanoscale imaging of orientational order in biological filaments by polarized superresolution microscopy. *Proceedings of the National Academy of Sciences* **113** (7), E820–E828. https://doi.org/10.1073/pnas.1516811113

Valeur B (2002) *Molecular Fluorescence: Principles and Applications*. Weinheim, Germany: Wiley-VCH.

Vella A and Alonso MA (2019) Optimal birefringence distributions for imaging polarimetry. *Optics Express* **27** (25), 36799. https://doi.org/10.1364/OE.27.036799

Vogelsang J, Kasper R, Steinhauer C, Person B, Heilemann M, Sauer M and Tinnefeld P (2008) A reducing and oxidizing system minimizes Photobleaching and blinking of fluorescent dyes. *Angewandte Chemie International Edition* **47** (29), 5465–5469. https://doi.org/10.1002/anie.200801518

Waibel DJE, Röell E, Rieck B, Giryes R and Marr C (2023) A diffusion model predicts 3D shapes from 2D microscopy images. In *2023 IEEE 20th International Symposium on Biomedical Imaging (ISBI)*. Cartagena, Colombia: IEEE, pp. 1–5. https://doi.org/10.1109/ISBI53787.2023.10230752.

Walker AS, Rablen PR and Schepartz A (2016) Rotamer-restricted fluorogenicity of the bis-arsenical ReAsH. *Journal of the American Chemical Society* **138** (22), 7143–7150. https://doi.org/10.1021/jacs.6b03422

Wang M, Marr JM, Davanco M, Gilman JW and Liddle JA (2019) Nanoscale deformation in polymers revealed by single-molecule super-resolution localization–orientation microscopy. *Materials Horizons* **6** (4), 817–825. https://doi.org/10.1039/C8MH01187G

Weber M, Von Der Emde H, Leutenegger M, Gunkel P, Sambandan S, Khan TA, Keller-Findeisen J, Cordes VC and Hell SW (2023) MINSTED nanoscopy enters the Ångström localization range. *Nature Biotechnology* **41** (4), 569–576. https://doi.org/10.1038/s41587-022-01519-4

Wientjes E, Renger J, Cogdell R and van Hulst NF (2016) Pushing the photon limit: Nanoantennas increase maximal photon stream and Total photon number. *The Journal of Physical Chemistry Letters* **7** (9), 1604–1609. https://doi.org/10.1021/acs.jpclett.6b00491

Wu T, King MR, Qiu Y, Farag M, Pappu RV, Lew MD (2023) Single fluorogen imaging reveals distinct environmental and structural features of biomolecular condensates. *bioRxiv* 2023.01.26.525727. https://doi.org/10.1101/2023.01.26.525727

Wu T, Lu J and Lew MD (2022a) Dipole-spread-function engineering for simultaneously measuring the 3D orientations and 3D positions of fluorescent molecules. *Optica* **9** (5), 505. https://doi.org/10.1364/OPTICA.451899

Wu T, Lu P, Rahman MA, Li X and Lew MD (2022b) Deep-SMOLM: Deep learning resolves the 3D orientations and 2D positions of overlapping single molecules with optimal nanoscale resolution. *Optics Express* **30** (20), 36761. https://doi.org/10.1364/OE.470146

Xiao D, Kedem Orange R, Opatovski N, Parizat A, Nehme E, Alalouf O and Shechtman Y (2024) Large-FOV 3D localization microscopy by spatially variant point spread function generation. *Science Advances* **10** (10), eadj3656. https://doi.org/10.1126/sciadv.adj3656

Xie XS (1996) Single-molecule spectroscopy and dynamics at room temperature. *Accounts of Chemical Research* **29** (12), 598–606. https://doi.org/10.1021/ar950246m

Xu F, Ma D, MacPherson KP, Liu S, Bu Y, Wang Y, Tang Y, Bi C, Kwok T, Chubykin AA, Yin P, Calve S, Landreth GE and Huang F (2020) Three-dimensional nanoscopy of whole cells and tissues with in situ point spread function retrieval. *Nature Methods* **17** (5), 531–540. https://doi.org/10.1038/s41592-020-0816-x

Yildiz A, Forkey JN, McKinney SA, Ha T, Goldman YE and Selvin PR (2003) Myosin V walks hand-over-hand: Single Fluorophore imaging with 1.5-nm localization. *Science* **300** (5628), 2061–2065. https://doi.org/10.1126/science.1084398

Zhan P, Peil A, Jiang Q, Wang D, Mousavi S, Xiong Q, Shen Q, Shang Y, Ding B, Lin C, Ke Y and Liu N (2023) Recent advances in DNA origami-engineered nanomaterials and applications. *Chemical Reviews* **123** (7), 3976–4050. https://doi.org/10.1021/acs.chemrev.3c00028

Zhan Z, Li C, Liu X, Sun X, He C, Kuang C and Liu X (2022) Simultaneous super-resolution estimation of single-molecule position and orientation with

https://doi.org/10.1017/S0033583524000167 Published online by Cambridge University Press

minimal photon fluxes. *Optics Express* **30** (12), 22051. https://doi.org/10.1364/OE.456557

Zhang O, **Guo Z**, **He Y**, **Wu T**, **Vahey MD and Lew MD** (2023) Six-dimensional single-molecule imaging with isotropic resolution using a multi-view reflector microscope. *Nature Photonics* **17** (2), 179–186. https://doi.org/10.1038/s41566-022-01116-6

Zhang O and Lew MD (2019) Fundamental limits on measuring the rotational constraint of single molecules using fluorescence microscopy. *Physical Review Letters* **122** (19), 198301. https://doi.org/10.1103/PhysRevLett.122.198301

Zhang O and Lew MD (2020) Quantum limits for precisely estimating the orientation and wobble of dipole emitters. *Physical Review Research* **2** (3), 033114. https://doi.org/10.1103/PhysRevResearch.2.033114

Zhang O and Lew MD (2021a) Single-molecule orientation localization microscopy I: Fundamental limits. *Journal of the Optical Society of America A* **38** (2), 277. https://doi.org/10.1364/JOSAA.411981

Zhang O and Lew MD (2021b) Single-molecule orientation localization microscopy II: A performance comparison. *Journal of the Optical Society of America A* **38** (2), 288. https://doi.org/10.1364/JOSAA.411983

Zhang O, **Lu J**, **Ding T and Lew MD** (2018) Imaging the three-dimensional orientation and rotational mobility of fluorescent emitters using the tri-spot point spread function. *Applied Physics Letters* **113** (3), 031103. https://doi.org/10.1063/1.5031759

Zhang O, **Zhou H**, **Feng BY**, **Larsson EM**, **Alcalde RE**, **Yin S**, **Deng C and Yang C** (2024) Single-shot volumetric fluorescence imaging with neural fields. (Version 2). arXiv. https://doi.org/10.48550/ARXIV.2405.10463.

Zhang O, **Zhou W**, **Lu J**, **Wu T and Lew MD** (2022) Resolving the three-dimensional rotational and translational dynamics of single molecules using radially and azimuthally polarized fluorescence. *Nano Letters* **22** (3), 1024–1031. https://doi.org/10.1021/acs.nanolett.1c03948

Zhang Z, **Kenny SJ**, **Hauser M**, **Li W and Xu K** (2015) Ultrahigh-throughput single-molecule spectroscopy and spectrally resolved super-resolution microscopy. *Nature Methods* **12** (10), 935–938. https://doi.org/10.1038/nmeth.3528

Zhanghao K, **Chen L**, **Yang X-S**, **Wang M-Y**, **Jing Z-L**, **Han H-B**, **Zhang MQ**, **Jin D**, **J-T G and Xi P** (2016) Super-resolution dipole orientation mapping via polarization demodulation. *Light: Science & Applications* **5** (10), e16166–e16166. https://doi.org/10.1038/lsa.2016.166

Zheng Z, **Kuang F and Zhao J** (2010) Direct observation of rotational motion of Fluorophores chemically attached to polystyrene in its thin films. *Macromolecules* **43** (7), 3165–3168. https://doi.org/10.1021/ma902569n

Zhou H, **Feng BY**, **Guo H**, **Lin S (S)**, **Liang M**, **Metzler CA and Yang C** (2023) Fourier ptychographic microscopy image stack reconstruction using implicit neural representations. *Optica* **10**(12), 1679. https://doi.org/10.1364/OPTICA.505283.

Zhou W, **O'Neill CL**, **Ding T**, **Zhang O**, **Rudra JS and Lew MD** (2024a) Resolving the nanoscale structure of β-sheet peptide self-assemblies using single-molecule orientation–localization microscopy. *ACS Nano* **18** (12), 8798–8810. https://doi.org/10.1021/acsnano.3c11771

Zhou W, **Wu T and Lew MD** (2024b) Fundamental limits in measuring the anisotropic rotational diffusion of single molecules. *The Journal of Physical Chemistry A* acs.jpca.4c03160. https://doi.org/10.1021/acs.jpca.4c03160.

Zhu F-Y, **Mei L-J**, **Tian R**, **Li C**, **Wang Y-L**, **Xiang S-L**, **M-Q Z and Tang BZ** (2024) Recent advances in super-resolution optical imaging based on aggregation-induced emission. *Chemical Society Reviews* **53** (7), 3350–3383. https://doi.org/10.1039/D3CS00698K

Zondervan R, **Kulzer F**, **Berkhout GCG and Orrit M** (2007) Local viscosity of supercooled glycerol near T_g probed by rotational diffusion of ensembles and single dye molecules. *Proceedings of the National Academy of Sciences* **104** (31), 12628–12633. https://doi.org/10.1073/pnas.0610521104

Zuo T, **Goldwyn HJ**, **Isaacoff BP**, **Masiello DJ and Biteen JS** (2019) Rotation of single-molecule emission polarization by plasmonic nanorods. *The Journal of Physical Chemistry Letters* **10** (17), 5047–5054. https://doi.org/10.1021/acs.jpclett.9b02270

Zuo T, **Goldwyn HJ**, **Masiello DJ and Biteen JS** (2021) Model-based insight into single-molecule plasmonic mislocalization. *The Journal of Physical Chemistry C* **125** (44), 24531–24539. https://doi.org/10.1021/acs.jpcc.1c07989

https://doi.org/10.1017/S0033583524000167 Published online by Cambridge University Press